The Dissertation Committee for Yi Xu
certifies that this is the approved version of the following dissertation:

Brownian Motion of Optically Trapped Microspheres and Suspended Diaphragms

Committee:

Mark G. Raizen, Supervisor

John W. Keto

Can Kilic

Constantine Caramanis

Brownian Motion of Optically Trapped Microspheres and Suspended Diaphragms

by

Yi Xu

DISSERTATION

Presented to the Faculty of the Graduate School of

The University of Texas at Austin

in Partial Fulfillment

of the Requirements

for the Degree of

DOCTOR OF PHILOSOPHY

THE UNIVERSITY OF TEXAS AT AUSTIN

May 2023

To my parents and grandparents

Acknowledgments

First and foremost, I would like to thank my adviser Mark Raizen. Mark is a brilliant physicist and he always has an exceptional intuition regarding physics concepts and experiments. Mark is also very open for discussions about the direction of the experiment. Moreover, Mark is not only concerned about the academic life of his students but also their personal life. He is always very supportive of his students' decisions inside or outside the academic field. It has been a privilege to work in Mark's group.

When I first joined the group, I worked with Erik Anciaux on a project to demonstrate the one-dimensional Stern-Gerlach effect with a supersonic Neon beam. Erik and the Jamie Gardner had set up the structure of experiment for focusing the Neon beam. Erik shared with me his experience as a senior graduate student and I still remember the "π-rule" he told me in order to estimate the time it actually takes to complete a project for research. After one semester of working together, Erik wanted to focus on the focusing experiment to graduate, so I transferred to a different project developing a novel way of slowing and cooling atoms which was more inline with my original research interests.

Given that the new project used a magnetic decelerator to slow down lithium atoms, we often caller ourselves the slower team. Due to the complexity of the project, the slower team was quite large. There were two postdocs,

Lichung Ha and Pavel Nagornykh, and five graduate students, Kevin Melin, Yu Lu, Lukas Gradl, Logan Hillberry and me all working on the project together. It was everyone's effort that make it possible to develop and run such complicated experiment.

Pavel is a very knowledgeable and smart physicist. He has great insights into many different fields in physics. We worked together on many small projects and I'm very impressed by his ability to quickly set up a model to explain whatever experimental data that would arise. Kevin Melin was the most senior and experienced graduate student in the team. Kevin is a very helpful and is always willing to help everyone in the group no matter whether they are on the same project or not. He is very good at CAD, Labview, electronics and so on and he is always willing to pass the knowledge to junior graduate students. Whenever looking for specific piece of equipment in the lab, he could always point out the location. Yu's exceptional ability to learn quickly and take action has been a source of inspiration to me. He has generously shared his valuable experiences with me, including insights into career choices and picking up new skills, which have been incredibly useful. Lukas was the first person I met in the lab. I have always been consistently impressed by his unwavering persistence in understanding the fundamental theories covered in the core physics courses we took together. Logan entered the group around the same time as I did. He is very good at programming and shared lots of his programming knowledge to the group. We have been partners on experiments through the most my graduate school studies. At the end of the funding cycle

of the magnetic slower project, we were able to capture the lithium atoms from the magnetic slower into a magneto-optical trap after the postdocs and senior graduates students left. It remains one of the most memorable achievements in my graduate studies.

After three years working on cold atom experiments, I transferred to the project studying the short-time Brownian motion with optically trapped microspheres. Our group has pioneered measuring the short-time Brownian motion with a setup similar to our current one around ten years ago. When I joined the project, the postdoc Diney Either was just starting to rebuild the setup for trapping microspheres in air again. Diney is a very experienced physicist. In order to enrich our understanding of the field, he initiated a weekly journal club in which each of us would introduce a relevant paper to the rest of the group. Moreover, Diney also told me the importance of having a healthy lifestyle and work-life balance, which has been a valuable reminder to me during my time in the lab. While we were in the process of rebuilding our optical tweezer setup, Jianyong Mo, a former graduate student and postdoc in our group, provided us with many pieces of advice and guidance. Additionally, Jianyong offered me valuable suggestions on how to assess the feasibility of the project. I am very grateful for his guidance and support. Sebastian Miki-Silva worked on the optical tweezer project as an undergraduate student. Sebastian dedicated much time in the project and was always willing to learn and tackle problems. He is now pursuing a PhD degree in physics in another institution and I'm confident that he will be very successful in graduate school.

Shortly after gathering the experimental data for our weighing methodology paper, the COVID-19 outbreak occurred and our lab was temporarily shut down for several months. The experiment to use the optically trapped microsphere as a fast acoustic detector had to be paused and all of us started to work from home. During the time of lock-down, we started to simulate the fast acoustic signal measured in the proton therapy, which is one of the potential applications of our experiment. Tom Mazur, who is a former graduate of our group and now a Assistant Professor of Radiation Oncology, provided us with much useful guidance and advice. Simultaneously, we were also exploring the possibility of using a suspended thin diaphragm to create a portable, fast acoustic detector, and I began working many of the theoretical aspects of the project that would grow into the work of this dissertation. After we were able to return to work in the lab in a cohort schedule, I started to also work on the experimental aspects of the project as well.

Zhida Liu, a graduate student in Prof. Elaine Li's group, was one of my collaborators on the project to measure the Brownian motion of the suspended thin diaphragm. With his solid background in two-dimensional materials, he provided invaluable assistance in finding the appropriate samples for our measurements. Yuqi Meng, a graduate student in Prof. Neal Hall's group, also collaborated with me on this project. I am grateful for his support and assistance in running the LDV machine, which was crucial for the measurements.

Our group always has a very supportive and collaborative atmosphere across the whole lab. So I want to thank the other Raizen lab members who

worked on different projects. Georgios Stratis is very kind and welcoming. He always brewed and treated us with tasty coffee. Igal Bucay was working on the ionization project, and we would occasionally chat about various topics related to graduate school, future plans, and other random subjects. Ahmed Helal was the postdoc worked on the same project as Igal and he helped us measuring the radius of the silica microsphere using SEM. Aaron Barr joined the group as the new graduate student last summer. He started to work on the project to prevent iron deficiency and picked it up in a very short time. Additionally, Aaron also took over the safety officer work from me and has been doing a fantastic job. Shortly after Aaron joined the group, V.J. Ajith also joined us as a postdoc and started to work with Aaron on the same project. With his solid background in building AFMs, Ajith brought invaluable expertise to the team. He has been extremely helpful and supportive, always offering to lend a hand whenever needed.

I would also like to express my gratitude to all the UT staff who have helped me during my time in graduate school. I would like to thank the Physics machine shop for their exceptional work in turning our designs into functional devices. It has been a privilege for me to work with such a talented team of machinists, including Allan Schroeder, Kenny Schneider, Richard Goodwin, Jeff Boney, Bryan McDonald, and many others. I would also like to give special recognition to Jack Clifford, the supervisor of the student machine shop. Jack taught me the usage of many machine tools and provided much guidance when I tried to machine device on my own. I would also like to express my

gratitude to Olga Vera at the Center for Nonlinear Dynamics for her assistance in navigating the paperwork and administrative tasks during the early years of my graduate school career. I would like to thank Matt Ervin, the Graduate Coordinator of the physics department, for his willingness to answer my many questions regarding qualification, defense, and other aspects of graduate school. Additionally, I would like to thank Belle Howell who serves at the Center for Complex Quantum Systems for her help of organizing my defense and setting up DocuSign for the relevant paperwork.

I would like to take this opportunity to thank all of my friends, including Jihang Zhu, Mengke Liu, Bowen Ma, Wente Li, Zhanzhi Jiang, Xiantao Chen, Yue Wu, Lu Zheng, Shida Shen, Luyan Yu, Zexun Lin, and others, for making my life in Austin truly colorful and unforgettable. I would like to extend a special thanks to Jihang, who was my roommate during the pandemic. She gave me lots of help to get through that difficult time. I would also like to thank Alicia, who has always shown concern for my health and well-being during and after the pandemic.

I also extend my sincere gratitude to my PhD committee members, Prof. Mark Raizen, Prof. John Keto, Prof. Can Kilic, and Prof. Constantine Caramanis for graciously agreeing to serve on my committee, dedicating time to read and provide insightful feedback on my dissertation, and attending my final oral defense.

Finally I would like to thank my parents and grandparents for their love throughout these years. Without their unwavering support, I would not

have been able to make it to this point in my academic journey.

Brownian Motion of Optically Trapped Microspheres and Suspended Diaphragms

Publication No. _____

Yi Xu, Ph.D.
The University of Texas at Austin, 2023

Supervisor: Mark G. Raizen

This dissertation details our experiments of measuring the mass of optically trapped microspheres and suspended diaphragms using their Brownian motion.

The optically trapped microsphere is immersed in air and two different mass measurement methods are investigated based on fluctuations about thermal equilibrium. The first method is based on spectral analysis, which allows us to determine the relevant experimental parameters and also serves as a calibration step for the second method. The second method is based on the equipartition theorem and allows for rapid mass measurement.

A new method for measuring the effective mass of suspended diaphragms is presented by combining laser Doppler vibrometry and Brownian motion power spectral density analysis. By analyzing the relation between the fundamental resonant frequencies, the mode shape and the total mass of the

diaphragm can be determined without the need for prior knowledge of its mechanical properties. This technique provides a precise and efficient method for evaluating the mass of suspended diaphragms for real-life applications in a time-dependent way.

Table of Contents

List of Tables

List of Figures

Chapter 1

Introduction

Brownian motion refers to the random motion of microscopic objects suspended in a fluid. It was named after Robert Brown who first reported the observation of the irregular and persistent motion of pollen grains immersed in water through a microscope [1]. In 1905, Einstein gave a theoretical explanation that the Brownian motion is caused by the thermal motion of the molecules in the fluid and predicted that the average displacement of the particle $\bar{x}$ is proportional to the square root of time t as [2]

$$\bar{x} \equiv \sqrt{\left\langle [x(t) - x(0)]^2 \right\rangle} = \sqrt{2Dt}\,. \tag{1.1}$$

Here $D = k_{\mathrm{B}}T/\gamma$ is the diffusion constant, where k_{B} is the Boltzmann constant, T is the temperature and $\gamma = 6\pi\eta R$ is the Stokes friction coefficient for a sphere with radius R. Marian von Smoluchowski independently derived Eq. (1.1) from a different perspective in 1906 [3]. In 1908, Paul Langevin applied Newton's second law to solve the Brownian motion of the particle [4] and derived what is now known as the Langevin equation. Shortly after in 1909, Jean Perrin conducted experiments verifying Einstein's theory of Brownian motion [5], which provided experimental evidence for the existence of atoms and molecules and allowed for the measurement of Avogadro's number.

At long time scales, the particle's Brownian motion can be explained very well by Eq. (1.1). This regime is called the diffusive regime where the trajectories of the Brownian particles are continuous everywhere but not differentiable anywhere [6]. Since velocity is defined as the time derivative of the displacement, Brownian particles therefore do not have well-defined velocities in the diffusive regime. However, the average velocity over time t can still be expressed as $\bar{v} = x/t = \sqrt{2D/t}$ according to Eq. (1.1), which diverges to infinity as t goes to zero.

In 1907, Einstein developed the theory to address this divergence problem by considering the instantaneous velocity of Brownian particles at short time scales where the motion of the Brownian particle is ballistic and dominated by its inertia [7]. However, Einstein predicted that it would be impossible to measure the instantaneous velocity of a Brownian particle due to the rapid exchange of thermal energy between the particle and the fluid resulting in small displacements of the particle over short time scales. After more than a century since Einstein's prediction of the instantaneous velocity, our group successfully measured the instantaneous velocity of optically trapped Brownian microspheres both in air [8] and liquid [9] after achieving sub-nanometer spatial resolutions and microsecond temporal resolutions.

The previous research from our group provides the necessary foundation for us to develop two approaches for accurately weighing a microsphere that is optically trapped and at thermal equilibrium in air. The first method is based on spectral analysis, which allows us to simultaneously determine the

relevant experimental parameters and also serves as a calibration step for the second method. The second method relies on the equipartition theorem and enables rapid mass measurement of the microsphere. Both of these methods are described in detail in Chapter 4.

After calibrating our system using the method described in Chapter 4, we can use the optically trapped microsphere as a high-bandwidth acoustic detector, as detailed in Reference [10]. This is a step towards developing a quantum-limited acoustic detector, which has potential applications in detecting the Bragg peak in proton therapy for cancer treatment [11–13] and in detecting acoustic waves in bubble chambers used for dark matter searches [14–16]. Currently our optical tweezer setup is large and not portable; therefore, we are also researching applications of suspended two-dimensional (2D) diaphragm technology to create a more portable acoustic detector.

The study of suspended 2D diaphragm dynamics has been a growing area of research in the past decade. The micro-sized suspended thin diaphragms have been shown to have fundamental resonant frequencies in the MHz regime [17], leading to a low thermal noise floor and a wide detection bandwidth. Additionally, suspended 2D diaphragms feature a high aspect ratio and an extremely small mass due to their ultra-thin profile, yielding a high sensitivity transducer. In many cases, the Brownian motion of the suspended diaphragm is used as a tool to calibrate the system, known as thermomechanical calibration [18, 19]. This calibration method requires knowledge of the effective mass of the diaphragm, which depends on the total mass and the

resonant mode shape of the diaphragm [18].

The most intuitive way to measure the total mass of the suspended diaphragm is to use its dimensions in the 2D plane, thickness and density to directly calculate the total mass. Scanning electron microscopy (SEM) can accurately measure the planar dimensions of the diaphragm, whereas the thickness can be determined via an atomic force microscope (AFM), Raman spectrum, etc [19]. However, the suspended 2D material's ultra-thinness makes it very sensitive to contamination, which can affect the thickness, density and other mechanical properties of the diaphragm [20, 21].

The resonant mode shapes of the suspended diaphragm are also very important properties for analysis. Not only do they determine the ratio between the effective mass and the total mass of the diaphragm [18], they are also related to the calibration of the measurement. For example, when using a focused laser beam to detect the out-of-plane motion of the suspended diaphragm, the readout signal is a weighted average of the deflection over the size of the focal spot of the laser beam. When the out-of-plane motion of the suspended diaphragm is primarily determined by either the surface tension or the bending rigidity of the diaphragm alone, there are analytical solutions of the resonant mode shapes [18, 22]. However, no analytic expressions of the mode shapes can be found in the intermediate region where both the surface tension and the bending rigidity need to be included [23]. In Chapter 5, we (independently) develop a method that uses the measured first fundamental frequency to numerically solve the mode shapes of a suspended circular di-

aphragm with known dimensions, thickness and mechanical properties related to the bending rigidity but an unknown surface tension. Other numerical solutions from different approaches are presented in References [24, 25]. The downside of these methods is that they require physical and mechanical properties of the diaphragm that are susceptible to change due to contamination of the diaphragm [20].

In this dissertation we demonstrate a weighing method to first measure the effective mass of a suspended diaphragm with laser Doppler vibrometry that directly reads out the displacement signal. Using a spectral method similar to that used to weigh the optically trapped microsphere, the effective mass can be extracted. We then demonstrate a method that uses the first two resonant frequencies to numerically determine the resonant mode shape as well as the effective mass of the diaphragm. This method does not require the knowledge of physical and mechanical properties that are affected by contamination. Thus, it provides a possible means of studying suspended diaphragms in the ambient environments. This weighing experiment is covered in Chapter 6.

This dissertation is organized as follows: In Chapter 2, the fundamental theories of Brownian motion of optically trapped microspheres are reviewed, which include the theories of Brownian motion and the principles of optical tweezers. In Chapter 3, we cover the experimental setup used to trap and detect the short-time Brownian motion of silica microspheres. This includes the optical setup, the procedure to align the dual-beam optical tweezer, the apparatus to launch silica microspheres and the detection system. Chapter 4

details published experimental results of weighing an optically trapped silica microsphere in thermal equilibrium with air via two different methods, which are based on spectral analysis and the equipartition theorem, respectively. In Chapter 5, we shift focus from single microspheres to suspended diaphragms and present a theory for the Brownian motion of these structures. A theoretical derivation of the transverse motion of the diaphragm that takes into account both its bending rigidity and surface tension, under the assumption that the diaphragm is free of contamination, is presented. In Chapter 6, we describe an experiment to measure the Brownian motion of graphene diaphragms. This includes the setup of the experiment and the method we use to extract the mass of the diaphragm from multiple resonant frequencies resulting from its Brownian motion. In Chapter 7, we discuss our efforts to develop a high-bandwidth, quantum-limited acoustic detector. This includes the development of a high-power balanced photodetector for use in optical trapping experiments and the study of the Brownian motion of graphene diaphragms in ambient air. We also propose a design for a portable acoustic detector based on a heterodyne fiber interferometer with a graphene membrane.

Chapter 2

Theoretical Background

In this chapter we will provide an overview of the fundamental theories related to the experimental work covered in later chapters. First, the theories of the Brownian motion of a single spherical particle will be discussed. In Section 2.1.1 we introduce the Langevin equation that describes the Brownian motion of a single free particle in a viscous fluid [4, 26, 27]. Following the method developed by George E. Uhlenbeck and Leonard S. Ornstein in Reference [27], the fluctuation-dissipation theorem is derived from the Langevin equation. We introduce a general method to study Brownian motion in Section 2.1.2, which is based on the Kubo-Green formula [28–30] and the Wiener-Khinchin theorem [31]. This method is then applied to specific examples in Section 2.1.3, including a free particle and a trapped particle, to demonstrate its use in solving specific Brownian motion problems and to also derive the statistical tools to analyze Brownian motion.

Following the discussion of the theories of Brownian motion, we will dive into the principle of optical tweezers. Optical tweezers utilize the radiation pressure of focused light to manipulate microscopic objects, allowing us to trap microscopic particles in a fluid and study their Brownian motion. The principle of optical tweezers will be introduced with a combination of an

intuitive image, theoretical analysis and numerical results in different regimes which are determined by the size of the particle and the wavelength of the laser.

2.1 Theories of Brownian motion

In this section, we will introduce the theories and analytic techniques to study the Brownian motion of a particle in a viscous fluid (with low Reynolds number) at thermal equilibrium. For simplicity and consistency with our experimental system, we only focus on the Brownian motion of a particle in one-dimension here but the results can be easily extended to higher dimensions.

2.1.1 Langevin equation

The dynamics of a free Brownian particle with mass m in a viscous fluid can be described by the Langevin equation [4, 26, 27]

$$m\ddot{x}(t) + \gamma\dot{x}(t) = F_{th}(t)\,, \tag{2.1}$$

where $x(t)$ is the position of the particle at time t. The drag force is $F_{drag} = -\gamma\dot{x}(t)$ where γ is the Stokes friction coefficient. If the particle is a sphere with radius R and the fluid has a viscosity η, then the Stokes friction coefficient can be expressed as $\gamma = 6\pi\eta R$. The thermal force is expressed as $F_{th}(t) = \epsilon\zeta(t)$ where $\zeta(t)$ represents a normalized Gaussian white noise (GWN) with a zero-mean $\langle\zeta(t)\rangle = 0$ and a δ-correlated property $\langle\zeta(t)\zeta(t')\rangle = \delta(t-t')$. The

brackets $\langle\cdot\rangle$ denote ensemble averages over the realizations of ζ. Since the auto-correlation function of a random process $\xi(t)$ is defined as

$$C_{\xi\xi}(t,t') \equiv \left\langle \xi(t)\xi(t') \right\rangle , \tag{2.2}$$

the δ-correlation property of GWN can be re-written as $C_{\zeta\zeta}(t,t') = \delta(t-t')$ or $C_{\zeta\zeta}(\tau) = \delta(\tau)$ where $\tau = t - t'$.

The statistics of the Brownian motion of a particle depend on a very important concept called the mean-squared displacement (MSD), which measures how much the position of the particle deviates from the starting point after time t. The MSD is defined as

$$\mathrm{MSD}(t) \equiv \left\langle [x(t) - x(0)]^2 \right\rangle . \tag{2.3}$$

Based on the definition of the auto-correlation function above, the relation between the MSD and the auto-correlation function of a stationary process is

$$\mathrm{MSD}(t) = 2\left(C_{xx}(0) - C_{xx}(t)\right) . \tag{2.4}$$

If the initial condition of the particle is $x(0) = x_0$ and $v(0) = v_0$ at time $t = 0$, where x_0 and v_0 represent the initial position and velocity of the Brownian particle, respectively, we can obtain the velocity of the Brownian particle at time t by integrating Eq. (2.1) over time:

$$v(t) = v_0 e^{-\frac{\gamma}{m}t} + \frac{\epsilon}{m} e^{-\frac{\gamma}{m}t} \int_0^t \zeta(t') e^{\frac{\gamma}{m}t'} dt' . \tag{2.5}$$

Averaging over the ensemble of particles and using properties of $\zeta(t)$ mentioned above, we can write the mean of the velocity as simple expression

$$\left\langle v(t) \right\rangle = v_0 e^{-\frac{\gamma}{m}t} . \tag{2.6}$$

So, the averaged variance of the velocity of at time t is then [27]

$$\sigma_v^2(t) = \left\langle \left(v(t) - \left\langle v(t) \right\rangle\right)^2 \right\rangle = \frac{\epsilon^2}{2m\gamma}\left(1 - e^{-\frac{2\gamma}{m}t}\right) . \tag{2.7}$$

We can easily see that when $t \to \infty$, $\left\langle v(t) \right\rangle \to 0$ and $\sigma_v^2(t) \to \epsilon^2/2m\gamma$. Based on equipartition theorem, we have

$$\frac{\epsilon^2}{2m\gamma} = \frac{k_B T}{m} . \tag{2.8}$$

Upon rearranging we can get

$$\epsilon = \sqrt{2k_B T\gamma} . \tag{2.9}$$

This equation above links that magnitude of the thermal force to the dissipation, which is known as the fluctuation-dissipation theorem.

2.1.2 A general approach to study Brownian motion

In this subsection, we will introduce a general and organized approach to study Brownian motion. This approach will provide a standard procedure useful for the analysis of the Brownian motion of particles.

2.1.2.1 Kubo-Green formula

Before introducing the Kubo-Green formula, let's first consider a linear time-invariant (LTI) system taking an input $X_i(t)$ and giving an output $Y_i(t)$. The linearity of the system implies that an input signal $a_1X_1(t) + a_2X_2(t)$ will yield an output signal $a_1Y_1(t) + a_2Y_2(t)$ when a_1 and a_2 are constants. The time-invariance of the system means that $Y(t + \tau)$ is the output when the

input signal is $X(t+\tau)$ for any τ, which implies that the output of the system for a given input signal doesn't depend on the time.

The output signal $Y(t)$ of the LTI system can be written as the convolution of the input signal $X(t)$ and an impulse response $h(t)$,

$$Y(t) = \int_{-\infty}^{\infty} h(t-\tau)X(\tau)d\tau\,. \tag{2.10}$$

We can see from the equation above that when the input signal is a delta function $\delta(t)$, the output signal will be equal to $h(t)$, which means $h(t)$ captures the system's reponse to a impulse signal. Using the convolution theorem that states convolution in the time domain becomes multiplication in the frequency domain, we can express the output signal in the frequency domain as

$$\tilde{Y}(\omega) = \tilde{h}(\omega)\tilde{X}(\omega)\,, \tag{2.11}$$

where $\tilde{X}(\omega)$, $\tilde{Y}(\omega)$ and $\tilde{h}(\omega)$ are the Fourier transforms of the input signal, output signal and impulse response, respectively. Since the cross auto-correlation between $X(t)$ and $Y(t)$ is

$$\begin{aligned} C_{XY}(t,t') = \big\langle X(t)Y(t')\big\rangle &= \int_{-\infty}^{\infty} h(t'-\tau)\big\langle X(t)X(\tau)\big\rangle d\tau \\ &= \int_{-\infty}^{\infty} h(t'-\tau)C_{XX}(t,\tau)d\tau = \int_{-\infty}^{\infty} h(\alpha)C_{XX}(t,t'-\alpha)d\alpha\,, \end{aligned} \tag{2.12}$$

we can obtain the auto-correlation of $Y(t)$ as

$$\begin{aligned} C_{YY}(t,t') = \big\langle Y(t)Y(t')\big\rangle &= \int_{-\infty}^{\infty} h(t-\tau)\big\langle X(\tau)Y(t')\big\rangle d\tau \\ &= \int_{-\infty}^{\infty} h(t-\tau)C_{XY}(\tau,t')d\tau = \int_{-\infty}^{\infty} h(\beta)C_{XY}(t-\beta,t')d\beta\,. \end{aligned} \tag{2.13}$$

When $X(t)$ is a stationary process and we let $\tau = t' - t$, we have

$$C_{XY}(\tau) = \int_{-\infty}^{\infty} h(\alpha) C_{XX}(\tau - \alpha) d\alpha = (h * C_{XX})(\tau)\,, \tag{2.14}$$

$$\begin{aligned} C_{YY}(\tau) &= \int_{-\infty}^{\infty} h(\beta) C_{XY}(\tau + \beta) d\beta \\ &= \int_{-\infty}^{\infty} h(-\alpha) C_{XY}(\tau - \alpha) d\alpha = h(-\tau) * C_{XX}(\tau)\,. \end{aligned} \tag{2.15}$$

Combining the equations above, we can write

$$C_{YY}(t) = h(-t) * h(t) * C_{XX}(t). \tag{2.16}$$

This is a very useful equation that relates the auto-correlation function of the output signal to the auto-correlation function of the input signal under the assumption that the input is a stationary process. This will be used in the Section 2.1.2.2 when talking about the Wiener-Khinchin theorem.

As mentioned in Section 2.1.1, the Brownian motion of a particle is described by the Langevin equation [27], which is linear stochastic differential equation. Therefore, we have a LTI system that can be described with the formalism developed above.

The second important concept to mention before introducing the Kubo-Green formula is the definition of admittance as

$$\mathcal{Y}(\omega) \equiv \frac{\tilde{v}(\omega)}{\tilde{F}(\omega)}\,, \tag{2.17}$$

where $\tilde{v}(\omega)$ and $\tilde{F}(\omega)$ are the Fourier transforms of the velocity of and force exerted on the particle, respectively.

With the background knowledge established, the Kubo-Green formula

can be introduced now. The Kubo-Green formula [28–30] connects the admittance to the velocity auto-correlation function $C_{vv}(t)$ in a equilibrium system as

$$\mathcal{Y}(\omega) = \frac{1}{k_B T} \int_0^\infty e^{i\omega t} C_{vv}(t) dt \,. \tag{2.18}$$

Because $C_{vv}(t)$ is real at any time t, we see that

$$\mathcal{Y}^*(\omega) = \mathcal{Y}(-\omega) \,. \tag{2.19}$$

2.1.2.2 The Wiener-Khinchin theorem

Stochastic processes can be analyzed with an important statistical tool known as the power spectral density (PSD), which is defined as [31]

$$S_{\xi\xi}(\omega) \equiv \lim_{T\to\infty} \frac{1}{T} \left| \int_{-T/2}^{T/2} dt \, e^{i\omega t} \, \xi(t) \right|^2 \tag{2.20}$$

for a process $\xi(t)$. For a stationary random process $\xi(t)$, the Wiener-Khinchin theorem [31] states that the PSD and the auto-correlation function form a Fourier transform pair, that is

$$S_{\xi\xi}(\omega) = \int_{-\infty}^{\infty} e^{i\omega t} C_{\xi\xi}(t) \, dt \,, \tag{2.21}$$

$$C_{\xi\xi}(t) = \frac{1}{2\pi} \int_{-\infty}^{\infty} e^{-i\omega t} S_{\xi\xi}(\omega) \, d\omega \,. \tag{2.22}$$

Therefore we can write that the PSD of the velocity of the particle as

$$S_{vv}(\omega) = \int_{-\infty}^{\infty} e^{i\omega t} C_{vv}(t) \, dt. \tag{2.23}$$

Based on the property of the auto-correlation function that $C_v(-t) = C_v(t)$, the properties of the admittance Eq. (2.19) and the Kubo-Green formula Eq.

(2.18), we can write the PSD of the velocity as

$$S_{vv}(\omega) = 2k_B T \Re[\mathcal{Y}(\omega)]\,, \tag{2.24}$$

where $\Re[\mathcal{Y}(\omega)]$ represents the real part of $\mathcal{Y}(\omega)$. Plugging Eq. (2.24) into Eq. (2.22), we can express the velocity auto-correlation function as

$$C_{vv}(t) = \frac{k_B T}{\pi} \int_{-\infty}^{\infty} e^{-i\omega t} \Re[\mathcal{Y}(\omega)]\, d\omega\,. \tag{2.25}$$

In order to obtain the PSD of the position of the particle, let's take the Fourier transform of Eq. (2.16) and use the definition that the PSD is the Fourier transform of the auto-correlation function. We see that in a LTI system when the input $X(t)$ is a stationary process, the PSD of the output signal $Y(t)$ can be written as

$$S_{YY}(\omega) = \tilde{h}^*(\omega)\tilde{h}(\omega) S_{XX}(\omega) = |h(\omega)|^2 S_{XX}(\omega)\,. \tag{2.26}$$

This is a useful property of LTI systems when the input signal is stationary and will also be used in Chapter 5 when deriving the PSD of a suspended diaphragm due to their Brownian motion. Since $v(t) = \dot{x}(t)$, it is easy to show after a Fourier transform that $\tilde{v}(\omega) = -i\omega\tilde{x}(\omega)$. Using the relation of the PSD of the output signal and the PSD of the input signal, we can get

$$S_{vv}(\omega) = \omega^2 S_{xx}(\omega)\,. \tag{2.27}$$

Therefore, the position PSD is

$$S_{xx}(\omega) = \frac{S_{vv}(\omega)}{\omega^2} = \frac{2k_B T\, \Re[\mathcal{Y}(\omega)]}{\omega^2} \tag{2.28}$$

and the position auto-correlation function is

$$C_{xx}(t) = \frac{k_B T}{\pi} \int_{-\infty}^{\infty} e^{-i\omega t} \frac{\Re[\mathcal{Y}(\omega)]}{\omega^2} \, d\omega \, . \tag{2.29}$$

From Eq. (2.27), we can also write the relation between the auto-correlation function of the velocity and position as

$$C_{vv}(t) = \frac{1}{2\pi} \int_{-\infty}^{\infty} e^{-i\omega t} \omega^2 S_{xx}(\omega) \, d\omega = -\frac{\mathrm{d}^2}{\mathrm{d}t^2} C_{xx}(t). \tag{2.30}$$

The Wiener-Khinchin theorem can additionally be applied to connect the PSD to the variance, which is also helpful to analyze Brownian motion. For a stationary random process $\xi(t)$, the variance can be written as

$$\sigma_\xi^2 = \left\langle (\xi(t) - \left\langle \xi(t) \right\rangle)^2 \right\rangle = \left\langle \xi^2(t) \right\rangle - \left\langle \xi(t) \right\rangle^2 = C_{\xi\xi}(0) - \left\langle \xi(t) \right\rangle^2. \tag{2.31}$$

When the mean of the process is zero, we have $\sigma_\xi^2 = C_{\xi\xi}(0)$. Using the Wiener-Khinchin theorem, the relation between the variance and PSD can be expressed as

$$\sigma_\xi^2 = \frac{1}{2\pi} \int_{-\infty}^{\infty} S_{\xi\xi}(\omega) \, d\omega. \tag{2.32}$$

2.1.3 Examples

In this section we will apply the formalism introduced earlier in this chapter to analyze the Brownian motion of two scenarios: a free Brownian particle and a trapped Brownian particle. In both examples we will derive the PSD of position and velocity, the auto-correlation function of position and velocity and the MSD.

2.1.3.1 A free Brownian particle

As mentioned in the first section of this chapter, the Brownian motion a free particle in the air can be described by a Langevin equation Eq. (2.1). If we substitute $v(t)$ for $\dot{x}(t)$ in the equation, Eq. (2.1) becomes

$$m\dot{v}(t) + \gamma v(t) = F_{th}(t)\,. \tag{2.33}$$

Taking Fourier transform of this equation, we can rewrite it as

$$-i\omega m\tilde{v}(\omega) + \gamma\tilde{v}(\omega) = F_{th}(\omega)\,. \tag{2.34}$$

So, the corresponding admittance is

$$\mathcal{Y}(\omega) = \frac{1}{\gamma - i\omega m}\,. \tag{2.35}$$

Using Eq. (2.24), we can express the velocity PSD as

$$S_{vv}(\omega) = \frac{2k_BT\gamma}{\gamma^2 + m^2\omega^2}\,. \tag{2.36}$$

Applying the relation between the position PSD and the corresponding velocity PSD, which is Eq. (2.27), we can get the position PSD as

$$S_{xx}(\omega) = \frac{2k_BT\gamma}{\gamma^2\omega^2 + m^2\omega^4}\,. \tag{2.37}$$

Taking the reverse Fourier transform of the velocity PSD, the auto-correlation function of the velocity can be written as

$$C_{vv}(t) = \frac{k_BT}{m}e^{-|t|/\tau_p}\,, \tag{2.38}$$

where $\tau_p \equiv m/\gamma$ is so called momentum relaxation time. Integrating the above equation twice, the position auto-correlation function is obtained to be

$$C_{xx}(t) = -\frac{k_B T}{m}\left(\tau_p^2 e^{-t/\tau_p} + At + B\right) \text{ when } t \geq 0\,, \tag{2.39}$$

$$C_{xx}(t) = -\frac{k_B T}{m}\left(\tau_p^2 e^{t/\tau_p} + A't + B'\right) \text{ when } t \leq 0\,. \tag{2.40}$$

Since C_{xx} is continuous, we can get $B' = B$. For a stationary process, we also have $C_{xx}(t) = C_{xx}(-t)$; therefore, $\dot{C}_{xx}(t) = -\dot{C}_{xx}(-t)$, which means that $\dot{C}_{xx}(t)$ is an odd function and requires $\dot{C}_{xx}(0) = 0$. The other constants are then solved to be $A = -A' = \tau_p$. Using the derived relations, the position auto-correlation function is finally

$$C_{xx}(t) = -\frac{k_B T}{m}\left(\tau_p^2 e^{-|t|/\tau_p} + \tau_p|t| + B\right)\,. \tag{2.41}$$

So, the MSD of the particle for $t \geq 0$ is

$$\mathrm{MSD}(t) = \frac{2k_B T}{m}\left[\tau_p t - \tau_p^2\left(1 - e^{-t/\tau_p}\right)\right]. \tag{2.42}$$

From the equation above, we can see that at the long time scales where $t \gg \tau_p$, the MSD reduces to

$$\mathrm{MSD}(t) = 2Dt\,, \tag{2.43}$$

where $D = k_B T/\gamma$, which follows Einstein's prediction in 1905 [2]. At short time scales when $t \ll \tau_p$, the MSD simplifies as

$$\mathrm{MSD}(t) = \frac{k_B T}{m} t^2\,, \tag{2.44}$$

which describes the Brownian motion in the ballistic regime where Einstein predicted the existence of the instantaneous velocity. For a Brownian particle at thermal equilibrium, the velocity distribution can be described by the Maxwell-Boltzmann distribution as

$$f(v) = \sqrt{\frac{m}{2\pi k_B T}} \exp\left(-\frac{mv^2}{2k_B T}\right) . \tag{2.45}$$

2.1.3.2 A trapped Brownian particle

In order to study the Brownian motion, especially in the ballistic regime of the particle, we use a technique called an optical tweezer to trap the particle in practice. The principle of the optical tweezer will be covered in Section 2.2. The optically trapped particle experiences an additional trapping force beyond the thermal force and the Stokes drag force that influences the Brownian motion. Assuming that the particle only wiggles around the center of the optical trap and the displacements are small, the trap can be modeled as a harmonic trap with a trapping force that's propotional to the displacement from the center of the trap, $F_{trap} = -\kappa x(t)$, where κ is called trapping strength. Therefore, the Langevin equation that describes the trapped particle with this additional force is

$$m\ddot{x}(t) + \gamma\dot{x}(t) + \kappa x(t) = F_{th}(t). \tag{2.46}$$

This is equation essentially describes a thermally driven damped harmonic oscillator with an oscillation frequency $\omega_1 = \sqrt{\omega_0^2 - (2\tau_p)^{-2}}$ where $\omega_0 \equiv \sqrt{\kappa/m}$ is the undamped angular frequency. The system is under-damped when $\omega_0 >$

$(2\tau_p)^{-2}$, critically-damped when $\omega_0 = (2\tau_p)^{-2}$ and over-damped when $\omega_0 < \Gamma_0/2$. If we replace the $\dot{x}(t)$ with $v(t)$ in the equation and then take a Fourier transform, the equation can be rewritten as

$$-i\omega m\tilde{v}(\omega) + \gamma\tilde{v}(\omega) + \frac{\kappa\tilde{v}(\omega)}{-i\omega} = F_{th}(\omega). \tag{2.47}$$

Therefore, the admittance is

$$\mathcal{Y}(\omega) = \frac{1}{\gamma - i\omega m + i\kappa/\omega}. \tag{2.48}$$

Using Eq. (2.24), the velocity and position PSD are found to be

$$S_{vv}(\omega) = \frac{2k_BT\gamma\omega^2}{(m\omega^2 - \kappa)^2 + \gamma^2\omega^2}\,, \tag{2.49}$$

$$S_{xx}(\omega) = \frac{2k_BT\gamma}{(m\omega^2 - \kappa)^2 + \gamma^2\omega^2}\,. \tag{2.50}$$

Taking the reverse Fourier transform, we can obtain the velocity and position auto-correlation functions when the system is under-damped to be

$$C_{vv} = \frac{k_BT}{m}\left(\cos\omega_1 t - \frac{\sin\omega_1 t}{2\omega_1\tau_p}\right)e^{-t/2\tau_p}\,, \tag{2.51}$$

$$C_{xx} = \frac{k_BT}{\kappa}\left(\cos\omega_1 t + \frac{\sin\omega_1 t}{2\omega_1\tau_p}\right)e^{-t/2\tau_p}\,. \tag{2.52}$$

The theoretical results of C_{vv} and C_{xx} for a silica microsphere with a radius of 1.5 µm at thermal equilibrium with ambient air at a temperature of 300 K at atmospheric pressure are shown in Figure 2.1 and Figure 2.2, respectively.

So the MSD of the particle is

$$\mathrm{MSD}(t) = \frac{2k_BT}{\kappa}\left[1 - e^{-t/2\tau_p}\left(\cos\omega_1 t + \frac{\sin\omega_1 t}{2\omega_1\tau_p}\right)\right]. \tag{2.53}$$

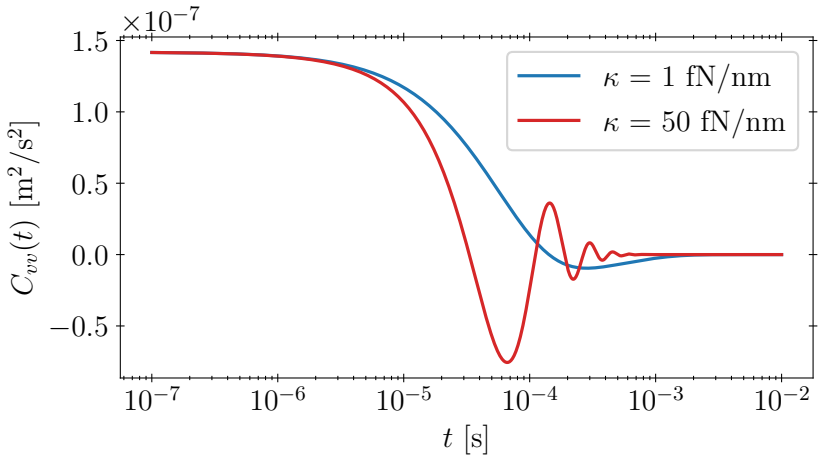

Figure 2.1: Velocity auto-correlation function of a trapped Brownian particle with different trapping strengths.

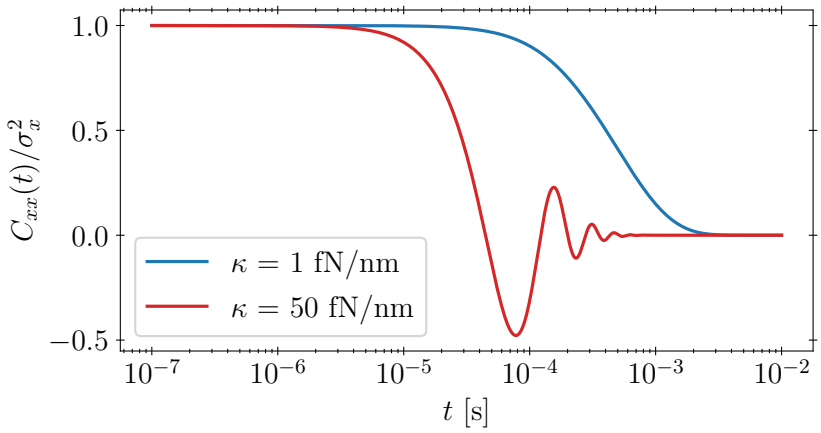

Figure 2.2: Normalized position auto-correlation function of a trapped Brownian particle with different trapping strengths. It is normalized to the variance of the position of the Brownian particle.

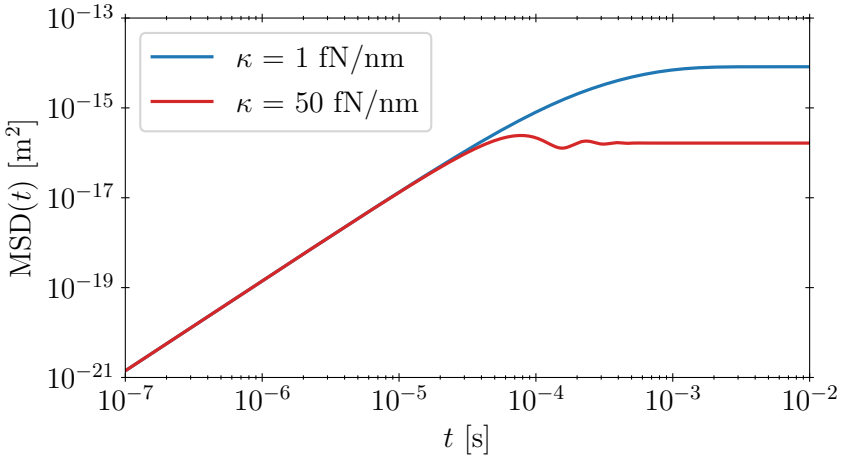

Figure 2.3: Mean squared displacement of a trapped Brownian particle with different trapping strengths.

The theoretical result of the MSD under the same condition as mentioned above is shown in Figure 2.3.

Another approach to analyze the Brownian motion without using the concept of admittance is to directly take the Fourier transform of Eq. (2.46)

$$\tilde{x}(\omega) = \tilde{h}(\omega)\tilde{F}_{th}(\omega)\,, \tag{2.54}$$

where $\tilde{h}(\omega)$ is

$$\tilde{h}(\omega) = \frac{1}{m(\omega_0^2 - \omega^2) + i\gamma\omega}\,. \tag{2.55}$$

Using Eq. (2.26), we can write the position PSD as

$$S_{xx}(\omega) = |\tilde{h}(\omega)|^2 S_{th}(\omega) = \frac{1}{m^2(\omega^2 - \omega_0^2)^2 + \gamma^2\omega^2} S_{th}(\omega)\,. \tag{2.56}$$

As mentioned before, the auto-correlation function of $F_{th}(t)$ is a δ-function with a strength ϵ^2. Since the PSD of F_{th} is the Fourier transform of the

corresponding auto-correlation function, we can express the PSD of F_{th} as $S_{th}(\omega) = \epsilon^2$. Therefore, we can get the position PSD as

$$S_{xx}(\omega) = \frac{\epsilon^2}{m^2(\omega^2 - \omega_0^2)^2 + \gamma^2\omega^2}\,, \tag{2.57}$$

Based on Eq. (2.32) which provides a way to calculate the variance of a signal from the PSD, we can obtain the variance of the position signal as

$$\sigma_x^2 = \frac{1}{2\pi}\int_{-\infty}^{\infty} S_{xx}(\omega)\, d\omega = \frac{\epsilon^2}{2m\omega_0^2\gamma}\,. \tag{2.58}$$

Using the equipartition theorem

$$\frac{1}{2}m\omega_0^2\sigma_x^2 = \frac{1}{2}k_BT\,, \tag{2.59}$$

we can get $\epsilon^2 = 2k_BT\gamma$, which is the same as what was derived in the first subsection about Langevin equation. Therefore, the position PSD can be written as

$$S_{xx}(\omega) = \frac{2k_BT\gamma}{m^2(\omega^2 - \omega_0^2)^2 + \gamma^2\omega^2}\,, \tag{2.60}$$

which is the same as Eq. (2.50). Since the PSD is an even function of ω, we often will limit the range of ω from 0 to $+\infty$ in practice and use two times the PSD as so called one-sided PSD. So the one-sided $S_{th}(\omega)$ and $S_{xx}(\omega)$ can be written as

$$S_{th}(\omega) = 4k_BT\gamma\,, \tag{2.61}$$

$$S_{xx}(\omega) = \frac{4k_BT\gamma}{m^2(\omega^2 - \omega_0^2)^2 + \gamma^2\omega^2}\,. \tag{2.62}$$

The corresponding one-sided velocity PSD is

$$S_{vv}(\omega) = \frac{4k_BT\gamma\omega^2}{(m\omega^2 - \kappa)^2 + \gamma^2\omega^2}\,. \tag{2.63}$$

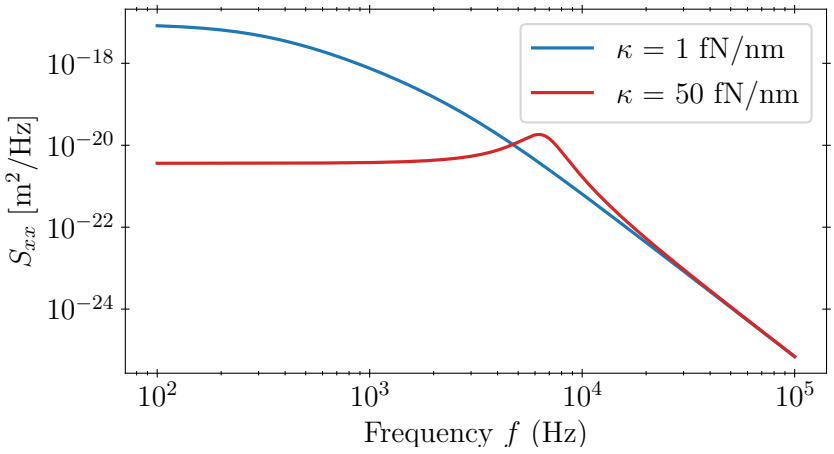

Figure 2.4: Position power spectral density of a trapped Brownian particle with different trapping strengths.

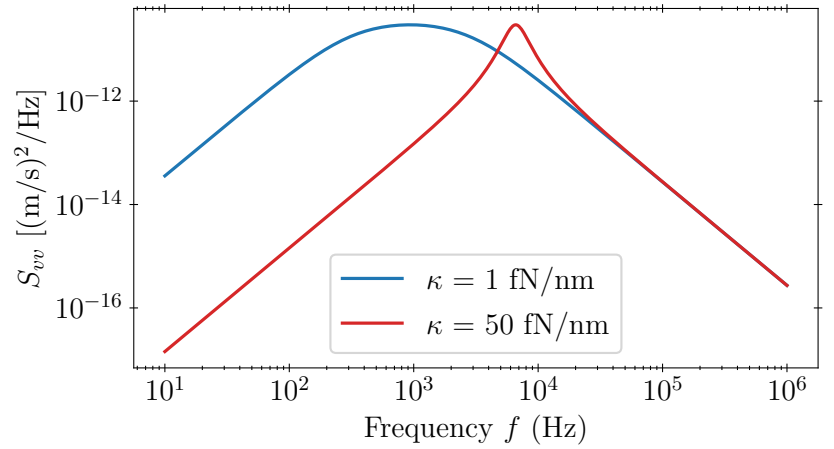

Figure 2.5: Velocity power spectral density of a trapped Brownian particle with different trapping strengths.

The theoretical results of the postion and velocity PSD under the same conditions mentioned above are shown in Figure 2.4 and Figure 2.5.

2.2 Principle of optical tweezers

Optical trapping utilizes radiation pressure which was deduced by James C. Maxwell using his theory of electromagnetism in 1873 [32]. The first experimental measurements of radiation pressure were reported by Pyotr N. Lebedev in 1901 [33] and by Ernest F. Nichols and Gordon F. Hull in the same year [34]. With the invention of laser in 1960 [35], it became possible to focus the light with high spatial and time coherence to a micro-sized spot and permit the generation of large radiation pressures. Suppose a laser beam with a power of $P = 1.5\,\mathrm{W}$ and a wavelength of 1064 nm is directed to and totally reflected off of a silica spherical microsphere with a diameter of 1 µm. The laser would exert a force of $F = 2P/c \approx 10\,\mathrm{nN}$[1] on the microsphere, which is 10^6 times larger in comparison to the gravitational force experienced by the microsphere (around $1 \times 10^{-14}\,\mathrm{N}$).

In 1970, Arthur Ashkin reported the acceleration and trapping of a micro-sized particle using the force of the radiation pressure from a focused laser beam [36]. After further development Ashkin and his colleagues in 1986 reported the first experimental realization of optical trapping of dielectric particles from 10 µm down to 25 nm in water by a single focused laser beam [37]. This is what now is known as an optical tweezer.

[1] c is the speed of light

The optical force the particle experiences in an optical tweezer can be decomposed into two types of forces: the (conservative) gradient force and the (non-conservative) scattering force. The gradient force arises from the gradient of the intensity profile of the laser beam. It is a restoring force that points in the direction of the gradient of the intensity and attracts the particle to the center of the beam. The scattering force, on the other hand, results from the momentum transfer from the photons to the particle as they are scattered or reflected by the particle. It points in the direction of laser propagation and sometimes causes the position of the particle trapped in a optical tweezer to shift downstream from the focus of the laser beam.

The optical force in an optical tweezer can be divided into three regimes, depending on the size of the particle D and the wavelength of the laser λ. These three regimes are the ray optics regime [38] ($D \gg \lambda$), Rayleigh regime [39] ($D \ll \lambda$) and Lorentz-Mie regime [40] ($D \sim \lambda$). In the following sections, we will first provide an intuitive explanation of the principle of the optical tweezer in the ray optics regime followed by a theoretical derivation of the optical force in the Rayleigh regime. Finally, a numerical calculation in the intermediate regime will be shown using Lorentz-Mie theory.

2.2.1 Ray optics regime

Ray optics is a useful approximation of light when the size of an object D is much larger than the wavelength of the laser λ. In this regime, the wave properties, such as diffraction and interference, of the light are ignored and

the propagation of the light is modeled in terms of rays.

To illustrate the idea of optical trapping, let us first explain the gradient force, which is caused by photons refracted in the particle with the ray optics approximation. Figure 2.6 shows a qualitative view of an optically trapped spherical particle in the ray optics regime ignoring the surface reflection from the particle. At equilibrium, the particle is located at the focus of the laser beam as shown in Figure 2.6 (middle). When the particle shifts away from the focus in a direction that is perpendicular to the axis of the laser beam as shown in Figure 2.6 (left), the outward directed beams are refracted along the same direction leading to a restoring force that pulls the particle back to the focus. When the particle moves away from the focus along the direction of laser propagation as shown in Figure 2.6 (right), the outward laser beam becomes more convergent. This causes the photons' momentum component along the propagation axis to increase thus leading to a restoring force that pulls the particle back towards the focus. The behavior is similar when the particle moves axially against the direction of the propagation of the laser. To summarize, the focused laser beam generates a restoring force that acts on the particle in three dimensions, which is directed towards the center of the trap and works to keep the particle trapped at the focus.

Next, we can consider the effect the scattering force adds to the discussion above and study its effect on trapping the particle with the focused laser beam. The scattering force originates from the surface reflection of the laser from the particle and pushes the particle in the direction of propagation

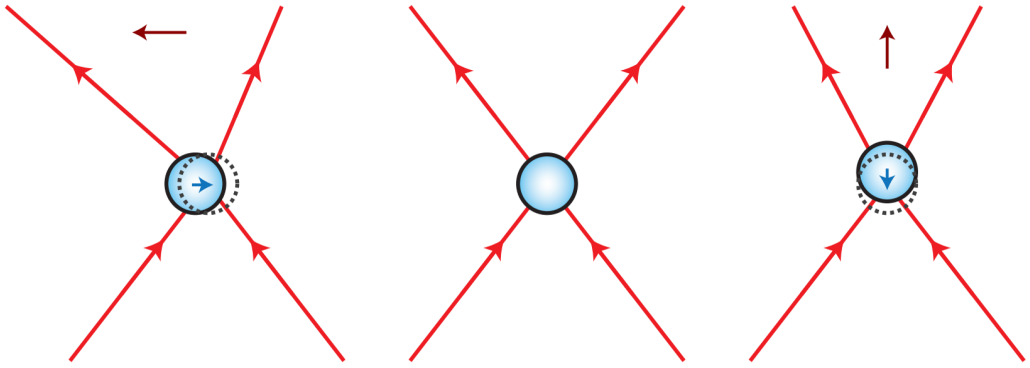

Figure 2.6: The optical force on a trapped spherical particle in the ray optics regime. The dark red arrows mark the direction the particle moves. The blue arrows mark the direction of the restoring force. (left) The particle moves laterally away from the focus. (middle) The equilibrium position with no net force. (right) The particle moves away from the focus in the direction downstream of the axis. Image courtesy of Tongcang Li.

of the laser beam [38]. In the case described above, the scattering force would cause the particle to move away from the focus of the laser beam in the same direction as the beam is traveling. Therefore, the gradient force in the axial direction must be larger than the scattering force to form a stable trap for the particle. A common way to increase the gradient force is to use an objective with a high numerical aperture (NA), which will be shown quantitatively in Section 2.2.3.

2.2.2 Rayleigh regime

When the size of the particle D is much smaller in comparison to the wavelength of the laser λ, analytical expressions can be derived for the scattering and gradient forces exerted by the laser beam on the particle [37, 39].

Below the result of Reference [39] is summarized for the case that a particle with radius R and refractive index n_p is struck by a linearly polarized Gaussian beam propagating in the $\hat{z}$ direction with power P, mode TEM_{00} and a beam waist w_0 at the focus located at the origin. Both the particle and the laser beam are present in a medium with refractive index n_f. The intensity distribution is

$$I(\vec{r}) = \frac{2P}{\pi w^2(z)} e^{-2(x^2+y^2)/w^2(z)}\,, \tag{2.64}$$

where $w(z)$ is the radius of the beam at a distance z from the waist, given by

$$w(z) = w_0\sqrt{1+\left(\frac{z}{z_R}\right)^2}\,. \tag{2.65}$$

Here the $z_R \equiv \pi w_0^2/\lambda$ is the Rayleigh length and $\lambda = \lambda_0/n_f$ is the laser's wavelength in the medium with λ_0 being the laser's wavelength in the vacuum. The scattering force the laser exerts on the particle is

$$\vec{F}_{\mathrm{scat}}(\vec{r}) = \hat{z}\frac{128\pi^5 R^6}{3c\lambda_0^4}\left(\frac{m^2-1}{m^2+2}\right)^2 n_f^2 I(\vec{r}), \tag{2.66}$$

where $m \equiv n_p/n_f$ is the relative refractive index defined as the ratio between the refractive index of the particle and the surrounding medium. The gradient force applied on the particle is then

$$\vec{F}_{\mathrm{grad}}(\vec{r}) = \frac{2\pi n_f R^3}{c}\left(\frac{m^2-1}{m^2+2}\right)\nabla I(\vec{r})\,, \tag{2.67}$$

which creates a trapping potential

$$V(\vec{r}) = -\frac{2\pi n_f R^3}{c}\left(\frac{m^2-1}{m^2+2}\right) I(\vec{r})\,. \tag{2.68}$$

The net optical force the particle experiences is the sum of the scattering and gradient forces. As mentioned above, the axial gradient force must be larger than the scattering force to form a stable trap. Given the equations above, we can discuss the effect some parameters of the particle or medium have on forming a stable trap. Focusing first on the radius R of the particle, we see that the scattering force increases faster than the gradient force for larger radii because the scattering force is proportional to R^6 (Eq. (2.66)), whereas the gradient force is proportional to R^3 (Eq. (2.67)). So it is more difficult to ensure a larger axial gradient force when the particle is bigger. In contrast, Eq. (2.68) shows that the trapping potential scales as R^3 but the average kinetic energy of the particle[2] is independent of the particle size, so it is also difficult to trap the particle stably if the particle is too small.

According to Eq. (2.66) and Eq. (2.67), both the scattering and gradient forces depend on the factor $(m^2 - 1)/(m^2 + 2)$ which increases as m becomes larger. Given the gradient force is linearly proportional to this factor while the scattering force scales quadratically to this factor, this implies that the scattering force grows more rapidly for $m > 1$. As a result it is more challenging to trap a particle when there's a large mismatch between the index of refraction of the particle and the medium [41]. For example, it is harder to trap the same silica particle in air than in water when all other conditions are the same, which is also one of the reasons a dual-beam configuration of the

[2]The average kinetic energy of the particle is $k_B T/2$ in one direction according to the equipartition theorem.

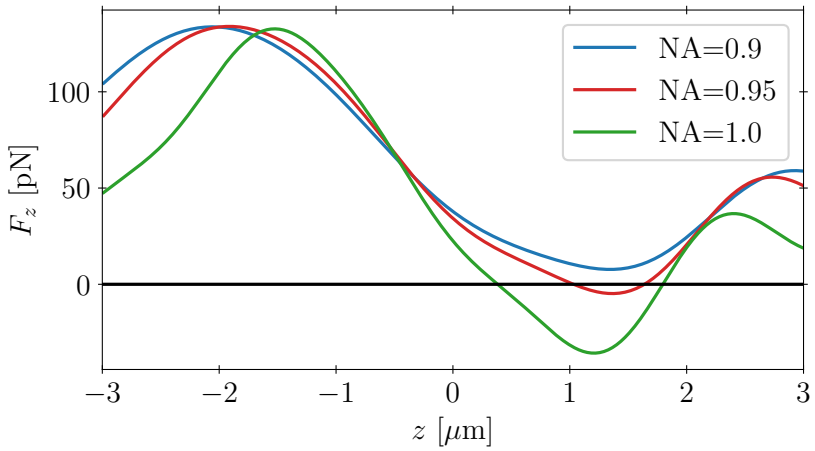

Figure 2.7: The optical force on a silica microsphere with a diameter of 3 µm in air along the axial direction. The force is exerted by a single focusing laser with a total power of 100 mW.

optical tweezer is used in our experiment to trap silica microspheres in air. The details of the setup will be discussed in Chapter 3.

2.2.3 Lorentz-Mie regime

In our experiment, the particles trapped have a range of radii of around 1.5 µm to 2.5 µm that are close to the wavelength of the laser (1064 nm). Particles of this size fall under the Lorentz-Mie regime [40] given the wavelength of the laser. In this case, the optical force can be calculated through the Lorentz-Mie theory, but due to the complexity of the theory, we will only show the numerical results obtained by the computational toolbox developed in Reference [40]. Here we present some simulation results of the optical force exerted on a silica microsphere with a diameter of 3 µm in air with 100 mW of laser power at different NAs using the Optical Tweezers Toolbox in Matlab.

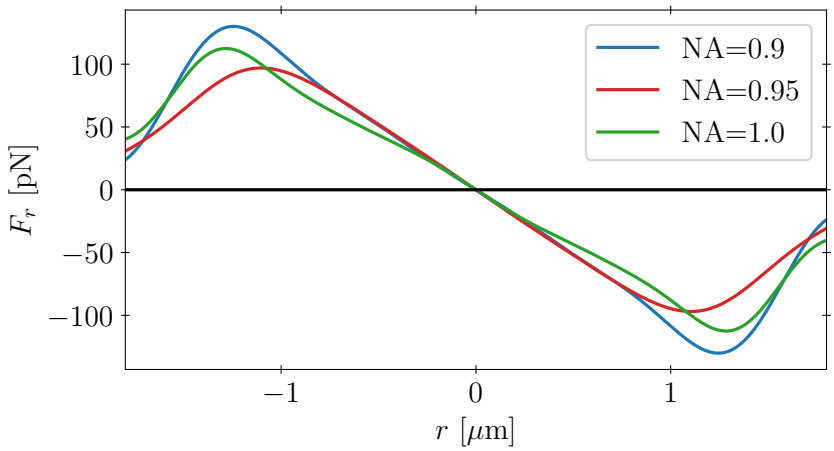

Figure 2.8: The optical force on a silica microsphere with a diameter of 3 µm in air in the radial direction. The force is exerting by a single focusing laser with a total power of 100 mW.

Here we assume there is only one focusing laser beam propagating along the $\hat{z}$ direction.

The optical force along the axial direction is presented in Figure 2.7. To establish a stable trap, the minimum optical force must be negative to ensure that there is a restoring force in both directions axially. Therefore, a high NA is essential to trap a silica microsphere in air with only a single focusing laser beam as it ensures that the gradient force of the beam is greater than the scattering force acting in the axial direction. The optical force in the radial direction, shown in Figure 2.8, behaves more symmetrically as the scattering force only affects the axial direction and causes a bias towards the laser propagation.

Chapter 3

Experiment Setup

In this section we will cover the experiment setup used to study the short-time Brownian motion of an optically trapped silica microsphere in air. In order to trap a microsphere in air, a dual-beam optical trap is needed. In Section 3.1 we first cover the optics setup of this dual-beam optical trap. Specifically, we discuss the procedure to align the propagating and counter-propagating beams in the dual-beam trap. In Section 3.2 we explain how silica microspheres are launched into the trap. Finally, in Section 3.3 the detection system is discussed, including the split-beam detection method and the data acquisition system.

3.1 Optical tweezer setup and alignment

In order to trap a microsphere in air, the most straightforward way is to attempt to use a single-beam optical trap. However, due to the large refractive index mismatch between air and silica, trapping in air is quite challenging as described in Chapter 2 as a result of the enhanced scattering force. According to the simulation in Section 2.2.3, a high NA microscope objective is required for a single-beam optical trap. The first experimental demonstration used an

objective with an NA of 0.95 to trap a 5 µm diameter glass sphere in a single-beam optical trap with a laser power of 40 mW [42]. While possible, a high NA objective has two specific drawbacks: a short working distance and a high cost. Therefore, we chose a dual-beam configuration for our optical trap since it has a lower NA requirement and provides a longer working distance. These benefits come at the cost of requiring careful alignment of the two counter-propagating beams. In principal, the two laser beams should be exactly in line with each other and focused at the same point. Misalignment will cause the trapped microsphere to experience non-conservative forces that can do net work on it [43, 44] and fall outside the formalism developed in Chapter 2. In this section, we first describe the optics setup before discussing the alignment of the dual-beam optical trap with the pinhole alignment method we developed.

3.1.1 Optical setup

Figure 3.1 shows a simplified schematic of the optics setup. We use an Innolite Mephisto laser that outputs continuous 1064 nm laser light for the trapping and detection laser beams. The Mephisto is based on a monolithic Nd:YAG crystal in a Non-Planar Ring Oscillator (NPRO) configuration. It has a maximum power output of 1.5 W, a beam divergence angle (half angle) of 2.3 mrad and a rms intensity noise less than 0.03 % from 10 Hz to 2 MHz. If the "Noise Eater" mode is set to be active, intensity noise centered around 600 kHz to 700 kHz will disappear compared to when the laser is free running. Output power can be adjusted by tuning the injection current. However, in practice

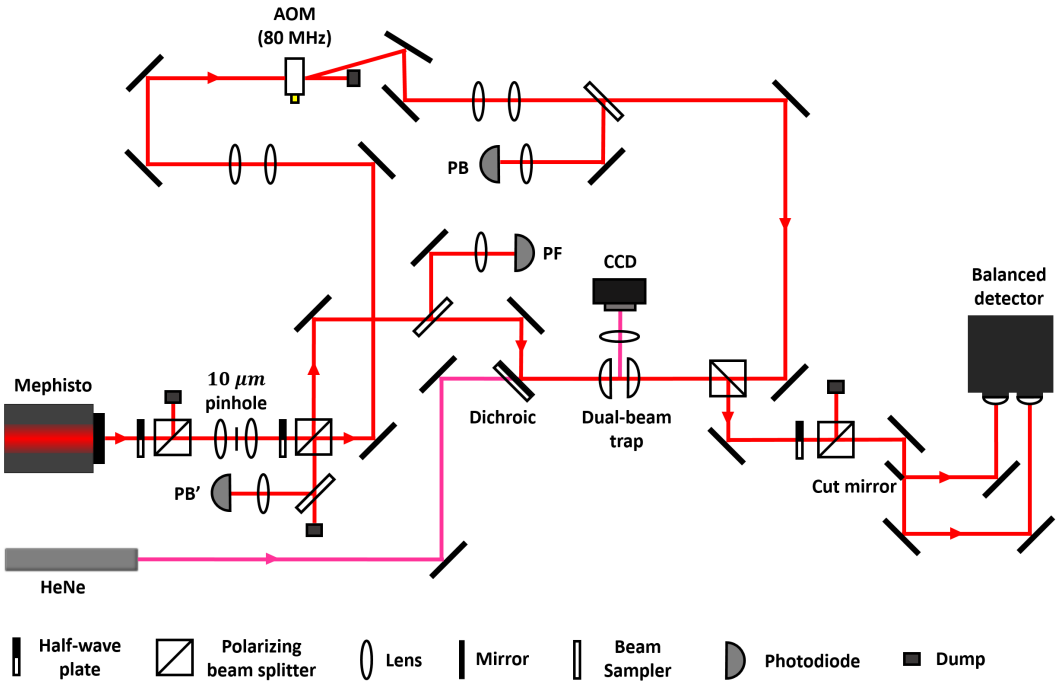

Figure 3.1: The simplified schematic of the optical setup. The solid red lines represent the 1064 nm laser from the Mephisto which is used for trapping and detection. The solid pink line marks the HeNe laser (633 nm) used for imaging the trapped microsphere. The split-beam detection system is depicted at the bottom right of the image.

we usually fix the injection current and instead adjust the power downstream by tuning a half-wave plate (HWP) next to the laser so that power passing through the polarizing beam splitter (PBS) can be changed. After the laser exits the PBS, a telescope expands the size of the beam. In order to improve the beam quality, a pinhole with a diameter 10 µm is inserted at the focus of the two lenses in the telescope to form a spatial filter that removes the higher order modes in the laser beam.

The laser beam is then split into two beams with the second pair of a half-wave plate and a PBS. The s-polarized beam is reflected by the PBS and serves as what we call the forward beam and the p-polarized beam passes through the PBS and serves as the backward beam. The backward beam passes through an acousto-optic modulator (AOM) (IntraAction Corp ATM-801A6 AOM driven by ME-802 modulator driver) to introduce an 80 MHz frequency difference between the forward beam and diffracted first order backward beam. Ensuring that the polarizations of the forward and backward beams are perpendicular to each other in addition to the 80 MHz frequency difference helps us avoid possible interference in the dual-beam trap. Two-mirror configurations are placed in front of both the forward and backward beams to help align them with the aspheric lenses (Thorlabs C330TMD-C) that form the dual-beam trap. By walking the two mirrors, we can control the position and orientation of both the forward and backward beams. The details about the procedure used to align the dual-beam trap will be covered later in this section. In order to monitor the power of the forward beam, a small percentage

of the forward beam is reflected by a beam sampler and measured by a photodiode (PF). For the backward beam a similar method is used to monitor the total power via a photodiode (PB). Power of the backward beam that passes through the dual-beam tweezer is also measured by a photodiode (PB'). After the forward beam passes through the dual-beam optical trap, it is collected for detection via a balanced photo-detector that will be covered Section 3.3 in this chapter.

We also use a 633 nm HeNe laser with an output power around 4 mW for imaging the microsphere trapped in the dual-beam optical tweezer. The imaging beam is aligned to merge with the forward beam via a two-mirror configuration. One of the mirrors used in the two-mirror configuration for the forward beam is selected to be a dichroic mirror, which allows the imaging laser to be transmitted and aligned with forward beam. Finally, a CMOS camera (Thorlabs DCC1545M) is mounted on the side of the dual-beam trap to collect the light scattered by the trapped microsphere.

3.1.2 Pinhole alignment

As mentioned at the beginning of Section 3.1, the dual-beam optical tweezer requires a high degree of alignment. In this section we cover the procedure used in our lab to align the dual-beam optical trap. Micro-sized pinholes play a crucial role in the alignment procedure.

The setup of the dual-beam optical tweezer during the alignment process can be found in Figure 3.2. Both aspheric lenses (Thorlabs E09RMS) that

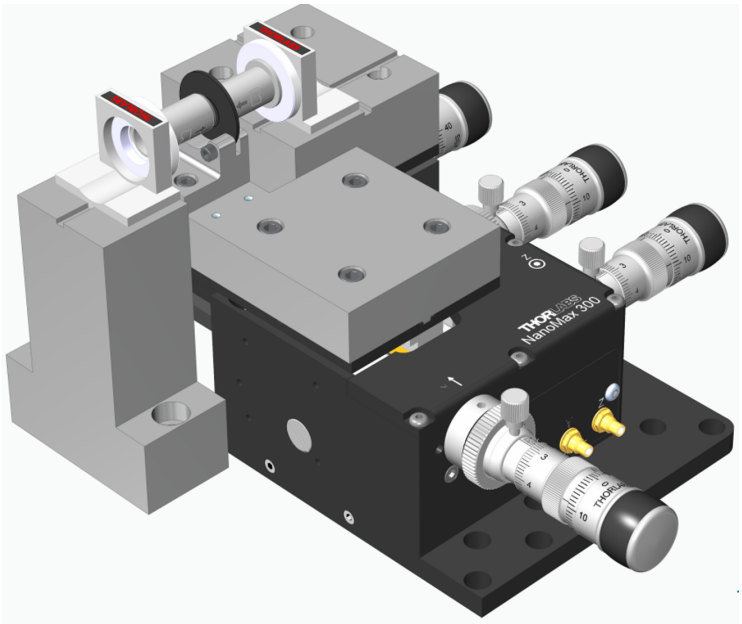

Figure 3.2: The setup of the dual-beam optical tweezer during the alignment process with a pinhole placed between two aspheric lenses. Image courtesy of Logan Hillberry.

form the dual-beam trap are installed in flexure stage mounts from Thorlabs (Thorlabs HCS013). The lens that focuses the forward beam is attached to a custom aluminum block that fixes the orientation and position of the lens. The other lens that focuses the backward beam is mounted on a 3-axis translation stage (Thorlabs MBT616D). A thin alignment pinhole can be inserted between the two aspheric lenses via a second 3-axis translation stage (Thorlabs NanoMax 300).

Aligning the dual-beam optical tweezer is mainly composed of three steps. First, the two mirrors prior to the fixed aspheric lens are adjusted to align the forward beam along the optical axis of the lens by focusing the

forward beam without installing the backward beam's focusing lens and the pinhole. A beam profiler (Thorlabs BP109-UV) is placed after the aspheric lens to image the forward beam. When translating the beam profiler along the beamline away from the focus of the forward beam, the alignment is considered optimal if we observe a clean Gaussian beam with a fixed center but an increasing size. The second step is to install and align the backward beam's aspheric lens on the 3-axis translation stage. Using the forward beam, optimal alignment is achieved when the beam entering and exiting the two-aspheric-lens system have the same size and the beam position stays stationary upon translation of the lens along the optical axis. Likewise, the backward beam can be also be aligned similarly with the other mirror pair to pass through the two aspheric lenses so that the beam size of the backward beam stays the same before and after entering the two-aspheric-lens system.

The final step to align the dual-beam tweezer requires insertion of a micro-sized pinhole between the two aspheric lenses to ensure that the focii are coincident. After installing the pinhole in the translation stage mount, its position is adjusted to maximize throughput of the forward beam. We then fix position of the pinhole and translate the backward beam's aspheric lens to maximize the throughput of the backward beam. This process needs to be done iteratively until reaching the maximum throughput of both beams. Practically, it is easier to start with a larger pinhole with a diameter of 20 µm and then proceed to a smaller one with a diameter of 5 µm after achieving coarse alignment.

3.2 Launching microspheres

In order to trap a microsphere in the optical tweezer, we use a method that release a bunch of microspheres near the center of the trap. As the microspheres fall due to the gravity, one of them will be trapped by the optical tweezer after a couple of attempts.

The microspheres used in the experiment are made of silica (Bangs Laboratories SSD5001) and have an average diameter of 3.17 µm. The Stöber process is used to manufacture these types of microspheres [45]. The microspheres are very spherical with a low dispersion of radius. The details about the silica microspheres are covered in Chapter 4 when describing our results of accurately weighing them. The silica microspheres are initially supplied as a dry powder and are adhered to a glass slide via the van der Waals force by painting them onto the slide. There are also van der Waals forces present between each microsphere. The minimum required force to liberate a microsphere from a flat surface is [46, 47]

$$F_{sphere-flat} = 4\pi R\Gamma\,, \tag{3.1}$$

where R is the radius of the microsphere and Γ is the effective solid surface energy. The minimum required force to separate two identical microspheres is

$$F_{sphere-sphere} = 2\pi R\Gamma\,. \tag{3.2}$$

It is useful to note that the force required to separate two identical microspheres is half of the force needed to remove a single microsphere from a flat

surface. This means that once we develop a method to effectively remove microspheres from a flat surface, there is no need to worry about microspheres still sticking to each other. It has been shown experimentally that it requires 88 nN to separate microspheres of 1 µm in diameter [47]. It follows that it requires approximately 176 nN to launch a microsphere off from a flat silica surface according to Eq. (3.1) and Eq. (3.2). In our experiment we designed a system to sufficiently accelerate the glass slide to release and launch the microspheres [48]. The required acceleration to launch a microsphere with mass m from a flat glass surface can be calculated based on Eq. (3.1) as

$$a = \frac{F_{sphere-flat}}{m} = \frac{3\Gamma}{\rho_{sphere} R^2} \,. \tag{3.3}$$

For a micro-sized silica microsphere, the required force to separate from the slide is on the order of 10^7 to 10^8 m/s^2.

We rebuilt the same setup used in our lab previously to launch the silica microspheres [48], which is essentially a glass slide attached to an ultrasonic transducer depicted schematically in Fig. 3.3. The transducer consists of a piezoelectric ring (APC International 70-2221) and a glass slide with a thickness of 1 mm clamped between two copper plates. Both surfaces of the piezoelectric rings can be viewed as electrodes. The surface that directly contacts the copper plate is electronically grounded. The other surface which has the glass slide serves as an insulator and is connected to the driving circuit. The silica microspheres are applied to the edge of a cover slip which is epoxied to the end of the glass slide.

The driving circuit we use to vibrate the slide attached to the trans-

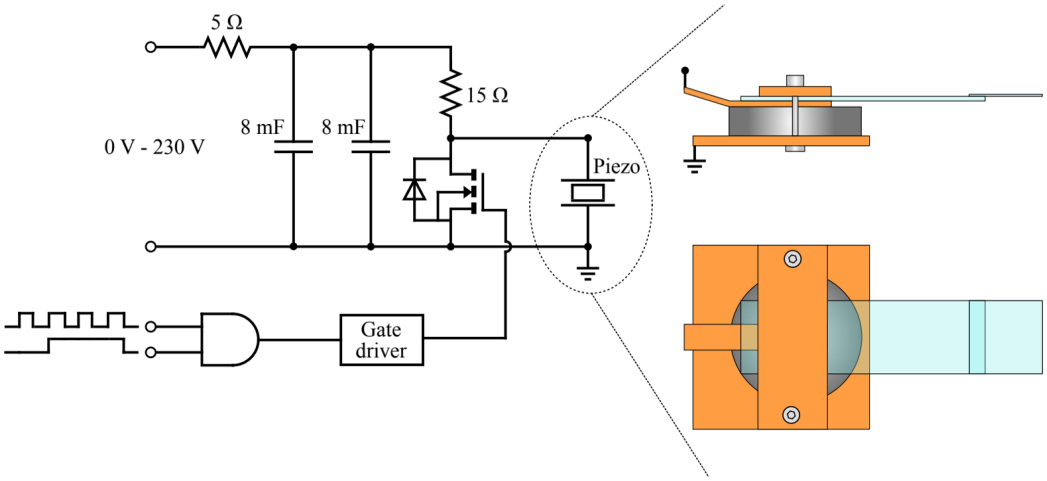

Figure 3.3: The schematic of the driving circuit (left side) to drive the ultrasonic transducer (right side). Image courtesy of Logan Hillberry.

ducer is the same one developed in our lab for previous tweezer experiments in air [48]. Essentially the circuit shown in Figure 3.3 represents a high-power pulsed generator. The two capacitors (8 mF, Digikey 338-1236-ND) are used to store energy from a connected external voltage supply (TDK Lambda 300-5). A high-power MOSFET (Vishay IRFPS40N50L) driven by a high-current, high-speed MOSFET gate driver (Microchip TC4422) serves as a switch to release pulsed current. The piezo ring manufacturer claims that the resonant frequency of the device is approximately 344 kHz. In practice, the gate driver is driven by a square wave with frequencies ranging from 342 kHz to 348 kHz. These waveforms are generated by a Stanford Research Systems DS345 function generator.

The glass slide with silica microspheres is positioned above but very close to the center of the trap. When the piezoelectric ring is activated, the

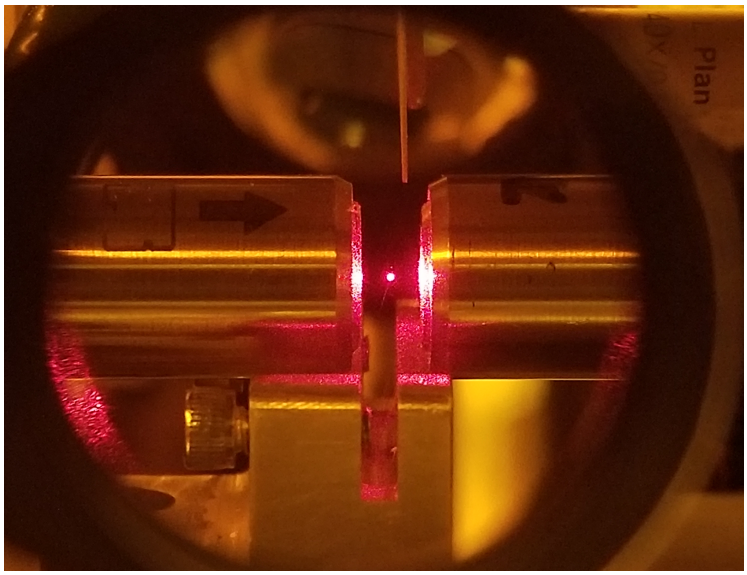

Figure 3.4: A silica microsphere trapped in a dual-beam optical tweezer. The silica microspheres are pre-applied on a cover slip that is brought very close to the center of the trap. Upon ultrasonic vibration, some microspheres are released and descend into the trap. The small red glowing dot observed in the image is from a trapped microsphere scattering the imaging laser.

microspheres begin to detach from the slide and descend before one of them gets trapped in the dual-beam optical tweezer. This process can be monitored visually through an eyepiece as shown in Figure 3.4.

3.3 Detecton system

As mentioned above, the forward beam will be collected after passing through the dual-beam trap to measure the Brownian motion. We use split-beam detection to measure the short-time Brownian motion of the trapped microsphere, which is shown in bottom right of Figure 3.1. The forward beam

of s-polarization is reflected by a PBS and enters the detection system. A D-shaped cut mirror (Thorlabs BBD05-E03) is used to divide the beam into two halves. Each beam is focused into one of the two ports of a balanced photodetector (Thorlabs PDB120C) separately. The balanced photodetector has a bandwidth of 75 MHz and a transimpedance gain of 180×10^3 V/A for wavelengths from 800 nm to 1700 nm. The balanced photodetecor has three signal ports. Two of them output voltage signals that are proportional to the corresponding power each port receives, denoted as V_a and V_b. The third port produces a voltage signal that is proportional to the power difference received between the two photodetector inputs $V_- = V_a - V_b$. As the microsphere wiggles in the trap, it will deviate the forward beam and cause an imbalance between the two halves of the laser beam. Therefore, we measure a voltage signal from the balanced photodetector that is proportional to position of the trapped microsphere along the direction that is perpendicular to the edge of the cut mirror. In practice, the voltage signal V_- is normalized to $V_-/(V_a + V_b)$ to account for the small variations in the detected power when changing the power of the trapping laser.

The temperature of the system is measured by placing a platinum resistance thermometer (Omega RTD-3-F3102-36-T) very close to the center of the dual-beam trap. The temperature data can be read with a temperature monitor (Lakeshore 211) and later be collected with the National Instruments 6259 data acquisition DAQ device with a maximum sampling frequency of 2 MHz, which is also used to collect the data from the photodiodes in order to

monitor the power of the forward and backward beams.

We digitize the analog voltage data from the balanced detector with a high bandwidth (200 MHz) data acquisition (DAQ) card (Gage 1622) that has a vertical resolution of 16 bits. Using this combination of the split-beam detection and the fast digitizer, our group has pioneered measuring the short-time Brownian motion of optically trapped microspheres in both air [8] and liquids [9].

Chapter 4

Weighing an Optically Trapped Microsphere using Short-time Brownian Motion

In this chapter we report the results of a novel weighing metrology experiment utilizing the short-time Brownian motion of a trapped microsphere, which has been published in [49] under the title *Weighing an optically trapped microsphere in thermal equilibrium with air*. The pictures shown in this Chapter are reproduced from this published paper where the author was one of the main contributors. In our experiment a silica microsphere with a radius of 1.5 µm is optically trapped in air at room temperature and atmosphere, which also remains in thermal equilibrium throughout the experiment. The dual-beam configuration of the optical tweezer that is described in Chapter 3 is used. We developed two methods to accurately weigh the microspheres: the spectral method and equipartition method.

In the spectral method we fit the average voltage signal PSD produced via the split-beam detection and extract relevant fitting parameters. By fixing some experimental parameters that can be measured with high accuracy, such as the air temperature T, the air viscosity η and the radius of the silica microsphere R, we can combine them with the fitting parameters to extract other experimental parameters that are difficult to measure accurately, such as the

harmonic trap strength κ, the microsphere mass density ρ and the calibration factor β. Specifically, the microsphere mass can be calculated by combining the radius and the density.

As it will be shown below, the spectral method can provide a very accurate measurement of the microsphere mass, but it requires a large amount of data to generate a smooth PSD necessary for fitting. Therefore, we developed the equipartition method to alleviate the data burden by an order of magnitude while achieving a similar mass uncertainty. The second method utilizes our system's ability to observe the short-time Brownian motion of the microsphere [8], so we only need to calculate the variance of the voltage signal and its derivative. However, the equipartition method demands knowledge of the harmonic trap strength κ or the calibration factor β, so the spectral method must be performed once prior to using the equipartition method. This faster method can be used to monitor the microsphere's mass after calibration has been performed with the spectral method.

In the following of this chapter, we first cover the method to extract parameters by fitting to the PSD in Section 4.1. In Section 4.2 we explain how to use the fitting parameters to calculate the microsphere mass in both the spectral and the equipartition methods. Finally, in Section 4.3 we discuss how noise affects our estimation of the microsphere's mass and provide a summary of all the experimental parameters.

4.1 Power spectral density parameter estimation

As discussed in Chapter 3, the split-beam detection system used in our experiment generates a voltage signal $V(t)$[1] that is proportional to the position $x(t)$ of the trapped microsphere along one the axis as $x(t) = V(t)/\beta$ where β is the calibration factor mentioned above. According to Eq. (2.62), the theoretical PSD (one-sided) of the voltage signal is

$$S_{VV}(\omega) = \beta^2 \frac{4k_B T\gamma}{m^2(\omega^2 - \omega_0^2)^2 + \gamma^2\omega^2}. \tag{4.1}$$

In order to smooth the experimental voltage PSD, ten trials of voltage signal of 0.3 s long each are collected at a sampling rate of 50 MHz during the experiment. We bin-average the signal with non-overlapping blocks of 256 samples to improve the spatial resolution, resulting a new effective sampling rate of 195 kHz. The Bartlett method [50] is performed to significantly reduce the noise in the overall PSD of the signal, at the cost of decreasing the resolution in the frequency domain. The method involves dividing the time domain signal into smaller segments and averaging the PSD of each segment. In practice, we perform 4 averages per trial and a total of 40 averages to the signal. The estimated experimental voltage PSD can be written as $\hat{S}_{VV,k} = \hat{S}_{VV}(f_k)$, where the index k represents the discrete frequencies where the PSD is known.

After obtaining a smooth PSD from the steps above, we can fit to the PSD to extract fitting parameters. First, we temporarily ignore the experimental parameters and only focus on fitting; therefore, it is more convenient

[1]The normalization of the voltage signal is described in Chapter 3

to express Eq. (4.1) as

$$S_{VV}(f;\boldsymbol{\theta}) = \frac{1}{a + bf^2 + cf^4}\,, \tag{4.2}$$

where $\boldsymbol{\theta} \equiv (a, b, c)^\top$ and a, b, c are the fitting parameters. In the following we describe how we apply the maximum likelihood estimation method [51–53] to fit our gamma-distributed PSD data.

Each data point of an n-trial-averaged PSD is subject to a gamma-distributed noise [52], which can be written as

$$\mathcal{P}(\hat{S}_{VV,k}) = \frac{1}{S_{VV,k}} \frac{n^n}{\Gamma(n)} \left(\frac{\hat{S}_{VV,k}}{S_{VV,k}}\right)^{n-1} \exp\left(-n\frac{\hat{S}_{VV,k}}{S_{VV,k}}\right), \tag{4.3}$$

where $\Gamma(n) = (n-1)!$ is the gamma function and $S_{VV,k}$ is the mean value of the distribution. In our case, we have $n = 40$ as the averaged number. The likelihood of measuring the entire data set, denoted as $\hat{S}_{VV}$, given a model, denoted as $S_{VV,k} = S_{VV}(f_k;\boldsymbol{\theta})$, is the joint probability distribution of the data given the model, and can be expressed as

$$\mathcal{P}(\hat{S}_{VV}\,|\,\boldsymbol{\theta}) = \prod_k \mathcal{P}(\hat{S}_{VV,k})\,. \tag{4.4}$$

The goal of maximizing the likelihood can be achieved by minimizing the negative log likelihood of the model, which is

$$\mathcal{L}(\boldsymbol{\theta}, \hat{S}_{VV}) = n\sum_k \left(\log\left[S_{VV}(f_k;\boldsymbol{\theta})\right] + \frac{\hat{S}_{VV}(f_k)}{S_{VV}(f_k;\boldsymbol{\theta})}\right) + C\,, \tag{4.5}$$

where $C = \sum_k \Big[\log\Gamma(n) - n\log n - (n-1)\log\hat{S}_{VV}(k)\Big]$ is a constant and does not affect the result of the minimization. Initial values for the minimization

process can be determined through analytical calculations and numerical implementations [52], which can help to improve the efficiency of finding the best-fit parameters $\hat{\boldsymbol{\theta}} = (\hat{a}, \hat{b}, \hat{c})^\top$ to maximize the likelihood of the data given the model. Figure 4.1(a) displays experimental power spectral densities and the corresponding best-fit curves for two different trapping laser powers.

In order to accurately assess the uncertainty and correlation of the fitted parameters, we use a method inspired by the profile likelihood method [51, 53] to scan a volume of parameter space around the estimated parameters $\hat{\boldsymbol{\theta}}$. This allows us to construct a three-variate probability distribution (as shown in Figure 4.1(b) and Figure 4.1(c)) that we then fit to a three-variate Gaussian distribution

$$\mathcal{P}_G(\boldsymbol{\theta}; \hat{\boldsymbol{\theta}}, \boldsymbol{\Sigma}_{\boldsymbol{\theta}}) = \exp\left[-\frac{1}{2}\left(\boldsymbol{\theta} - \hat{\boldsymbol{\theta}}\right)^\top \boldsymbol{\Sigma}_{\boldsymbol{\theta}}^{-1}\left(\boldsymbol{\theta} - \hat{\boldsymbol{\theta}}\right)\right]. \tag{4.6}$$

The absolute residuals between the actual probability distribution and the fitted Gaussian distribution are consistently less than 1%. The 95th percentile of these residuals is even lower, at less than 0.1%, see Figure 4.2. The variance-covariance matrix of the fitted parameters calculated from the fit is

$$\boldsymbol{\Sigma}_{\boldsymbol{\theta}} = \begin{pmatrix} \sigma_a^2 & \sigma_{ab}^2 & \sigma_{ac}^2 \\ \sigma_{ab}^2 & \sigma_a^2 & \sigma_{bc}^2 \\ \sigma_{ac}^2 & \sigma_{bc}^2 & \sigma_c^2 \end{pmatrix}. \tag{4.7}$$

The square root of the diagonal terms in $\boldsymbol{\Sigma}_{\boldsymbol{\theta}}$ is the uncertainty of the corresponding parameters denoted as σ_i. The correlation between the fitting parameters can be calculated through the off-diagonal terms as $r_{ij} = [\boldsymbol{\Sigma}_{\boldsymbol{\theta}}]_{ij}/(\sigma_i \sigma_j)$, where $i, j = a, b, c$.

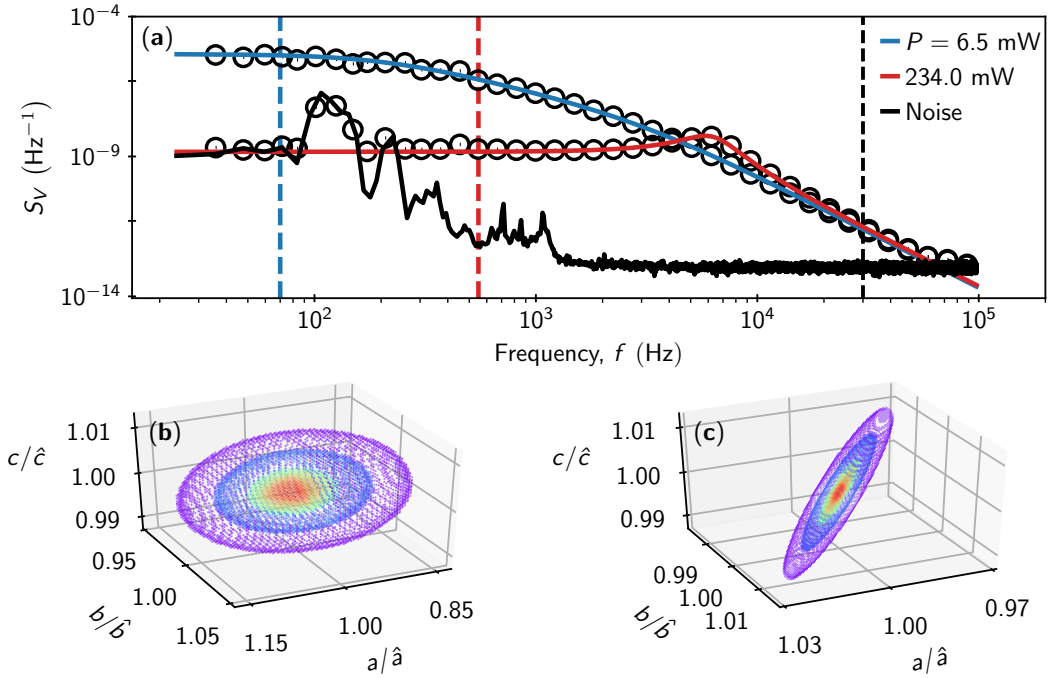

Figure 4.1: (a) Voltage PSD of a trapping laser at two different power levels: 6.5 mW (blue) and 234.0 mW (red). The data points, represented by open circles, are the result of averaging 40 independent measurements and further binned on a logarithmic scale for clarity. The solid lines represent the best fit of the data according to a maximum-likelihood method. The vertical dashed lines indicate the range of the data used in the fit, with the lower bound corresponding to the color of the fitting line and the upper bound represented by a black dashed line. The black solid line represents the noise spectrum, which was measured under the same detection conditions as the other two curves, but without a microsphere present. (b) The isosurface of $\mathcal{P} = \exp(-\mathcal{L})$ as a function of the fitting parameters when the trapping power is 6.5 mW. The isosurfaces represent different levels of Gaussian width, with 3-sigma represented by purple, 2-sigma represented by blue, and a range from the peak to 1-sigma represented by red to green. (c) As in (b) but the trapping power is 234 mW.

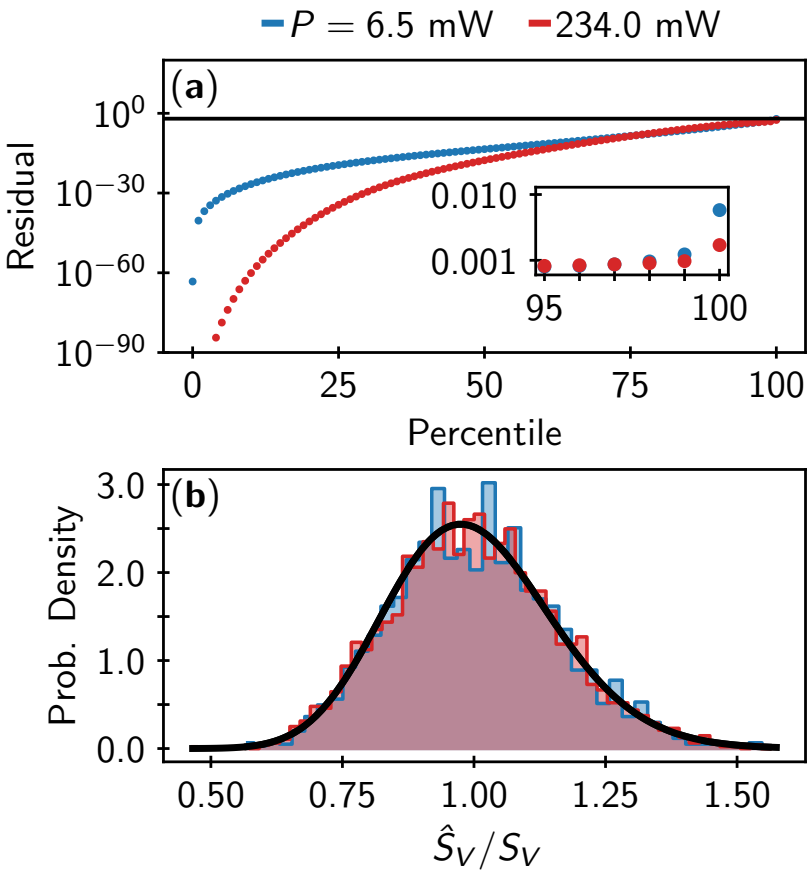

Figure 4.2: (a) The absolute residual between the data obtained from scanning fitting parameters and a three-dimensional Gaussian fit, with the black line indicating that the residual is bounded by 1%. The inset illustrates that the 95th percentile of the residual is bounded by 0.1%. (b) Distribution of the ratio between the measured PSD and the PSD fit, compared to the expected gamma distribution for 40 averaged PSD measurements marked by the solid black line.

After we obtain the best-fit parameters of the PSD, the next step is to deduce the experimental parameters from the fitting parameters. As mentioned at the beginning of the chapter, we will fix the experimental parameters that can be measured relatively accurately as constant, including the air temperature T, air viscosity η and the radius of the silica microsphere R, and then calculate the other experimental parameters, which are the harmonic trap strength κ, the microsphere mass density ρ and the calibration factor β. In the following we describe our methods to accurately measure T, η and R.

As mentioned in Chapter 3, a temperature sensor is placed very close to the center of the dual-beam optical trap (see Figure 3.4) to constantly monitor the temperature of the environment. The total fluctuation of the air temperature is found to be less than 0.05% during the experiment as shown in Figure 4.3(c). According to Sutherland's model [54] the viscosity of air changes only slightly as a function of temperature, see Figure 4.3(d).

As mentioned above, the silica microspheres are manufactured through the Stöber process [45], resulting in very spherical shapes with a low dispersion of the radius. According to a statistical analysis of approximately 200 microspheres observed using a scanning electron microscope (SEM) with the ImageJ program, the radius of the microspheres is approximately 1.51 µm with a uncertainty that is defined as the standard deviation divided by the radius of up to 3.0%, as shown in Figure 4.3(a) and Figure 4.3(b). The analysis of the uncertainty of the radius of the microsphere ensemble confirms a low dispersion of the radius. Additionally, the degree of sphericity of these microspheres, which

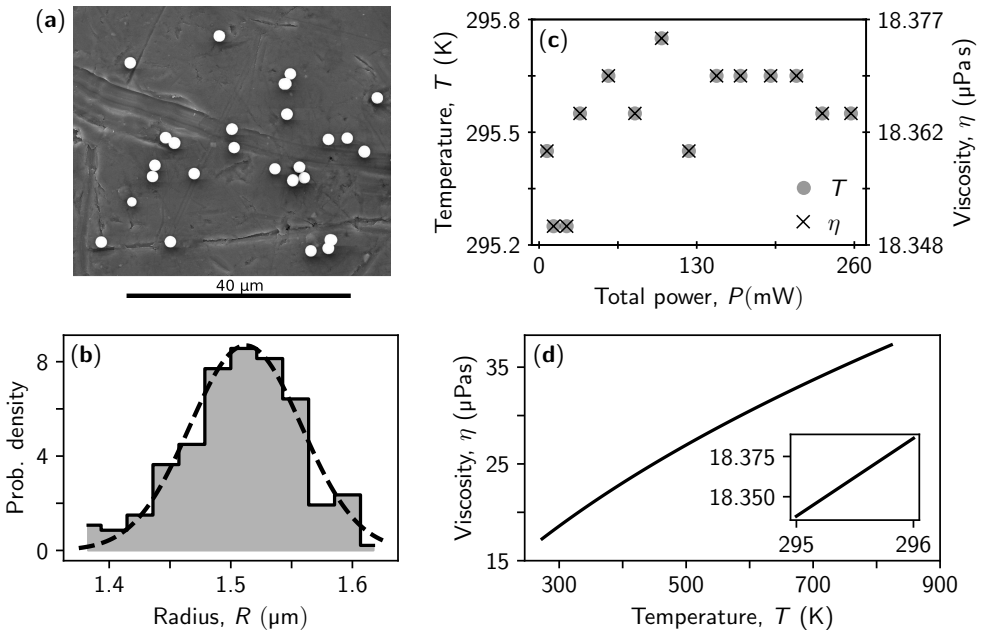

Figure 4.3: (a) Example of one SEM image of the 3 µm microspheres. (b) The distribution of the radius of the microsphere ensemble. (c) Observed temperatures (circles) and the corresponding viscosity (crosses) evaluated with the Sutherland model at different trapping powers. (d) Temperature-dependent viscosity according to the Sutherland model, with the inset showing the linear relationship between viscosity and temperature in the experimentally relevant range.

can be quantified by the aspect ratio a/b, can also be quantified through analysis of the SEM images using ImageJ. The deviation from a perfectly spherical shape can be represented by the parameter $\epsilon = a/b - 1$, and in this case, the value of ϵ is determined to be 0.027. The high degree of sphericity of the silica microspheres, with a small deviation from a perfectly spherical shape, suggests that the aspherical geometry of these microspheres will result in a relatively minor correction to the Stokes friction coefficient $\gamma = 6\pi\eta R$ [55]. In particular, the correction due to aspherical geometry is expected to be less than 1%. As a result, this minor correction can be safely ignored in the following analysis of the uncertainties of the other experimental parameters.

After obtaining the values and uncertainties of the fitting parameters $\boldsymbol{\theta}$ and the experimental parameters R, η, and T that can be measured accurately, the parameters of interest $\boldsymbol{\Theta} = (\kappa, \rho, \beta)^\top$ can be expressed as a function of these parameters $\boldsymbol{\Phi} = (\boldsymbol{\theta}, R, \eta, T)^\top$. If we define

$$d_1 \equiv b + \sqrt{ac}\,, \tag{4.8}$$

$$d_2 \equiv b + 2\sqrt{ac}\,, \tag{4.9}$$

then we have

$$k(\boldsymbol{\Phi}) = 12\pi^2\eta R\sqrt{\frac{a}{d_2}}\,, \tag{4.10}$$

$$\rho(\boldsymbol{\Phi}) = \frac{9\eta}{4\pi R^2}\sqrt{\frac{c}{d_2}}\,, \tag{4.11}$$

$$\beta(\boldsymbol{\Phi}) = \sqrt{\frac{6\pi^3\eta R}{k_B T d_2}}\,. \tag{4.12}$$

The variance-covariance matrix of $\boldsymbol{\Theta}$ can be calculated through the error propagation equation [56]

$$\boldsymbol{\Sigma}_{\boldsymbol{\Theta}} = \boldsymbol{J}_{\boldsymbol{\Theta}} \boldsymbol{\Sigma}_{\boldsymbol{\Phi}} \boldsymbol{J}_{\boldsymbol{\Theta}}^{\top} \tag{4.13}$$

where $\boldsymbol{J}_{\boldsymbol{\Theta}}$ is the Jacobian matirx with elements $(\boldsymbol{J}_{\boldsymbol{\Theta}})_{i,j} = [\partial \Theta_i / \partial \Phi_j]_{\boldsymbol{\theta}=\hat{\boldsymbol{\theta}}}$. Here, $\boldsymbol{\Sigma}_{\boldsymbol{\Phi}}$ is the variance-covariance matrix of the fitting parameters $\boldsymbol{\Phi}$, which includes both the fitting parameters and the measured experimental parameters. Under the assumption of zero correlation between the fitting parameters and the measured experimental parameters, we can approximate $\boldsymbol{\Sigma}_{\boldsymbol{\Phi}}$ as $\boldsymbol{\Sigma}_{\boldsymbol{\Phi}} \approx \mathrm{diag}(\boldsymbol{\Sigma}_{\boldsymbol{\theta}}, \sigma_R^2, 0, 0)$, where σ_R^2 is the variance of the radius R. The uncertainties of the parameters T and η are ignored in this simplification due to their much smaller values compared to the uncertainties of the radius R and the fitting parameters according to the discussion above. The uncertainty of the parameters of interest $\boldsymbol{\Theta}$ can be obtained by taking the square root of the diagonal elements of the variance-covariance matrix $\boldsymbol{\Sigma}_{\boldsymbol{\Theta}}$. If we define

$$u_1 \equiv \frac{3}{16\pi^2 R^3}\,, \tag{4.14}$$

$$u_2 \equiv \frac{1}{2\sqrt{6\pi\eta R k_B T}}\,, \tag{4.15}$$

then the Jacobian matrix can be explicitly written as

$$\boldsymbol{J}_{\boldsymbol{\Theta}} = \frac{6\pi^2 \eta R}{\sqrt{a d_2^3}} \times \begin{pmatrix} d_1 & -a & -\sqrt{a^3/c} & 2ad_2/R & 2ad_2/\eta & 0 \\ -u_1 c & -u_1\sqrt{ac} & u_1 d_1 \sqrt{a/c} & -4u_1 d_2 \sqrt{ac}/R & 2u_1 d_2 \sqrt{ac}/\eta & 0 \\ -u_2\sqrt{c} & -u_2\sqrt{a} & -u_2 a/\sqrt{c} & u_2 d_2 \sqrt{a}/R & u_2 d_2 \sqrt{a}/\eta & -u_2 d_2 \sqrt{a}/T \end{pmatrix}. \tag{4.16}$$

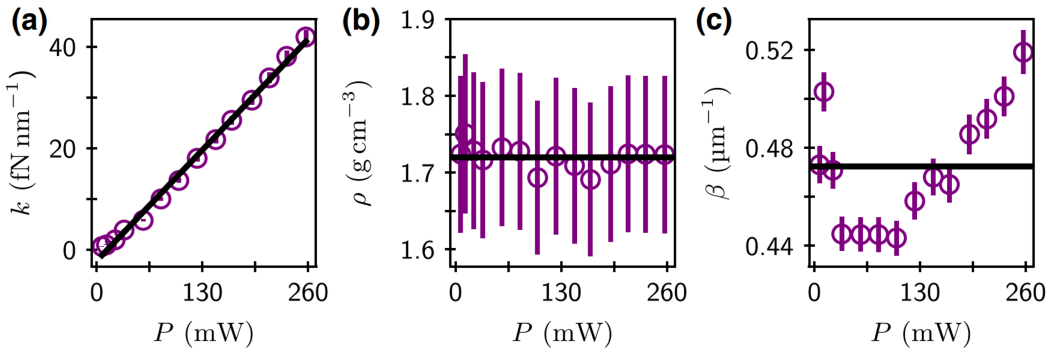

Figure 4.4: The results of the power scan experiment extracted from fitting to the PSD at different trapping powers: trap strength (a), density of the silica microsphere (b) and calibration factor (c). The solid black line represents the linear fitting of the trap strength vs the trapping power in (a) but represents the average of the values (density of the microsphere or the calibration factor) over all the trapping powers in (b) and (c).

Up to this point, we have discussed the necessary analytical tools for extracting the parameters κ, ρ, and β. In our experimental setup, the trapping power of the optical tweezer can be adjusted, allowing us to perform the experiment at various trapping powers and extract the parameters of interest under different conditions. It is worth noting that the same microsphere is used throughout the power-scan experiment. In Figure 4.4, we present the results of the power scan experiment where the trapping power of the optical tweezer varies from 6.5 mW to 257.2 mW. As shown in Figure 4.4(a), the trapping strength κ exhibits a positive linear relationship with the trapping power. By fitting a straight line to the data, we can determine the slope of the graph to be 0.16 fN nm^{-1}/mW.

Before discussing the results of the power-scan experiment on the density of the microsphere ρ, it is important to make distinct what are systematic

and statistical uncertainties when discussing the measured results at different laser powers. In the following discussion, the systematic uncertainty is derived from error propagation of the fitting parameters and the measured experimental parameters at each power. The statistical uncertainty, however, refers to the fluctuation (the standard deviation) of a value that, in principle, should remain constant for different trapping powers.

From Figure 4.4(b), it can be observed that the density of the microsphere ρ, remains relatively constant across different trapping powers with a systematic uncertainty of 5.9% and a statistical uncertainty of 0.9%. However, Figure 4.4(c) shows a relatively larger and non-monotonic fluctuation of the calibration factor β is observed at different trapping powers. According to Eq. (4.1), the magnitude of the voltage PSD is proportional to the product of the square of the calibration factor and the temperature. However, the non-monotonic dependence of the calibration factor on the trapping power, as well as the strong coupling of the microsphere to the environment in our experiment, suggests that the observed behavior is not a result of laser heating of the microsphere. This conclusion is further supported by the fact that our experiment was conducted under different conditions than the experiments in vacuum [57]. Furthermore, the trend of the calibration factor on different powers is reproducible with different microspheres. It suggests that this trend is probably due to the fact that we need to rotate the HWP in front of the PBS to control the laser power that goes into the split-beam detection system because the power limit of this Thorlabs balanced photodetector is only 40 µW

per port.

Once we have obtained the relevant experimental parameters, which are κ, ρ and R, we can use them to calculate the mass of the silica microsphere accurately. This will be discussed in the following section.

4.2 Mass measurement technique

Using the parameters determined in the previous section, we can easily calculate the mass of the microsphere by using the density and radius, which is

$$m_1 = \frac{4}{3}\pi R^3 \rho. \tag{4.17}$$

As mentioned at the beginning of the chapter, we can also use the equipartition therorem, which is $k_B T = m\langle \dot{x}^2 \rangle = \kappa \langle x^2 \rangle$, to calculate the mass of the microsphere. Based on the parameters determined from the section above, the mass can also be written as

$$m_2 = \frac{k_B T}{\langle \dot{V}^2 \rangle} \beta^2 \,, \tag{4.18}$$

$$m_3 = \frac{\langle V^2 \rangle}{\langle \dot{V}^2 \rangle} k \,. \tag{4.19}$$

More specifically, if we define $\mathbf{\Phi'} = (\boldsymbol{\theta}, \langle \dot{V}^2 \rangle, \langle V^2 \rangle, R, \eta)^{\top 2}$, then the three equations of calculating the mass of the microsphere can be re-expressed as

$$m_1(\mathbf{\Phi'}) = 3\eta R \sqrt{\frac{c}{d_2}} \,, \tag{4.20}$$

[2]The mass measurements are independent of temperature T

$$m_2(\mathbf{\Phi'}) = \frac{6\pi^3\eta R}{d_2}\frac{1}{\langle \dot{V}^2 \rangle}\,, \tag{4.21}$$

$$m_3(\mathbf{\Phi'}) = 12\pi^2\eta R\sqrt{\frac{a}{d_2}}\frac{\langle V^2 \rangle}{\langle \dot{V}^2 \rangle}\,. \tag{4.22}$$

As seen in the above expressions, once the fitting parameters have been determined, the mass of the microsphere can be calculated using only the variances of the voltage and the derivative of the voltage, both of which require much less data compared to the spectral method. To obtain the variance of the position and velocity signals in practice, we collect a single trial of data lasting 0.3 s and plot the normalized histograms of the position and velocity. These histograms can then be fit with a Gaussian distribution with the variance as the only adjustable parameter. This allows us to extract the variance of the position and velocity signals as shown in Figure 4.5. The uncertainty of the variance is estimated statistically by taking the standard deviation of 10 trails of data at each trapping power.

Similar to the analysis to extract the uncertainties of the parameters of interest from the fitting parameters and the measured experimental parameters through the variance-covariance matrix, the variance-covariance matrix of vector $\boldsymbol{m} = (m_1, m_2, m_3)^\top$, denoted as $\mathbf{\Sigma}_{\boldsymbol{m}}$, can be calculated from

$$\mathbf{\Sigma}_{\boldsymbol{m}} = \boldsymbol{J}_{\boldsymbol{m}}\mathbf{\Sigma}_{\mathbf{\Phi'}}\boldsymbol{J}_{\boldsymbol{m}}^\top, \tag{4.23}$$

where $\mathbf{\Sigma}_{\mathbf{\Phi'}} = \mathrm{diag}(\mathbf{\Sigma}_{\boldsymbol{\theta}}, \sigma^2_{\langle \dot{V}^2 \rangle}, \sigma^2_{\langle V^2 \rangle}\sigma^2_R, \sigma^2_\eta)$ and $\boldsymbol{J}_{\boldsymbol{m}}$ is the Jacobian matirx with elements $(\boldsymbol{J}_{\mathbf{\Theta}})_{i,j} = [\partial m_i/\partial \Phi'_j]_{\boldsymbol{\theta}=\hat{\boldsymbol{\theta}}}$. If we define

$$v_1 \equiv \frac{1}{4\pi^2}, \quad v_2 \equiv \frac{\pi}{\langle \dot{V}^2 \rangle}, \quad v_3 \equiv \frac{\langle V^2 \rangle}{\langle \dot{V}^2 \rangle}, \tag{4.24}$$

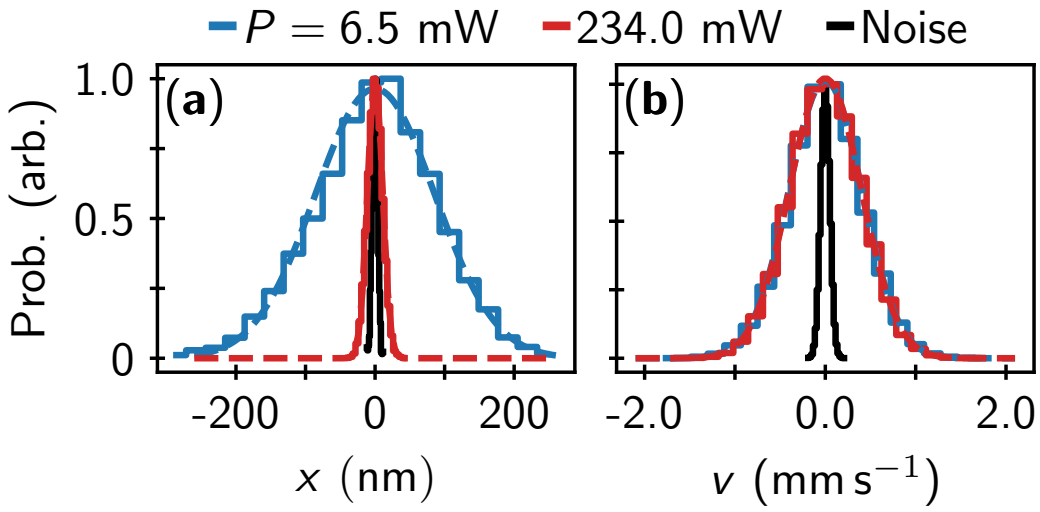

Figure 4.5: Position (a) and velocity (b) probability density of a microsphere over a 0.3 s trial at two different trapping laser powers: 6.5 mW (blue) and 234.0 mW (red) with Gaussian fits (dashed lines) and a histogram of the signal without a microsphere (black line)

then the Jacobian matrix can be written as

$$\boldsymbol{J_m} = \frac{6\pi^2\eta R}{\sqrt{ad_2^3}}\times \begin{pmatrix} -v_1 c & -v_1\sqrt{ac} & v_1 d_1\sqrt{a/c} & 0 & 0 & 2v_1 d_2\sqrt{ac}/R & 2v_1 d_2\sqrt{ac}/\eta \\ -v_2\sqrt{c/d_2} & -v_2\sqrt{a/d_2} & -v_2 a/\sqrt{cd_2} & -v2\sqrt{ad_2}/\langle \dot{V}^2\rangle & 0 & v_2\sqrt{ad_2}/R & v_2\sqrt{ad_2}/\eta \\ v_3 d_1 & -v_3 a & -v_3\sqrt{a^3/c} & -2v_3 a d_2/\langle \dot{V}^2\rangle & 2v_3 a d_2/\langle V^2\rangle & 2v_3 a d_2/R & 2v_3 a d_2/\eta \end{pmatrix}. \tag{4.25}$$

The systematic uncertainties of the mass measurements are calculated by taking the square root of the variance-covariance matrix $\boldsymbol{\Sigma_m}$.

In order to accurately calculate the variances of the position and velocity signals, it is important to carefully consider the length of the data used in the calculation. The uncertainty in the estimate of the variance decreases as the length of the uncorrelated data increases, following the scaling of $\tau^{-1/2}$, where τ is the length of the uncorrelated voltage trace. However, in our case,

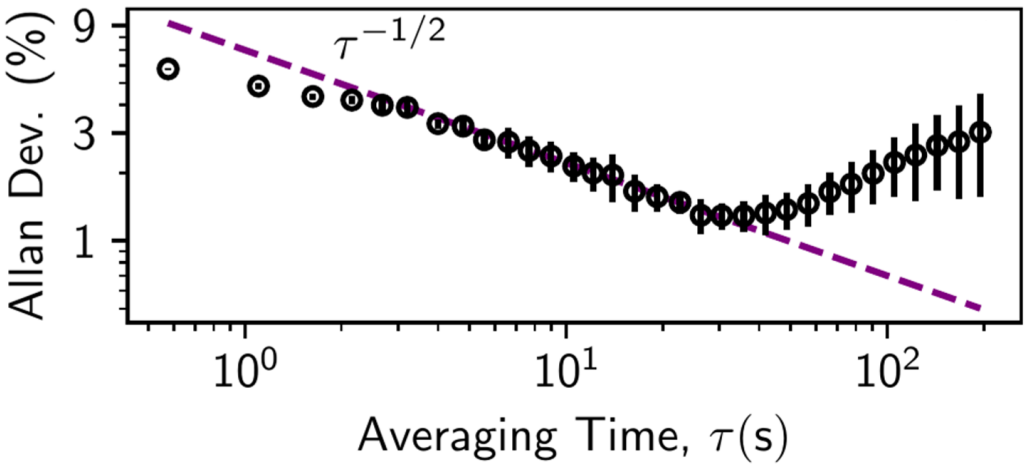

Figure 4.6: The relative Allan deviation normalized to the value of variance corresponding to the minimum Allan deviation. The dashed purple line represents the $\tau^{-1/2}$ trend of the uncorrelated data.

the data is correlated when the time scale is shorter than the momentum relaxation time $\tau_p = m/\gamma$, but slow drifts may contaminate the signal at longer time scales. Therefore, Allan-deviation stability analysis [58–61] is used to determine the optimal time to estimate the variance. Figure 4.6 shows the result of the Allan-deviation experiment with 22.8 mW of trapping power calculated from a 14-minute voltage trace. We can see that the Allan-deviation decreases with increasing averaging time up to 30 s before slow drifts start to affect the result after that point. Based on this, it is estimated that roughly 100 independent mass measurements can be performed using a single trial of data that is 0.3 s in length.

Using the techniques mentioned above, the mass of the same silica microsphere was estimated at 14 different trapping powers. The results are

summarized in Figure 4.7. The average mass was calculated for each method, yielding $\bar{m}_1 = 24.8$ pg, $\bar{m}_2 = 25.1$ pg, and $\bar{m}_3 = 27.4$ pg. Here we denote the systematic uncertainty of the mass measurement as $\sigma^{\text{sys}}_{m_i}$ and statistical uncertainty as $\sigma^{\text{stat}}_{m_i}$, where $i = 1, 2, 3$. The spectral method (m_1) provides the most accurate measurement result with smallest systematic and statistical uncertainties ($\sigma^{\text{sys}}_{m_1}/\bar{m}_1 = 3.0\,\%$ and $\sigma^{\text{stat}}_{m_1}/\bar{m}_1 = 0.9\,\%$). For the equipartition method, m_2, which uses the variance of the voltage derivative, yields a similar result (around 1 % shift) to m_1 with slightly higher systematic and statistical uncertainties ($\sigma^{\text{sys}}_{m_2}/\bar{m}_2 = 4.1\,\%$ and $\sigma^{\text{stat}}_{m_2}/\bar{m}_2 = 1.6\,\%$). The other method based on the equipartition theorem, m_3, using the variance of the voltage produces results with the largest systematic and statistical uncertainties ($\sigma^{\text{sys}}_{m_3}/\bar{m}_3 = 6.7\,\%$ and $\sigma^{\text{stat}}_{m_3}/\bar{m}_3 = 3.0\,\%$). Important to note also is that, the results of m_3 have a roughly 10 % shift of the value of the mass of the microsphere for at almost all trapping powers compared to m_1 and m_2. A possible explanation for this shift will be provided in the next section.

4.3 Discussion and summary

In this section, we will first discuss the reason why m_3 provides a result of the mass measurement with a large shift compared to m_1 and m_2. Then we will summarize all the measured quantities in the experiment and the order of using the spectral and the equipartition method in application.

From Figure 4.1(a) we can see that there are many low-frequency noise contaminants in our system that persist even when the trapped bead is not

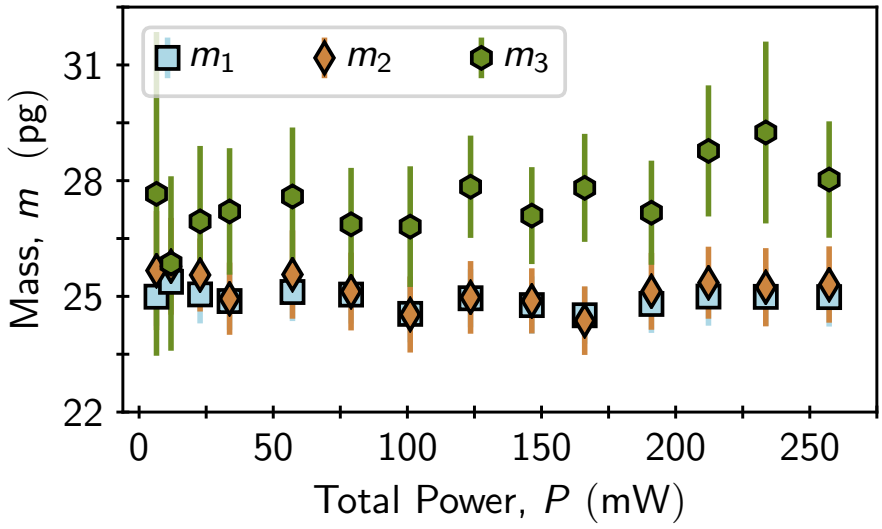

Figure 4.7: Summary of the three mass measurement methods at different trapping powers

present, including but not limited to laser pointing noise, acoustic noise due to close proximity to a chilled water pipe line and so on. The most prominent of these noise sources is centered around 120 Hz and extends from 70 Hz to 170 Hz. When using spectral analysis to fit the voltage PSD, we can adjust the fitting range to exclude these low-frequency noise peaks and improve the accuracy of the results. But when we directly calculate the variance of the voltage signal, the results are affected by these low frequency noise components based on Eq. (2.32). To estimate the effect of the noise on the variance of the voltage signal, the voltage PSD can be viewed as a summation of the PSD due to the Brownian motion of the microsphere and the noise PSD. According to Eq.

(2.32), we can approximate

$$\left\langle V^2 \right\rangle \approx \left\langle V^2 \right\rangle_{\text{Brownian}} + \int_{70\,\text{Hz}}^{170\,\text{Hz}} S_{VV}^{\text{noise}}(f)\,\mathrm{d}f\,, \tag{4.26}$$

where $\left\langle V^2 \right\rangle$ is the variance of the measured voltage signal and $\left\langle V^2 \right\rangle_{\text{Brownian}} = k_B T \beta^2 / k$ is calculated by using the parameters from the spectral method. It is worth noting that we only consider the dominant noise peak in the equation above. Figure 4.8(a) shows the result of the excess variance defined as $\Delta\left\langle V^2 \right\rangle \approx |\left\langle V^2 \right\rangle - \left\langle V^2 \right\rangle_{\text{Brownian}}|$ and the value of the second integration in Eq. (4.26) at different trapping powers. The 10 % discrepancy between m_3 to m_1 and m_2 could be explained by the low-frequency noise on average.

Similar to Eq. (2.27), the relation between the voltage PSD and the voltage derivative PSD can be stated as

$$S_{\dot{V}\dot{V}}(f) = (2\pi f)^2 S_{VV}(f), \tag{4.27}$$

which implies that the high-frequency components contribute more to the voltage derivative PSD. This also explains the smaller drift m_2 experiences in comparison to m_3 since there is more low-frequency noise in our system than high-frequency noise. As shown in Figure 4.8(b), we can apply a similar analysis to estimate the excess variance of the voltage derivative, $\Delta\left\langle \dot{V}^2 \right\rangle$. We find that the excess variance of the voltage derivative is approximately 2 % of the voltage derivative variance calculated by using the parameters from the spectral method, which is consistent with the expected contribution from noise with frequencies above 80 kHz when integrated using the noise PSD.

To summarize the results of this chapter, Table 4.1 presents a summary

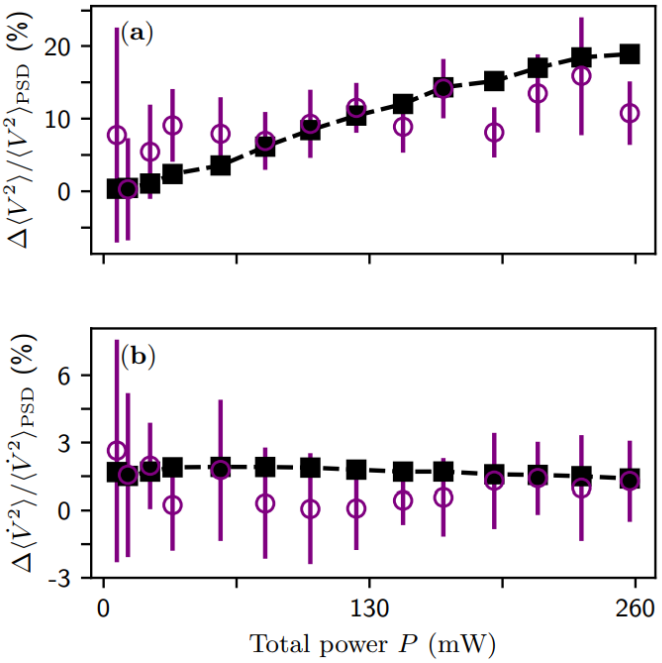

Figure 4.8: The excess variance of the voltage signal (a) and the voltage derivative signal (b), denoted by purple circles. The black squares represent the value of the integration of the noise term in both cases. The error bars are the standard deviation of 10 trials of data at each trapping laser power.

of the experimental parameter values and their uncertainties. The spectral method can measure the optically trapped silica microsphere's mass with 3.0 % uncertainty with a 3 s trail of data. This measurement provides a calibration of our system that we can proceed to in combination with the equipartition theorem to rapidly measure the mass of the microsphere in 0.3 s with uncertainties of 4.1 %. Our experiment is performed in a strong environmental coupling scenario, which suggests application for air-based sensing. This fast measurement method allows us to study a system of changing mass with high accuracy.

Table 4.1: Table of values and uncertainties. Reported values are the average over the power scan experiment, except for κ and $\langle V^2 \rangle$ for which we report the range since these quantities scale linearly with trapping power. The relative systematic uncertainties averaged over the power scan experiment and the statistical uncertainties are included, where applicable.

Quantity	**Value**	**Uncertainty** (%)		**Unit**
		Systematic	Statistical	
R	1.51	2.9	-	µm
η	18.295	0.04	-	µPa s
T	295.50	0.05	-	K
$\langle \dot{V}^2 \rangle \times 10^3$	36.4	2.4	-	μs^{-1}
$\langle V^2 \rangle \times 10^3$	(0.03, 1.53)	8.9	-	Arb.
k	(0.66, 49.1)	3.1	-	$fN\,nm^{-1}$
ρ	1.72	5.9	0.9	$g\,cm^{-3}$
β	0.47	1.6	5.0	μm^{-1}
m_1	24.8	3.0	0.9	pg
m_2	25.1	4.1	1.6	pg
m_3	27.4	6.7	3.0	pg

Chapter 5

Theory for the Brownian Motion of Suspended Diaphragms

In this chapter we are going to extend the theory of the Brownian motion from a single particle to a suspended diaphragm. Unlike the microspheres that require an optical tweezer for trapping, suspended diaphragms are naturally "trapped". For all the discussion in this dissertation, we will focus on the out-of-plane motion of the suspended diaphragm, which can be viewed as a summation of an infinite number of resonant modes. The trapping strengths and the resulting resonant frequencies are determined by the mechanical properties of the diaphragm. Section 5.1 details the model that describes the out-of-plane motion of circular suspended diaphragms. Specifically, we analyze the "intermediate" regime where both the bending rigidity and the surface tension play comparable roles. We present a numerical method that uses the first resonant frequency as well as some parameters related to the mechanical properties of the diaphragm to solve the resonant mode shapes of the diaphragm in the intermediate regime. After solving for the fundamental resonant modes of the suspended diaphragm, we decompose its out-of-plane motion as well as the thermal force to a summation of the fundamental resonant modes and apply the techniques covered in Chapter 2 to derive the

corresponding statistical tools to analyze its Brownian motion.

5.1 Out-of-plane motion of suspended diaphragms

In this section we will talk about the out-of-plane motion of a suspended diaphragm and solve for the fundamental resonant modes assuming the edges of the diaphragm are clamped. This will provide the tools necessary to analyze the Brownian motion of the diaphragm described in Section 5.2.

Consider a thin circular diaphragm of with a radius of a in air. The diaphragm is suspended in the $xy-$plane. If we assume it is a thin solid plate of uniform isotropic material with a constant thickness and its tension is also uniformly distributed, then the motion of the diaphragm in the z direction can be described by the following equation [62–64]

$$D\nabla^4 z - \Sigma h \nabla^2 z + \mu \dot{z} + \rho h \ddot{z} = F_{th}(x, y, t)\,, \tag{5.1}$$

where $z(x, y, t)$ describes the transverse displacement of an element $\rho\, dx\, dy$ on the surface of the membrane in the $xy-$plane along the z direction. The density and the thickness of the diaphragm are designated as ρ and h, respectively. The two-dimensional gradient operator is defined as $\nabla = \frac{\partial^2}{\partial x^2} + \frac{\partial^2}{\partial y^2}$. The bending stiffness of the diaphragm can be described by its Young's modulus and Poisson's ratio, E and ν, respectively as $D = Eh^3/12(1-\nu^2)$. The in-plane tension of the diaphragm is represented as Σ while μ corresponds to the damping coefficient of forced vibration. Finally, the diaphragm's random collisions with air molecules are captured by the stochastic process $F_{th}(x, y, t)$.

In order to analyze the Brownian motion of the diaphragm, the normal mode method will be employed [18, 64]. The transverse motion of the diaphragm will be decomposed into the fundamental resonant modes which depend on the boundary condition. Initially, we will omit the damping term $\mu\dot{z}$ and the stochastic force $F_{th}(x, y, t)$. This simplification of Eq. (5.1) describes the free undamped transverse motion of a diaphragm as

$$D\nabla^4 z - \Sigma h\nabla^2 z + \rho h\ddot{z} = 0\,. \tag{5.2}$$

In the equation above, the first and second terms capture the effects of the diaphragm's bending rigidity and tension, respectively. The contribution that each term has on the transverse motion of the diaphragm depends on many parameters including in-plane tension, size and thickness of the diaphragm and so on. In order to compare the roles of these two terms and also provide guidance on which term can be safely ignored in some circumstances, we will talk below about the resonant frequencies in the two cases when $D = 0$ and $\Sigma = 0$ separately. When $D = 0$, we have [18, 22]

$$f_{mn}|_{D=0} = \frac{1}{2\pi}\sqrt{\frac{\Sigma}{\rho}}\,\frac{\gamma_{mn}}{a}\,, \tag{5.3}$$

where γ_{mn} is a constant and it varies for different resonant modes. Some values of γ_{mn} are $\gamma_{01} = 2.405$, $\gamma_{11} = 3.832$, $\gamma_{21} = 5.135$, $\gamma_{02} = 5.520$, etc. When $\Sigma = 0$, the resonant frequencies of each mode are [22]

$$f_{mn}|_{\Sigma=0} = \frac{1}{2\pi}\sqrt{\frac{D}{\rho h}}\,\frac{\beta_{mn}^2}{a^2}\,. \tag{5.4}$$

Table 5.1: The ratio of higher resonant frequencies to the first resonant frequency f_{01} when $D = 0$ and $\Sigma = 0$.

Ratio	**Uncertainty**	
	$D = 0$	$\Sigma = 0$
f_{11}/f_{01}	1.593	2.082
f_{21}/f_{01}	2.135	3.415
f_{02}/f_{01}	2.295	3.893

where β_{mn} is a constant and it varies for different modes. Some values of β_{mn} are $\beta_{01} = 3.196$, $\beta_{11} = 4.611$, $\beta_{21} = 5.906$, $\beta_{02} = 6.306$, etc. Table 5.1 shows the ratio of the frequencies corresponding to higher resonant modes to the first resonant frequency. It can be seen that the ratio is larger for the case when $\Sigma = 0$ compared to when $D = 0$. As it is shown below, the ratio when both terms are included should fall between the corresponding two values when only one of the terms is present.

The ratios between the fundamental resonant frequencies when only taking one term into account can provide insight about the role each term has on dynamics of the diaphragm. Consider a circular graphene diaphragm with density $\rho = 2.267\,\mathrm{g/cm^3}$, radius a, thickness h, Young's modulus $E = 0.9\,\mathrm{TPa}$, Poisson' ration $\nu = 0.165$, and in-plane tension $\Sigma \approx 1\,\mathrm{MPa}$ [65], we can plot the ratio of the first resonant frequency when $D = 0$ to when $\Sigma = 0$, which is $f_{01}|_{D=0}/f_{01}|_{\Sigma=0}$, as a function of the radius of the diaphragm for different thicknesses of 1 nm, 2 nm and 3 nm, as shown in Figure 5.1. We can see from the figure below that when the radius of the diaphragm is on the order of a micron, the bending rigidity and the in-plane tension are comparable to each other. For example, in the case of a graphene diaphragm with a thickness of

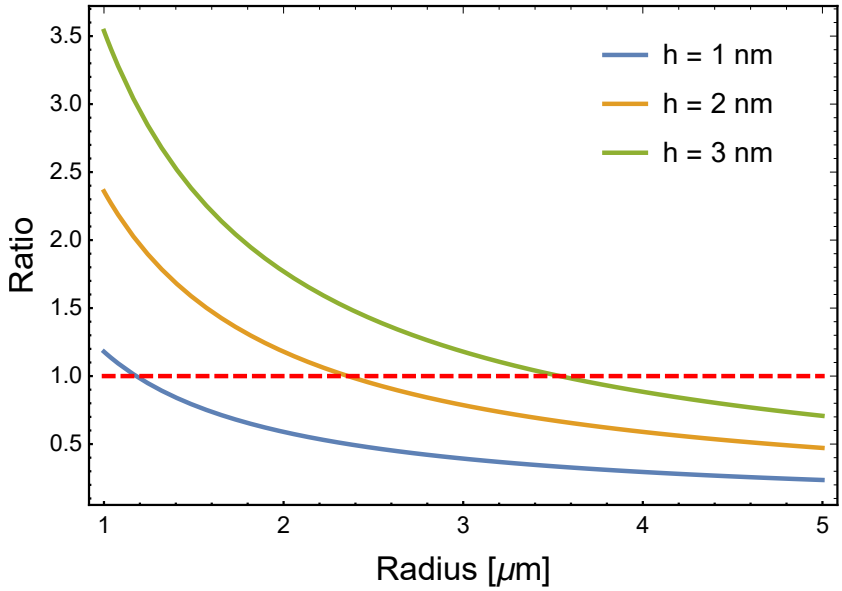

Figure 5.1: The ratio of the first resonant frequency when $D = 0$ to when $\Sigma = 0$ ($f_{01}|_{D=0}/f_{01}|_{\Sigma=0}$) as a function of the radius of the diaphragm for different thicknesses of 1 nm, 2 nm and 3 nm. The intersection between the solid line and the dashed red line indicates when the two frequencies equal to each other.

2 nm, the two resonant frequencies are nearly equal to each other when the radius of the diaphragm is around 2.5 µm. This point of equivalence will shift to larger radii for thicker graphene diaphragms. In these scenarios, it is difficult to ignore either of the terms; therefore, we will detail the procedures to acquire the fundamental resonant modes and frequencies with both terms present.

Here, the procedure to solve the fundamental resonant modes for bounded circular thin diaphragms when $\Sigma = 0$ provided in Reference [22] is adapted to solve Eq. (5.2) when both Σ and D are present. The radius and thickness of the graphene diaphragm are chosen to be experimentally relevant values of 3.25 µm

and 2.1 nm, respectively. All other parameters are the same as what was listed above save for the surface tension Σ which is unknown. First, we use separation of variables in cylindrical coordinates, which is $z(r,\theta,t) = Z(r,\theta)T(t)$, and plug into Eq. (5.2) to obtain two independent equations

$$\frac{\mathrm{d}^2 T}{\mathrm{d}t^2} + \omega^2 T = 0\,, \tag{5.5}$$

$$\nabla^4 Z - \kappa^2 \nabla^2 Z + \lambda^4 Z = 0\,, \tag{5.6}$$

where

$$\kappa^2 \equiv \frac{\Sigma h}{D} \tag{5.7}$$

and

$$\lambda^4 \equiv \frac{\rho h \omega^2}{D}. \tag{5.8}$$

If we then define

$$\alpha_{\pm}^2 \equiv \frac{\sqrt{\kappa^4 + 4\lambda^4} \pm \kappa^2}{2}\,, \tag{5.9}$$

then Eq. (5.6) can be written as two separate equations:

$$\frac{\partial^2 Z}{\partial r^2} + \frac{1}{r}\frac{\partial Z}{\partial r} + \frac{1}{r^2}\frac{\partial^2 Z}{\partial \theta^2} + \alpha_-^2 Z = 0\,, \tag{5.10}$$

$$\frac{\partial^2 Z}{\partial r^2} + \frac{1}{r}\frac{\partial Z}{\partial r} + \frac{1}{r^2}\frac{\partial^2 Z}{\partial \theta^2} - \alpha_+^2 Z = 0\,. \tag{5.11}$$

Using separation of variables once more $Z(r,\theta) = R(r)\Theta(\theta)$ with the fact that $Z(r,\theta) = Z(r,\theta + 2\pi)$, we know $\Theta(\theta)$ will have the form

$$\Theta(\theta) = A\cos m\theta + B\sin m\theta, \tag{5.12}$$

where m is an integer and $m = 0, 1, 2, 3, ...$, then

$$\frac{\mathrm{d}^2 R}{\mathrm{d}r^2} + \frac{1}{r}\frac{\mathrm{d}R}{\mathrm{d}r} + \left(\alpha_-^2 - \frac{m^2}{r^2}\right) R = 0\,, \tag{5.13}$$

$$\frac{\mathrm{d}^2R}{\mathrm{d}r^2} + \frac{1}{r}\frac{\mathrm{d}R}{\mathrm{d}r} - \left(\alpha_+^2 + \frac{m^2}{r^2}\right) R = 0\,. \tag{5.14}$$

The first, Eq. (5.13), is a Bessel differential equation of order m, while Eq. (5.14) is a modified Bessel differential equation of order m. Given that the solution of $R(r)$ should be finite for all the points inside the diaphragm, it follows that terms of the Bessel functions of the second kind should be removed because they diverge to infinity at $r = 0$. The general solution of Eq. (5.6) can then be written as

$$Z(r,\theta) = [C_m J_m(\alpha_- r) + C'_m I_m(\alpha_+ r)] \times (A_m \cos m\theta + B_m \sin m\theta)\ , \tag{5.15}$$

where J_m is the Bessel function of the first kind of order m and I_m is the modified Bessel function of the first kind of order m. For a clamped diaphragm, the boundary conditions of $Z(r,\theta)$ can be written as

$$Z(a,\theta) = 0\,, \tag{5.16}$$

$$\frac{\partial Z}{\partial r}|_{r=a} = 0\,. \tag{5.17}$$

Using the general solution in Eq. (5.16), we obtain

$$C'_m = -\frac{J_m(\alpha_- a)}{I_m(\alpha_+ a)} C_m\,, \tag{5.18}$$

so $Z(r,\theta)$ can be re-written as

$$Z(r,\theta) = \left[J_m(\alpha_- r) - \frac{J_m(\alpha_- a)}{I_m(\alpha_+ a)} I_m(\alpha_+ r)\right] \times (A_m \cos m\theta + B_m \sin m\theta)\ . \tag{5.19}$$

We can re-express the second boundary condition with this new solution as

$$\left[\frac{\mathrm{d}}{\mathrm{d}r} J_m(\alpha_- r) - \frac{J_m(\alpha_- a)}{I_m(\alpha_+ a)} \frac{\mathrm{d}}{\mathrm{d}r} I_m(\alpha_+ r)\right]_{r=a} = 0\,. \tag{5.20}$$

From the properties of the Bessel and modified Bessel functions

$$\frac{\mathrm{d}}{\mathrm{d}r}J_m(\alpha_- r) = \alpha_- J_{m-1}(\alpha_- r) - \frac{m}{r}J_m(\alpha_- r)\,, \tag{5.21}$$

$$\frac{\mathrm{d}}{\mathrm{d}r}I_m(\alpha_+ r) = \alpha_+ I_{m-1}(\alpha_+ r) - \frac{m}{r}I_m(\alpha_+ r)\,, \tag{5.22}$$

we derive the equation that determines the fundamental resonant frequencies as

$$x_- I_m(x_+)J_{m-1}(x_-) - x_+ J_m(x_-)I_{m-1}(x_+) = 0 \tag{5.23}$$

where $x_\pm \equiv \alpha_\pm a$. It is difficult to find an analytic solution for the equation above. Furthermore, the in-plane tension usually isn't even known at this stage. However, as long as we can measure the first resonant frequency of the diaphragm experimentally, then $x_\pm$ can be solved numerically and the in-plane tension can subsequently be extracted. Plugging these parameters back into Eq. (5.23), frequencies of higher resonant modes can then be also solved numerically. Below, we will use the parameters of a thin circular graphene diaphragm mentioned earlier and assume that the first resonant frequency is measured to be at 5.5 MHz to demonstrate this idea.

Based on the definitions of $\alpha_\pm$ and $x_\pm$, we can express the relation between $x_\pm$ with λ and κ as

$$x_+ x_- = \lambda^2 a^2\,, \tag{5.24}$$

$$x_+^2 - x_-^2 = \kappa^2 a^2\,. \tag{5.25}$$

Inserting Eq. (5.24) into Eq. (5.23) we can write

$$\frac{\lambda^2 a^2}{x_+} I_m(x_+) J_{m-1}\left(\frac{\lambda^2 a^2}{x_+}\right) - x_+ J_m\left(\frac{\lambda^2 a^2}{x_+}\right) I_{m-1}(x_+) = 0\,. \tag{5.26}$$

Referring to the definition of λ in Eq. (5.8) we can calculate λ_{01} for the first resonant frequency $f_{01} = 5.5\,\mathrm{MHz}$ as

$$\lambda_{01}\, a = a\left(2\pi f_{01}\sqrt{\frac{\rho h}{D}}\right)^{1/2} \approx 5.419\,. \tag{5.27}$$

Plugging λ_{01} into Eq. (5.26), we can try to solve for x_{+01}. Although Eq. (5.26) has an infinite number of solutions, we can tell from the definition of $\alpha_\pm$ and $x_\pm$ that $x_+ \geq x_-$. Using the relation between $x_\pm$ and Eq. (5.24) we notice that $x_+ \geq \lambda a$. Finding the root of Eq. (5.26) with this condition, we can get $x_{+01} \approx 11.133$ and $x_{-01} \approx 2.638$. Using the relation between κ and $x_\pm$ we can calculate $\kappa = 3.387 \times 10^6\,\mathrm{m}^{-1}$ and therefore the in-plane tension $\Sigma = 3.9 \times 10^6\,\mathrm{MPa}$. With these parameters, we can numerically solve Eq. (5.23) for the resonant frequencies of higher modes, e.g. $\lambda_{11}a \approx 7.008$, $\lambda_{21}a \approx 8.225$, $\lambda_{02}\,a \approx 8.642$ and so on. The corresponding resonant frequencies are $f_{11} \approx 9.1\,\mathrm{MHz}$, $f_{21} \approx 12.7\,\mathrm{MHz}$, $f_{02} \approx 13.8\,\mathrm{MHz}$, etc. The ratio between the higher resonant frequencies to the first resonant frequency is then $f_{11}/f_{01} \approx 1.65$, $f_{21}/f_{01} \approx 2.30$, $f_{02}/f_{01} \approx 2.51$, etc.

For the convenience of the following discussion, it is usually common to normalize $Z(r,\theta)$ so that the maximum value of $|Z(r,\theta)|$ is unity. This is to ensure that the time term can represent the transverse motion of the diaphragm. As an example, the spatial term when $m = 0$ can be written as

$$Z_{01}(r,\theta) = A_{01}\left[J_0\left(\frac{x_{-01}r}{a}\right) - \frac{J_0(x_{-01})}{I_0(x_{+01})}I_0\left(\frac{x_{+01}r}{a}\right)\right]. \tag{5.28}$$

The maximum value of 1.00001 occurs when $r = 0$, which can be viewed as unity thus yielding a normalization of $A_{01} \approx 1\,\mathrm{m}^{-1}$.

The effective mass is another very useful concept that is utilized to analyze the transverse motion of the diaphragm. For a circular diaphragm, it can be defined as

$$\frac{M_{mn}}{M} = \frac{1}{\pi a^2} \int_0^{2\pi} d\theta \int_0^a r|Z_{mn}(r,\theta)|^2 dr \,, \tag{5.29}$$

where $M = \rho\pi a^2 h$ represents the total mass of the diaphragm and M_{mn} is the effective mass of mode mn. Let us again focus on the fundamental resonant mode that corresponds to the first resonant frequency f_{01} for the two cases of no bending rigidity and no tension. When $D = 0$, the spatial mode can be written as [18]

$$Z_{01}|_{D=0}(r,\theta) = A_{01}|_{D=0} J_0\left(\frac{\gamma_{01} r}{a}\right) , \tag{5.30}$$

where $A_{01}|_{D=0} = 1$. The corresponding ratio of the effective mass to the total mass is $(M_{01}/M)|_{D=0} \approx 0.2695$ [18]. Similarly, when $\Sigma = 0$ the spatial mode of the fundamental resonant mode is [22]

$$Z_{01}|_{\Sigma=0}(r,\theta) = A_{01}|_{\Sigma=0} \left[J_0\left(\frac{\beta_{01} r}{a}\right) - \frac{J_0(\beta_{01})}{I_0\beta_{01})} I_0\left(\frac{\beta_{01} r}{a}\right) \right] , \tag{5.31}$$

where $A_{01}|_{\Sigma=0} \approx 1.056$. The corresponding ratio of the effective mass to the total mass is $(M_{01}/M)|_{\Sigma=0} \approx 0.1829$. When both terms are necessary we should expect the ratio to again lie between the previous two special cases similar to the previous discussion on the resonant frequencies earlier in this section. In the case that the first resonant frequency is found to be $f_{01} = 5.5\,\text{MHz}$, we can numerically calculate $M_{01}/M \approx 0.226$ using $Z_{01}(r,\theta)$ from Eq. (5.28). The mode shape of a system can provide insight about its effective mass, as demonstrated in Figure 5.2. The figure shows the mode shape of the fundamental

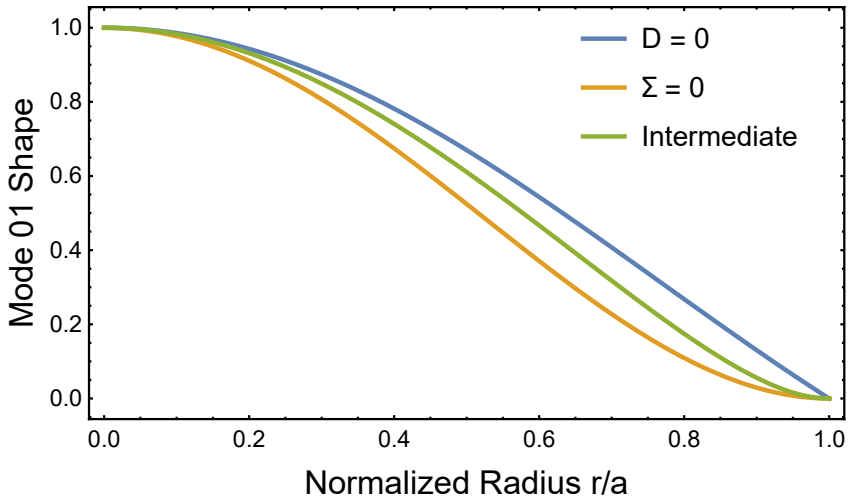

Figure 5.2: The mode shape of the fundamental resonant mode $Z_{01}(r)$ as a function of the normalized radius r/a.

resonant mode, Z_{01}, as a function of the normalized radius r/a. Integration of the mode shape from 0 to r/a reflects the value the effective mass. As the figure illustrates, when $D = 0$ the integration is at its maximum, resulting in the largest effective mass. Conversely, when $\Sigma = 0$ the integration is at its minimum, resulting in the smallest effective mass. When both terms are considered, the mode shape falls in between, resulting in an effective mass that is also in between the two extremes. As it will be shown in the Chapter 6, we can directly measure the effective mass experimentally by fitting to the PSD of the corresponding specific resonant mode. Therefore, the ratio between the effective mass and the total mass is required in order to calculate the total mass of the diaphragm.

It is worth noting that the method described above requires the knowledge of the physical and mechanical properties of the diaphragm in Eq. (5.27).

As a result, the method only works in cases of very "clean" samples. However, reality is not so kind, and the sample may be contaminated with water, oil, hydrocarbons, etc. The method to calculate the mode shape and effective mass in these situations will be discussed in Chapter 6.

5.2 Brownian motion of suspended diaphragms

Given the fundamental resonant modes of the diaphragm that were solved in the previous section, the out-of-plane motion of the diaphragm can be decomposed into a summation of the fundamental resonant modes

$$z(r,\theta,t) = \sum_{m,n} z_{mn}(t) Z_{mn}(r,\theta)\,. \tag{5.32}$$

Please note that we will keep using cylindrical coordinates for the discussion below to suit our experiment needs, but the result applies to other coordinates as well. Here Z_{mn} has been normalized so that the maximum value is unity as mentioned in the previous section. The fundamental modes can be shown to be orthogonal, which means

$$\iint Z_{mn}(r,\theta) Z_{jk}(r,\theta) dS = \epsilon_{mn,jk}\delta_{mn,jk}\,, \tag{5.33}$$

where the integral is evaluated over the surface of diaphragm and $\epsilon_{mn,jk}$ is a constant related to the normalization and $\delta_{mn,jk}$ is defined as

$$\delta_{mn,jk} = \begin{cases} 1, & mn = jk \\ 0, & mn \neq jk \end{cases}\,. \tag{5.34}$$

The thermal force term of Eq. (5.1) can also be decomposed into the fundamental resonant modes as

$$F_{th}(r,\theta,t) = \sum_{m,n} q_{mn}(t) Z_{mn}(r,\theta)\,. \tag{5.35}$$

Multiplying the equation above by Z_{jk} and integrating over the diaphragm, we can write

$$q_{mn}(t) = \chi_{mn}^{-2} \iint F_{th}(r,\theta,t) Z_{mn}(r,\theta) dS\,, \tag{5.36}$$

where $\chi_{mn}^2 = \iint Z_{mn}^2(r,\theta) dS$. Plugging Eq. (5.32) and Eq. (5.35) into Eq. (5.1), we have

$$\sum_{mn} \left[\ddot{z}_{mn}(t) + \frac{\mu}{\rho h} \dot{z}_{mn}(t) + \omega_{mn}^2 z_{mn}(t) - \frac{q_{mn}(t)}{\rho h} \right] Z_{mn}(r,\theta) = 0\,. \tag{5.37}$$

Since the equation above holds for any point on the diaphragm, then it follows that the expression in the bracket must be zero and we have

$$\ddot{z}_{mn}(t) + \frac{\mu}{\rho h} \dot{z}_{mn}(t) + \omega_{mn}^2 z_{mn}(t) = \frac{q_{mn}(t)}{\rho h}\,. \tag{5.38}$$

Using the definition of the effective mass $M_{mn} \equiv \rho h \iint Z_{mn}^2\, dS$ and linking the damping term to the Quality factor of the oscillation, then the equation above can be written as

$$\ddot{z}_{mn}(t) + \frac{\omega_{mn}}{Q_{mn}} \dot{z}_{mn}(t) + \omega_{mn}^2 z_{mn}(t) = \frac{F_{th,\,mn}(t)}{M_{mn}}\,, \tag{5.39}$$

where $F_{th,\,mn}(t) = \iint F_{th}(r,\theta,t) Z_{mn}(r,\theta)\, dS$. In order to apply the method we developed in Chapter 2 when studying the Brownian motion of a single particle to the Brownian motion of a suspended diaphragm, we just need to

prove that $F_{th,\,mn}(t)$ still describes a random stationary process.

If $F_{th}(\boldsymbol{x},t)$ describes a random stationary process with a zero-mean $\big\langle F_{th}(\boldsymbol{x},t)\big\rangle = 0$ and a δ-correlated property $C_{th}(\boldsymbol{x},t,\boldsymbol{x'},t') = \delta(t-t')C'_{th}(\boldsymbol{x},\boldsymbol{x'})$, then it can be seen that

$$\big\langle F_{th,mn}(\boldsymbol{x},t)\big\rangle = \iint \big\langle F_{th}(\boldsymbol{x},t)\big\rangle Z_{mn}\,dS = 0 \tag{5.40}$$

and

$$\begin{aligned} C_{F_{th,mn}(\boldsymbol{x},t)F_{th,mn}(\boldsymbol{x'},t')} &= \iiiint \big\langle F_{th}(\boldsymbol{x},t)F_{th}(\boldsymbol{x'},t')\big\rangle Z_{mn}(\boldsymbol{x})Z_{mn}(\boldsymbol{x'})\,dS \\ &= \iiiint C_{th}(\boldsymbol{x},t,\boldsymbol{x'},t')Z_{mn}(\boldsymbol{x})Z_{mn}(\boldsymbol{x'})\,dS \\ &= \delta(t-t')\iiiint C'_{th}(\boldsymbol{x},\boldsymbol{x'})Z_{mn}(\boldsymbol{x})Z_{mn}(\boldsymbol{x'})\,dS\,, \end{aligned} \tag{5.41}$$

which shows that $F_{th,\,mn}(t)$ still describes a random stationary process and the techniques developed in Chapter 2 can still be applied here. If we perform a Fourier transform to Eq. (5.39) we can write

$$\tilde{z}_{mn}(\omega) = \tilde{h}_{mn}(\omega)\tilde{F}_{th,\,mn}(\omega)\,, \tag{5.42}$$

where $\tilde{h}_{mn}(\omega)$ is defined as

$$\tilde{h}_{mn}(\omega) = \frac{1}{M_{mn}\left(\omega_{mn}^2 - \omega^2 + i\omega_{mn}\omega/Q_{mn}\right)}\,. \tag{5.43}$$

Using Eq.(2.26) we can also obtain

$$S_{zz,mn}(\omega) = |\tilde{h}_{mn}(\omega)|^2 S_{th,mn}(\omega) \tag{5.44}$$

$$= \frac{1}{M_{mn}^2\left[(\omega^2-\omega_{mn}^2)^2 + \omega_{mn}^2\omega^2/Q_{mn}^2\right]} S_{th,mn}(\omega)\,. \tag{5.45}$$

Since the auto-correlation function $F_{th,\,mn}(t)$ is a δ-function with a strength ϵ_{mn}^2, the corresponding PSD is simply

$$S_{th,mn}(\omega) = \epsilon_{mn}^2 \,. \tag{5.46}$$

Therefore, the PSD of the $z_{mn}(t)$ after substitution is

$$S_{zz,mn}(\omega) = \frac{\epsilon_{mn}^2}{M_{mn}^2\,[(\omega^2 - \omega_{mn}^2)^2 + \omega_{mn}^2\omega^2/Q_{mn}^2]} \,. \tag{5.47}$$

We can use Eq. (2.32) which provides a way to calculate the variance of a signal from the PSD to express the variance of the position signal as

$$\sigma_{z,mn}^2 = \frac{1}{2\pi}\int_{-\infty}^{\infty} S_{zz,mn}(\omega)\,d\omega = \frac{\epsilon_{mn}^2}{2M_{mn}^2\omega_{mn}^2/Q_{mn}} \,. \tag{5.48}$$

Using the equipartition theorem that states [18]

$$\frac{1}{2}M_{mn}\omega_{mn}^2\sigma_{z,mn}^2 = \frac{1}{2}k_BT \,, \tag{5.49}$$

we can get the relation $\epsilon_{mn}^2 = 2k_BT\omega_{mn}M_{mn}/Q_{mn}$ and then express the one-sided position PSD as

$$S_{zz,mn}(\omega) = \frac{4k_BT\omega_{mn}}{M_{mn}Q_{mn}\,[(\omega^2 - \omega_{mn}^2)^2 + \omega_{mn}^2\omega^2/Q_{mn}^2]} \,. \tag{5.50}$$

If we write $u(t) = \dot{z}(t)$ and use Eq. (2.27), then the one-sided velocity PSD $S_{uu,mn}(\omega)$ can also be obtained as

$$S_{uu,mn}(\omega) = \frac{4k_BT\omega_{mn}\,\omega^2}{M_{mn}Q_{mn}\,[(\omega^2 - \omega_{mn}^2)^2 + \omega_{mn}^2\omega^2/Q_{mn}^2]} \,. \tag{5.51}$$

Furthermore, it is more convenient to express the position PSD in terms of the natural frequency as

$$S_{zz,mn}(f) = \frac{k_BTf_{mn}}{2\pi^3M_{mn}Q_{mn}\,[(f^2 - f_{mn}^2)^2 + f_{mn}^2f^2/Q_{mn}^2]} \tag{5.52}$$

and the velocity PSD as

$$S_{uu,mn}(f) = \frac{2k_B T f_{mn} f^2}{\pi M_{mn} Q_{mn} \left[(f^2 - f_{mn}^2)^2 + f_{mn}^2 f^2 / Q_{mn}^2\right]} . \tag{5.53}$$

Using the Wiener-Khinchin theorem, we can get the auto-correlation function by performing a reverse Fourier transform of the PSD to obtain

$$C_{zz,mn} = \frac{k_B T}{\kappa} \left(\cos \omega_{1mn} t + \frac{\sin \omega_{1mn} t}{2\omega_{1mn} \tau_{p,mn}} \right) e^{-t/2\tau_{p,mn}} , \tag{5.54}$$

$$C_{uu,mn} = \frac{k_B T}{m} \left(\cos \omega_{1mn} t - \frac{\sin \omega_{1mn} t}{2\omega_{1mn} \tau_{p,mn}} \right) e^{-t/2\tau_{p,mn}} , \tag{5.55}$$

where $\omega_{1mn} = \omega_{mn} \sqrt{1 - (2Q_{mn})^{-2}}$ and $\tau_{p,mn} = Q_{mn}/\omega_{mn}$. The corresponding MSD of mode mn is

$$\mathrm{MSD}_{mn}(t) = \frac{2k_B T}{\kappa} \left[1 - e^{-t/2\tau_{p,mn}} \left(\cos \omega_{1mn} t + \frac{\sin \omega_{1mn} t}{2\omega_{1mn} \tau_{p,mn}} \right) \right] . \tag{5.56}$$

The theory to study the Brownian motion of diaphragms was established in this Chapter. In next chapter we will transition to the experiment setup and results of measuring the Brownian motion of the diaphragm.

Chapter 6

Measuring the Brownian Motion of Graphene Diaphragms

In this chapter we will discuss both the experiment and results from measuring the Brownian motion of suspended graphene diaphragms. In Section 6.1 we will cover the experimental details, including the choice of the diaphragms to study and the experimental tools used to measure the Brownian motion of the diaphragms, as well as the setup and procedure of the experiment. The results and analysis are subsequently presented in Section 6.2. We will use the spectral method in Section 6.2.1 to measure the effective mass of the diaphragm that corresponds to the first fundamental resonant mode. Afterward, we introduce a new methodology in Section 6.2.2 to determine the mode shape that uses the first resonant frequencies. By combining the effective mass and the corresponding mode shape, the total mass of the suspended graphene diaphragm can be calculated.

6.1 Experiment

6.1.1 Suspended graphene diaphragm

The sample chosen for this experiment is 6-8 layers of graphene on Ultra-fine 2000 Mesh Copper TEM Grids (Ted Pella 21970-5). The thickness

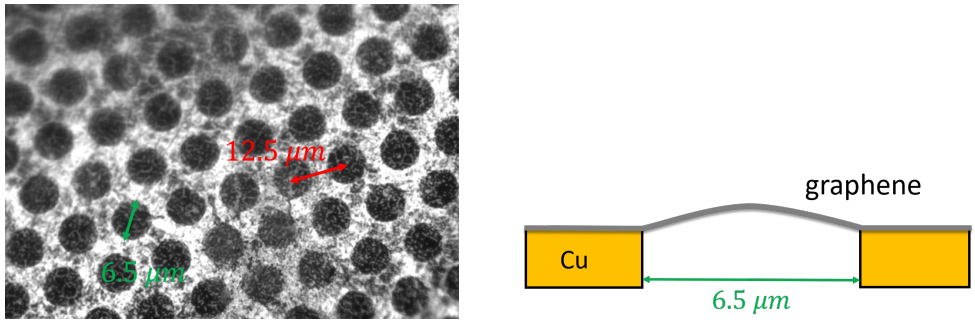

Figure 6.1: (left) Top view of the suspended graphene sample. Optical image taken with the CCD camera from a laser Doppler vibrometer setup (MSA-600-U). (right) Schematic of the suspended graphene diaphragm in cross section view. The graphene diaphragm is represented by the solid grey line, the curvature of which represents the thermal motion of the diaphragm over the through hole on the copper plate.

of the graphene is between 2.1 - 2.8 nm and the Young's modulus is 0.9 TPa according to the manufacturer. The graphene is grown by the chemical vapor deposition (CVD) on copper substrate. The copper substrate is etched away and the remaining graphene is transferred to a separate meshed copper grid by the wet transfer process. Across the copper grid are circular through holes with a diameter of 6.5 µm and a pitch between the adjacent holes of 12.5 µm, as shown in Figure 6.1 (left). The graphene sheet covers the entire copper grid and leaves freestanding graphene over the through holes, as illustrated in Figure 6.1 (right). The copper grid is supported by a 3 mm circular holder with a 1 x 2 mm slot in the middle (Ted Pella, 4510 PELCO SynapTek grids) where the copper and graphene are exposed. These exposed sections of graphene on both sides of the sample can be sued to design a fiber acoustic detector with an optical readout, the design of which is covered in Chapter 7.

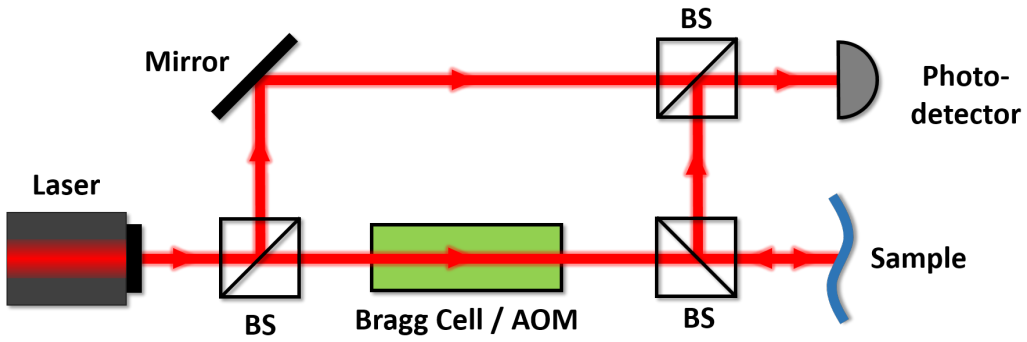

Figure 6.2: The schematic of a typical heterodyne design of LDV.

6.1.2 Laser Doppler vibrometry

In order to measure the mass of the suspended diaphragms using their Brownian motion, the position or displacement of the diaphragm need to be directly measured. In our experiment, a laser Doppler vibrometer (LDV) is used for detection of the Brownian motion of the diaphragm. We first introduce and review the operating principle of the LDV before providing the technical details of the specific LDV machine used in the experiment.

The LDV is a non-contact optical device that uses laser light to precisely measure the vibration velocity and displacement of a surface. Figure 6.2 shows a simplified schematic of a typical heterodyne design of a LDV. The laser beam is first split into two parts by a non-polarizing beam-splitter. The upper beam serves as a reference beam. The lower beam, which we call detection beam, passes through either a Bragg cell or an AOM that adds a frequency shift f_s, usually in the range of tens of MHz, to the original frequency of the laser beam. The detection beam with shifted frequency is then directed at the

vibrating sample. Laser light reflected from the sample is then re-combined with the reference beam and is collected and detected by a photodiode to produce a beat note signal..

The phase shift $\phi(t)$ of the detection laser beam due to the displacement $s(t)$ of the sample is [66]

$$\phi(t) = \frac{4\pi s(t)}{\lambda}, \tag{6.1}$$

where λ is the wavelength of the laser. Then the frequency modulation due to the phase shift can be written as

$$f_D = \frac{\omega(t)}{2\pi} = \frac{1}{2\pi}\frac{\mathrm{d}\phi(t)}{\mathrm{d}t} = \frac{2v(t)}{\lambda}, \tag{6.2}$$

where $v(t)$ is the velocity of the sample and f_D is the Doppler shift frequency. The photo-detector will detect a beat note signal between the reference beam and the reflected detection beam, where the Doppler shift frequency f_D is encoded. After obtaining the beat note signal, either the analog decoder using a phase-locked loop circuit or a digital decoder using the arctangent phase method can be used to extract the phase shift $\phi(t)$ and therefore the displacement of the sample $s(t)$ [66].

The LDV used in our experiment is a MSA-600-U from Polytec (with MSA-A-DIF option, non-differential measurement mode). It can measure the out-of-plane vibrations with frequencies between 6.25 Hz and 600 MHz. The maximum sampling time is 160 ms. The displacement resolution is $100\,\mathrm{fm}/\sqrt{\mathrm{Hz}}$ for frequencies up to 1 MHz and $15\,\mathrm{fm}/\sqrt{\mathrm{Hz}}$ for frequencies between 1 MHz and 600 MHz. The optical system for detection consists of a 532

nm laser with a maximum power of 5 mW and can be focused down to a spot with diameter as low as 0.8 um with the bright field objective. It also has a high resolution digital camera installed for a full-field view of the sample.

6.1.3 Experiment setup

In this section, we will detail the experimental setup and the process for preparing the sample for measurement. First, the graphene sample is secured to the center of the top side of a cylindrical sample holder, which has a diameter of 0.75 inches and a thickness of 0.345 inches, using a tiny amount of silver paint applied on the edges of the sample. The sample holder is designed with a hole, measuring 0.078 inches in diameter and 0.062 inches in depth at the center of the top side, that allows the suspended graphene to move freely in the out-of-plane direction. Additionally, a threaded hole for a 1/4-20 screw is placed at the center of the bottom side of the sample holder, allowing for secure placement in the chamber. The sample holder also features a side hole with a diameter of 0.062 inches and a trench with a width of 0.062 inches and a height of 0.025 inches, both of which are designed to minimize trapped gas within the sample holder. The design of the sample holder is shown in Figure 6.3.

After the silver paint used to secure the position of the sample has dried, the sample, together with the sample holder, is inserted into a cleaning chamber that uses radiation heating from a lamp to heat the sample to temperatures above 300 °C as shown in Figure 6.4. The sample is left in the

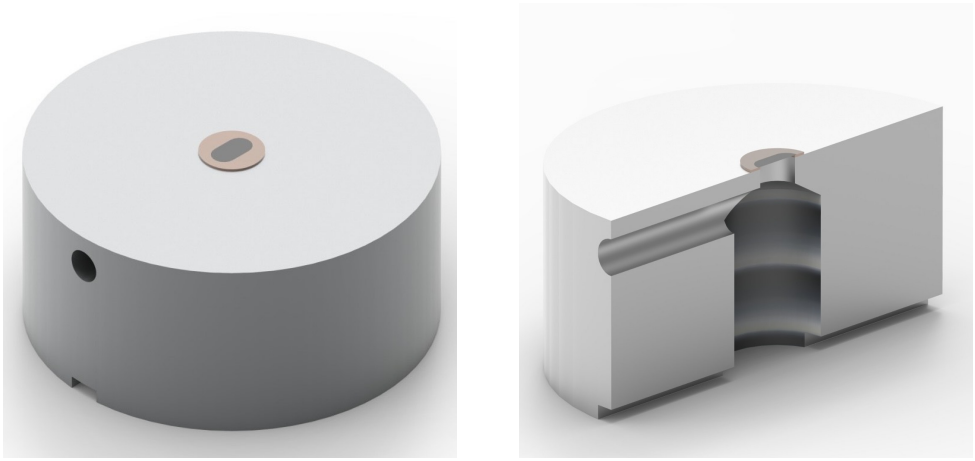

Figure 6.3: (left) Graphene sample fixed on the sample holder. (right) The cross-sectional view of the sample holder.

chamber overnight to thoroughly remove contaminants such as hydrocarbons.

Immediately after removal from the cleaning chamber, the graphene sample holder is mounted into a custom chamber, specifically designed for our measurements. The chamber, as shown in Figure 6.5, is comprised of a 2.75-inch tapped ConFlat (CF) vacuum blank flange that functions as the base. The blank flange is machined to have a centrally located threaded hole that secures sample holder in place inside the chamber. Additionally, two pairs 0.25-inch diameter blind holes are drilled on the sides of the flange, which serve as the connection points for welding two 1/4-inch stainless steel tubes, used for pumping and controlled gas leaking. Furthermore, two additional holes with a diameter of 0.25 inches are drilled on interior side of the flange to form an L-channel that to connects the inside of the chamber to the pumping tubes. Valves are attached to each of these two tubes (not shown in the Figure)

Figure 6.4: The graphene diaphragm in the cleaning chamber. The sample is heated up and cleaned by the radiation heat from the lamp.

to seal the chamber after pumping down vacuum and prevent any vibrations caused by the pump from interfering with the accuracy of the measurements. The chamber also includes a 2.75-inch double-sided CF flange to function as a separating middle layer to create some vertical space for the sample, and a 2.75-inch DUV-graded fused silica viewport (Kurt J. Lesker VPZL-275DUC2) with anti-reflection coating from 425-760 nm as the top layer. Crucially, the viewport coating has near zero reflectivity at 532 nm, which is the wavelength of laser used in the LDV. This minimizes the reflected beam power from the viewport, which is essential for the experiment. Once the chamber is sealed and connected to an oil-free pumping system, the pressure inside the chamber

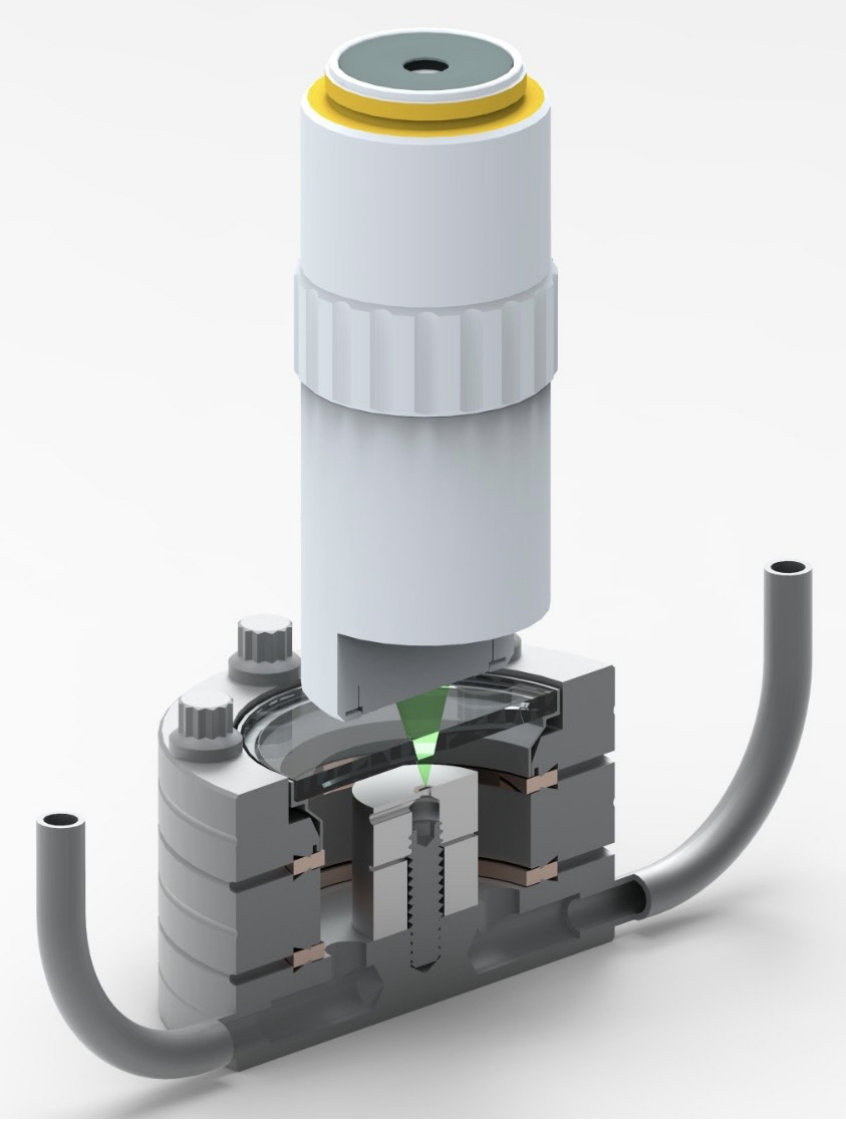

Figure 6.5: The experimental setup of measuring the Brownian motion of the graphene diaphragm. The chamber is shown with a cross-sectional view for clarity. Two valves connected to the two 1/4-inch tubes in the figures are not shown.

is pumped down to a lower pressure[1], reducing the possibility of further contamination. Subsequently, the valves on the two tubes are closed to isolate the system. The chamber is then disconnected from the pumping system and is transferred for measurement to the LDV as shown in Figure 6.5. The detection beam from the LDV is focused on the sample via a 50X microscope objective (A-MOB-050X) and the spot diameter at the focus should be 1.4 µm according to the manufacturer. This concludes the experimental setup for measuring the Brownian motion of the suspended graphene diaphragm and the results of the measurement are covered in the next section.

6.2 Results

6.2.1 Effective mass

The laser Doppler vibrometer used in the measurement allows us to acquire the displacement signal directly instead of extracting the calibration factor by fitting to the voltage PSD as described in Chapter 4. However, as we can see from Eq. (5.52), in the frequency regime where $f \ll f_{01}$ where f_{01} is the first resonant frequency of the diaphragm, the corresponding position PSD is inversely proportional to f_{01}^4. As shown below, our choice of graphene sample results in a first resonant frequency in the MHz region which is beneficial for building a low-thermal-noise and high-bandwidth acoustic sensor. However, at this frequency other noises in the system becomes non-negligible and an

[1]The pressure measured close to the pump is 10^{-4} mbar; however, the pressure in the chamber should be larger due to small conductance of the thin tube used to connect the chamber to the pump.

additional corresponding term needs to be included in Eq. (5.52) for fitting as

$$S_{zz,\mathrm{tot}}(f) = \frac{k_B T f_{mn}}{2\pi^3 M_{mn} Q_{mn} \left[(f^2 - f_{mn}^2)^2 + f_{mn}^2 f^2 / Q_{mn}^2\right]} + S_{zz,\mathrm{noise}}\,, \tag{6.3}$$

where $S_{zz,\mathrm{noise}}$ refers to the constant noise floor in the frequency domain. During the experiment, one trial of data over 160 ms is collected at a sampling rate of 125 MHz. Similar to the spectral method described in Chapter 4, the Bartlett method [50] is used by dividing the signal into smaller segments and averaging PSD of each segment in order to reduce the noise in the PSD.

In principle, the diaphragm has an infinite number of resonant modes, but only three or four resonant frequencies can be resolved with the laser beam focused on the center of the diaphragm in our experiment. The first resonant peak is dominant and is used for fitting to extract parameters. Similar to the fitting method in Chapter 4, we temporarily ignore the experimental parameters and only focus on fitting the PSD itself. So it is more convenient to write Eq. (6.3) as

$$S_{zz,\mathrm{tot}}(f;\boldsymbol{\theta}) = \frac{a}{(f^2 - f_0^2)^2 + b^2 f^2} + c\,, \tag{6.4}$$

where $\boldsymbol{\theta} \equiv (a, f_0, b, c)^\top$ and $a,\ f_0,\ b,\ c$ are the fitting parameters referred to below. An actual example of an experimental PSD of the first resonant peak and the best-fit curve are shown in Figure 6.6.

The uncertainty in the fitting parameters can be extracted by taking the square root of diagonal terms in the the variance-covariance matrix $\boldsymbol{\Sigma}_{\boldsymbol{\theta}}$. We find the relative uncertainties of the fitting parameters as $\sigma_a/a = 0.61\,\%$, $\sigma_{f_0}/f_0 = 0.006\,\%$, $\sigma_b/b = 0.38\%$ and $\sigma_c/c = 0.22\,\%$ when fitting the first

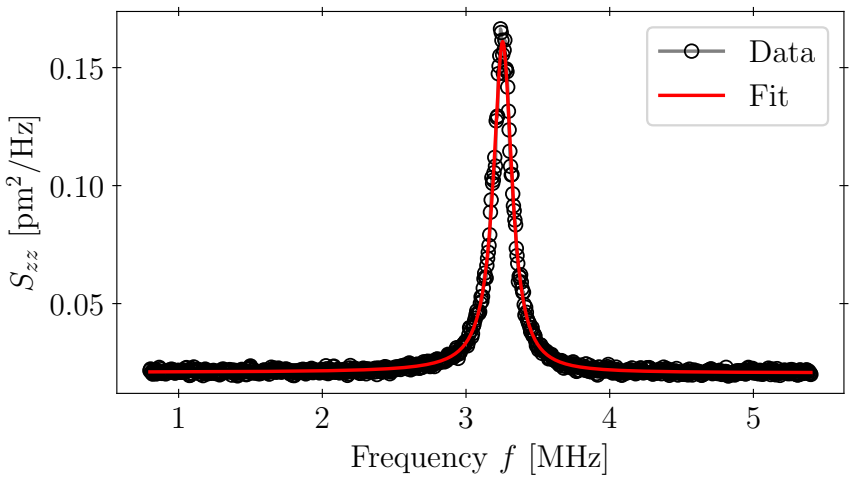

Figure 6.6: The position PSD for the first resonant mode of a 6-8 layer graphene diaphragm at low pressures. The experimental data is depicted as open black circles and the solid red line is the fitting result. The frequency range shown in the plot is the same one used for fitting.

resonant peak. The temperature of the environment, found to be 295.75 K, is also monitored during the experiment by placing a thermometer near the focus of the laser beam. What differs from the experiment weighing the optically trapped microsphere is that a power scan measurement is not needed, thus the experiment can be completed in much less time. As a result, the uncertainty of the temperature measurement is chosen to be the systematic uncertainty of the thermometer, which is 0.5 K, resulting in a relative uncertainty of the temperature as $\sigma_T/T = 0.17\,\%$.

Comparing Eq. (6.3) and Eq. (6.4) we can get the relation between the fitting parameters and the parameters to extract as

$$M_{mn} = \frac{k_B T b}{2\pi^3 a}\,, \tag{6.5}$$

$$f_{mn} = f_0\,, \quad Q_{mn} = f_0/b\,, \quad S_{zz,\mathrm{noise}} = c\,. \tag{6.6}$$

The uncertainties of f_{mn} and $S_{zz,\mathrm{noise}}$ are just the uncertainties of the fitting parameters f_0 and c, respectively. We find the first resonant frequency to be $f_{01} = 3.257\,\mathrm{MHz}$ with a relative uncertainty of 0.005 % while the noise floor is determined to be $S_{zz,\mathrm{shot}} = 0.02\,\mathrm{pm}^2/\mathrm{Hz}$. The uncertainties of the effective mass M_{mn} and quality factor Q_{mn} can both be calculated through the propagation of uncertainty as

$$\frac{\sigma_{M_{mn}}}{M_{mn}} = \sqrt{\left(\frac{\sigma_a}{a}\right)^2 + \left(\frac{\sigma_b}{b}\right)^2 + \left(\frac{\sigma_T}{T}\right)^2}, \tag{6.7}$$

$$\frac{\sigma_{Q_{mn}}}{Q_{mn}} = \sqrt{\left(\frac{\sigma_b}{b}\right)^2 + \left(\frac{\sigma_{f_0}}{f_0}\right)^2}. \tag{6.8}$$

Based on the fitting parameters extracted by fitting to the PSD of the first resonant peak and the temperature, we calculate that the effective mass of the first resonant mode is $M_{01} = 284.8\,\mathrm{fg}$ with a relative uncertainty of 0.74 % and the corresponding quality factor is 21.1 with a relative uncertainty of 0.38 %.

Fitting to PSD is essentially analogous to the spectral method described in Chapter 4. Is there a corresponding equipartition method? The situation turns out to be a little bit different here. According to Eq. (2.32), the variance of the position data equals the integral of the position PSD inside the bandwidth. Unfortunately, the shot noise overpowers the Brownian motion signal outside of the frequency window centered around the resonant peak. A bandpass filter is applied to increase the signal-to-noise ratio (SNR), as shown in Figure 6.7. However, this bandpass filter also removes some Brownian motion signal at the same time. A trade-off has to be made between maximizing

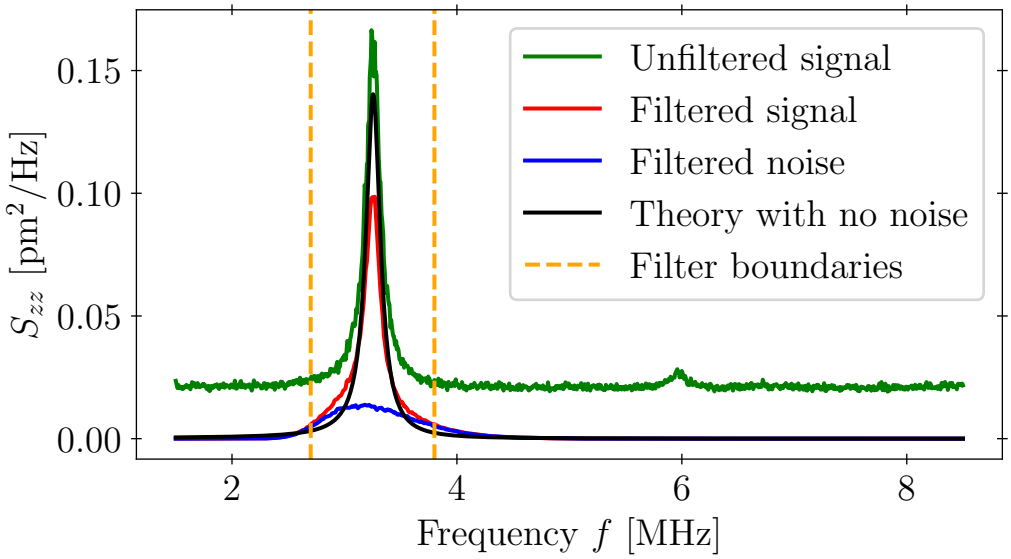

Figure 6.7: The position power spectral density of the original and bandpass filtered signal. The solid green and red lines represent the unfiltered and filtered signal, respectively. The dashed orange lines represent the boundaries of the bandpass filter. The noise is numerically generated from the fitting parameter c and is then bandpass filtered with the same boundaries. The solid black line represents the theoretical position PSD without noise.

the SNR while preserving as much Brownian motion signal as possible. A window spanning from 2.7 MHz to 3.8 MHz is chosen and the normalized distribution of the position signal is shown in Figure 6.8. The SNR is 2.42 and 54.5 % of the energy of the position due to short-time Brownian motion is resolved. Similarly, the normalized distribution of the velocity signal with the same bandpass filtering is shown in Figure 6.9. The SNR of the velocity signal is 2.34 and 54.1 % of the energy due to instantaneous velocity is resolved. The equipartition method could be used to measure the effective mass in the case when the signal due to the Brownian motion is larger than the shot noise

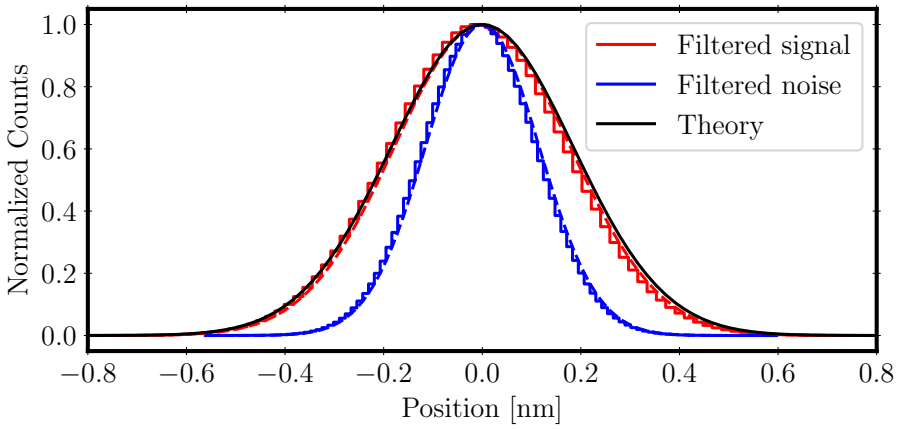

Figure 6.8: The normalized position distribution of the bandpass filtered signal (red) and noise (blue). The solid black line is the theoretical result using the effective mass and resonant frequency extracted by the spectral method.

floor in the low frequency region. This can possibly be achieved by using a suspended graphene diaphragm with a larger diameter and a lower first resonant frequency which leads to a higher Brownian motion signal in the low frequency region according to Eq (5.52). Recently, there has been progress to make large suspended monolayer and bilayer graphene diaphragms with diameters up to 750 µm [65]. It is worth testing the weighing method based on the equipartition theorem on those samples in the future experiments.

6.2.2 Mode shape and total mass

It is worth noting that what we measure by fitting to the PSD is the effective mass of the corresponding resonant mode, not the total mass of the suspended graphene diaphragm. According to Eq. (5.29), the total mass is equal to the effective mass corresponding to the first resonant mode divided

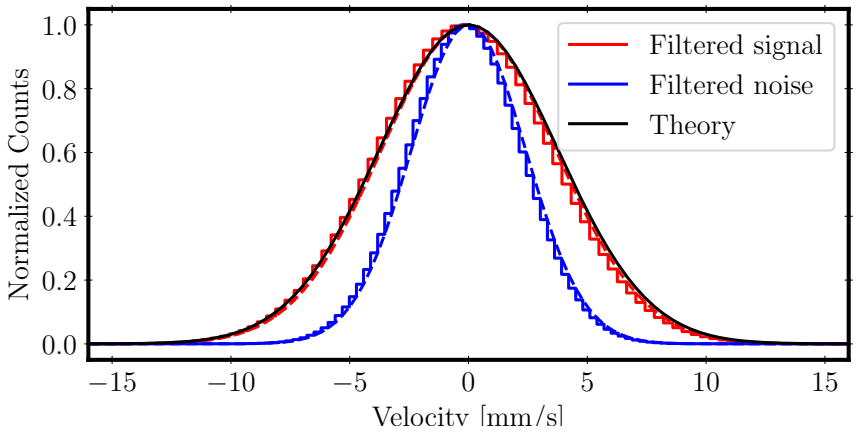

Figure 6.9: The normalized velocity distribution of the bandpass filtered signal (red) and noise (blue). The solid black line is the theoretical result using the effective mass extracted by the spectral method.

by a ratio ranging from 0.1829 to 0.2695 depending on the mode shape. This means the total mass of the suspended graphene diaphragm can range from 1056.8 fg to 1557.1 fg, which is much larger than the expected mass calculated from the manufacturer's data. This discrepancy implies there is contamination on the sample[2]. The method covered in Chapter 5 requires the knowledge of the thickness, density and mechanical properties of the graphene. However, when contamination is present on the sample, these parameters from the manufacturer are no longer accurate.

Here we propose a method that uses the frequencies of the higher resonant modes to extract the ratio of the effective mass to the total mass. The only other required knowledge of the sample is the radius of the suspended

[2]The contamination effect is larger for graphene in an ambient environment, which will be shown in Chapter 7.

graphene diaphragm which can be measured very accurately in our case.

Continuing from Eq. (5.23) in Chapter 5, if we define

$$k \equiv \kappa a = a\sqrt{\frac{\Sigma h}{D}}, \quad g \equiv 2\pi a\sqrt{\frac{\rho h}{D}}, \tag{6.9}$$

then we have

$$x_{\pm mn} = \sqrt{\frac{\sqrt{k^4 + 4f_{mn}^2 a^2 g^2} \pm k^2}{2}} \tag{6.10}$$

as the solutions of Eq. (5.23). Since higher resonant frequencies can be observed in the experiment, we can combine one of them with the first resonant mode and numerically solve Eq. (5.23) with the two corresponding resonant frequencies to extract k and g. After parameters k and g are calculated, they can be plugged back into Eq. (6.10) with the first resonant frequency to calculate $x_{\pm 01}$. Then the spatial mode of the fundamental mode Eq. (5.28) can be written in terms of $x_{\pm 01}$ allowing the ratio of the effective mass and the total mass M_{01}/M to be calculated. In practice, the first and second resonant frequencies are used. Not only because they are the strongest features present in our data but also it is more straight forward to find the corresponding mode numbers. Below, we will use our data set to illustrate the idea.

As mentioned above, the first measured resonant peak has a frequency of 3.257 MHz which is extracted by fitting to the PSD. The same method can again be used to extract the second resonant frequency, which was found to be 5.972 MHz with a 0.05 % relative uncertainty[3]. A careful scan has been

[3]The other fitting parameters a and b have a much larger fitting uncertainties, which are 9.49 % and 5.58 %, respectively. This is due to the small signal strength at higher frequencies.

made to ensure there are no other resonant peaks between these two strong peaks. From Table 5.1 we can see that the ratio between the second resonant frequency, which is f_{11}, to the first resonant mode should be 1.593 if only surface tension is considered and 2.082 if only bending rigidity is considered. The ratio between the measured second and first resonant peak in our experiment is 1.834 and falls between these two extreme cases, as shown in Figure 6.10. This implies that we are still in the intermediate regime where both terms need to be considered. Therefore, there is no analytic ratio between the effective mass to the total mass that can be used to get the total mass of the sample with effective mass calculated from the fitting parameters. However, we can solve the problem numerically with the method mentioned above.

Since we have measured the first and second resonant frequencies, which are f_{01} and f_{11}, respectively, we can plug them into Eq. (6.10) and express the following four parameters as

$$x_{\pm 01}(k,g) = \sqrt{\frac{\sqrt{k^4 + 4f_{01}^2 a^2 g^2} \pm k^2}{2}}, \tag{6.11}$$

$$x_{\pm 11}(k,g) = \sqrt{\frac{\sqrt{k^4 + 4f_{11}^2 a^2 g^2} \pm k^2}{2}}. \tag{6.12}$$

Plugging them into Eq. (5.23), we can write two equations with two unknown variables k and g as

$$x_{01} I_0(x_{+01}) J_{-1}(x_{-01}) - x_{+01} J_0(x_{-01}) I_{-1}(x_{+01}) = 0, \tag{6.13}$$

$$x_{11} I_1(x_{+11}) J_0(x_{-11}) - x_{+11} J_1(x_{-11}) I_0(x_{+11}) = 0. \tag{6.14}$$

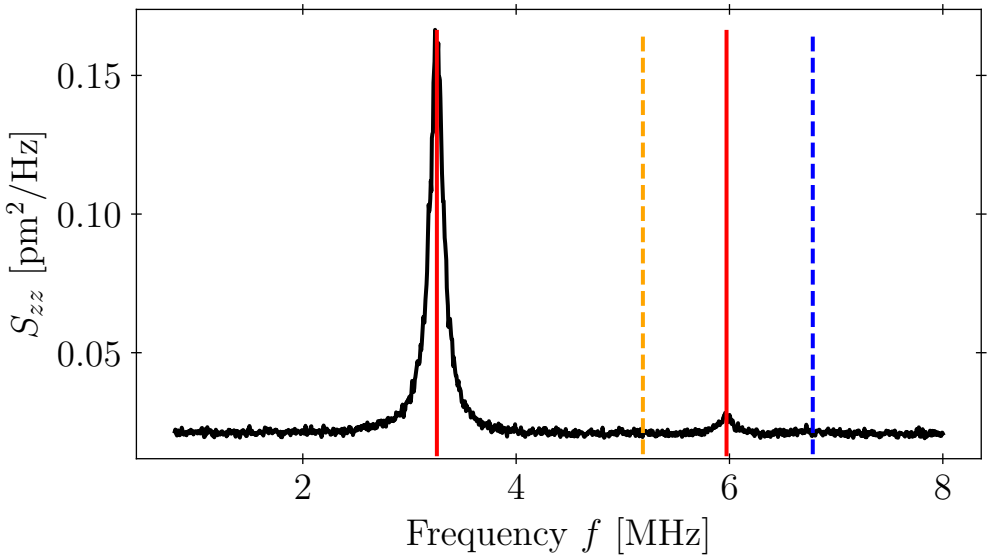

Figure 6.10: The position PSD for the graphene diaphragm. The experimental data is depicted as the solid black line and the solid red lines highlight the first two resonant frequencies extracted by fitting to the PSD at different regions. The dashed orange line is calculated by multiplying the measured first resonant frequency with the theoretical ratio f_{11}/f_{01} when only surface tension is included, which is 1.593 from Table 5.1. The dashed blue line is calculated by multiplying the measured first resonant frequency with the theoretical ratio when only bending rigidity is included, which is 2.082 from Table. 5.1.

Numerically solving these two equations together we find that $k = 4.036$ and $g = 1.386$. So $x_{\pm 01}$ can be calculated as $x_{-01} = 2.938$ and $x_{+01} = 4.992$. The fundamental spatial mode can then be written according to Eq. (5.28)

$$Z_{01}(r,\theta) = A_{01}\left[J_0\left(\frac{2.938r}{a}\right) - \frac{J_0(2.938)}{I_0(4.992)}I_0\left(\frac{4.992r}{a}\right)\right], \tag{6.15}$$

where the normalization factor $A_{01} \approx 0.9913$. According to the definition of effective mass in Eq. (5.29), we find that $M_{01}/M \approx 0.196$. So the total mass of the suspended graphene is determined to be 1453.1 fg. We see that by using the first two resonant frequencies, we are able determine the mode shape and calculate the total mass of the diaphragm rather than just bounding it's value.

It is worth noting that this measured mass corresponds to a mass density ρh of $4.4\times10^{-5}\,\mathrm{kg\,m^{-2}}$. The theoretical mass density of 6-8 layer graphene is from $4.8\times10^{-6}\,\mathrm{kg\,m^{-2}}$ to $6.3\times10^{-6}\,\mathrm{kg\,m^{-2}}$. The deviation that indicates the ratio between the measured and the theoretical mass density is from 7.0 to 9.2. It has also been shown by other experiment performed with CVD graphene in high vacuum ($1\times10^{-6}\,\mathrm{mbar}$) a deviation from 2.9 to 29 [67–69].

Further information can be extracted from solving for k and g other than just the mode shape. Based on the definition of k and g, Eq. (6.9), we have

$$\frac{k}{g} = \frac{1}{2\pi}\sqrt{\frac{\Sigma}{\rho}}, \tag{6.16}$$

$$\frac{1}{g} = \frac{1}{2\pi a}\sqrt{\frac{D}{\rho h}}. \tag{6.17}$$

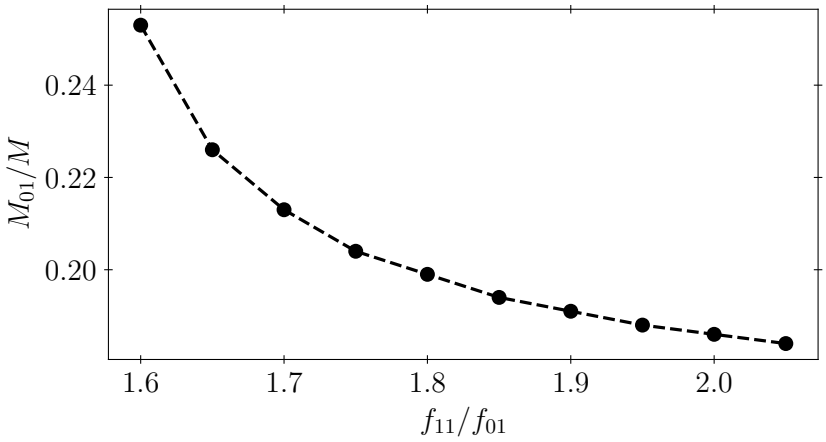

Figure 6.11: The ratio between the effective mass to the total mass M_{01}/M vs. the ratio of the first two resonant frequencies f_{11}/f_{01} for a suspended circular diaphragm with a radius of a, the measured first resonant frequency f_{01} and $f_{01}\,a = 9\,\mathrm{m/s}$.

Comparing with Eq. (5.3) and Eq. (5.4), we find that

$$f_{mn}|_{D=0} = \frac{k}{g}\frac{\gamma_{mn}}{a}\,, \tag{6.18}$$

$$f_{mn}|_{\Sigma=0} = \frac{1}{g}\frac{\beta_{mn}^2}{a}\,. \tag{6.19}$$

Therefore, we can estimate the contribution of the bending rigidity and surface tension to the final resonant frequency with k and g, for example $f_{01}|_{D=0} \approx 2.2\,\mathrm{MHz}$ and $f_{01}|_{\Sigma=0} \approx 2.3\,\mathrm{MHz}$, which are comparable to each other.

In the above we use our experimental data to illustrate the procedure of using the first two measured resonant frequencies to extract the mode shape of the suspended diaphragm, but the method is not limited to the specific parameters seen in our experiment. Figure 6.11 presents the numerical results of

the ratio between the effective mass to the total mass M_{01}/M vs. the ratio of the first two resonant frequencies f_{11}/f_{01} for a suspended circular diaphragm with a radius of a, the measured first resonant frequency f_{01} and $f_{01}\,a = 9\,\mathrm{m/s}$. It is also worth noting that the set of Eq. (6.13) and Eq. (6.14) have solutions only when the f_{11}/f_{01} is in between the two boundary values 1.593 and 2.082, which correspond to the case when only the surface tension or the bending rigidity is considered.

To summarize, the experimental setup and results of measuring the Brownian motion of a suspended graphene diaphragm have been covered in this chapter. Using laser Doppler vibrometry, the displacement of the graphene diaphragm can be directly read out so that the thermomechanical calibration is turned into a method to directly measure the effective mass of the diaphragm. Moreover, we have demonstrated a methodology that uses the first two resonant frequencies of the diaphragm to numerically solve the resonant mode shape allowing determination of the total mass. This method has the benefit that it doesn't require knowledge of the physical and mechanical properties of the diaphragm except for the radius which can be measured very accurately and it is not susceptible to contamination, making it possible to analyze the Brownian motion of the diaphragm in an ambient environment.

Chapter 7

Towards a Quantum-Limited Acoustic Detector

In this Chapter we outline the ongoing efforts to develop a quantum-limited acoustic detector in our group. After calibrating our system using the method described in Chapter 4, we can use the optically trapped microsphere as a high-bandwidth acoustic detector as detailed in Reference [10]. However, the bandwidth of the acoustic detector is limited by the shot noise at high frequencies. In Section 7.1 we discuss the design of a high-power balanced photodetector which can be utilized in future experiments to improve the bandwidth of the optically trapped microsphere as an acoustic detector. In order to develop a quantum-limited acoustic detector, it is crucial to study the properties of the suspended graphene diaphragm when exposed to an ambient environment, which is covered in Section 7.2. Finally, Section 7.3 provides a summary of the dissertation and presents a design for a portable, high-bandwidth acoustic detector based on a heterodyne fiber interferometer with a suspended graphene diaphragm.

7.1 High-power balanced photodetector

At high frequencies laser shot noise is a significant factor limiting the sensitivity of detection. Shot noise is a fundamental noise source that arises from the random nature of the photon emission process in a laser. The noise is characterized by a distribution of photon counts around the mean count with the standard deviation of the distribution being proportional to the square root of the mean count. Since the signal is proportional to the mean photon count, the SNR is proportional to the square root of the laser power. So an increase in laser power leads to an increase in the mean photon count and a corresponding improvement in SNR. Therefore, a home-made detector with a much higher damage threshold than commercially available is constructed to reach a higher SNR based on Reference [70], the schematic of which is shown in Figure 7.1. It is inspired by a circuit design used by LIGO [71–73]. Besides the low-frequency noise in the system caused by vibrations, harmonics of 60 Hz AC power lines, laser pointing noise and acoustic noise around 237 Hz, etc, create a large imbalance in the photocurrent which leads to saturation of the photodetector. Thus, a high-pass filter with a 3-dB drop around 1 kHz is placed at the first amplification stage to overcome this problem.

One of the primary obstacles limiting the maximum power output of a photodetector is the vulnerability of the photodiodes to thermal damage. To overcome this challenge, using photodiodes with larger surface areas can help raise the thermal damage threshold and thus improve the maximum operating power of the photodetector. We use large area, low capacitance InGaAs

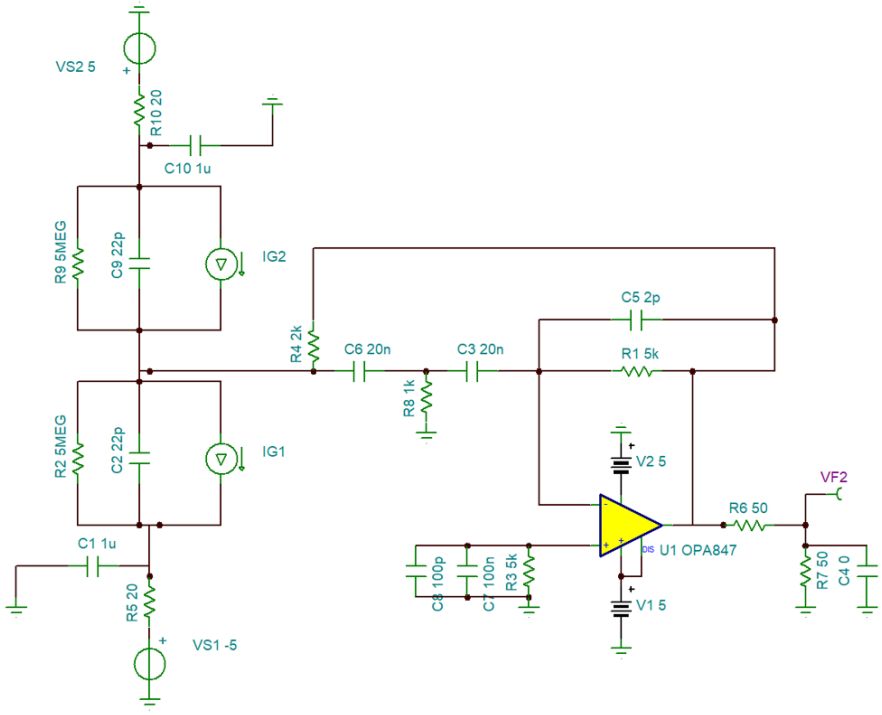

Figure 7.1: Schematic of the circuit of the high power balanced photodetector.

PIN photodiodes (Excelitas C30641GH) that are reversed biased at 5V. Their relatively low capacitance of 22 pF allows the detector to maintain a high bandwidth. Prior to assembling the photodetector circuit shown in Figure 7.1, we characterized its AC behavior in TINA, a circuit simulation software, to ensure reasonable cut-off frequencies. The result of the simulation is shown in Figure 7.2.

Although the photodiodes on the detector have a relatively large surface area with a 1.0 mm useful diameter, they are still quite small when compared to the size of the laser beam used in the experiment. This size discrepancy necessitates the use of focusing lenses to direct the laser beams onto

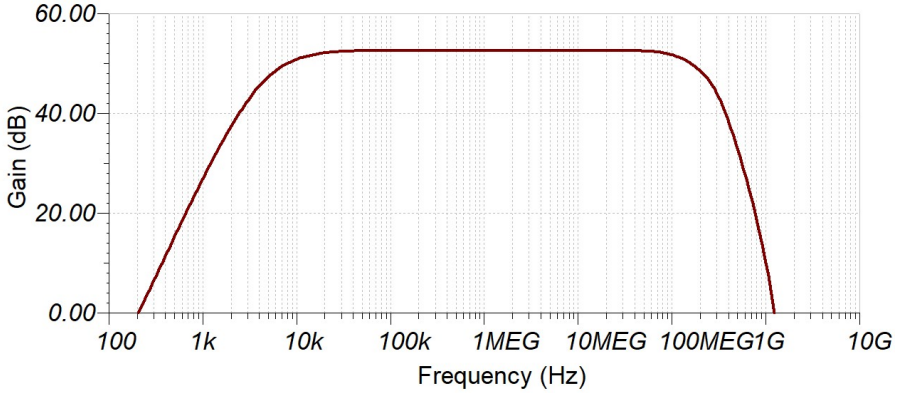

Figure 7.2: The simulated frequency response of the high power balanced photodetector in TINA

the photodiodes. We use a 16 mm Thorlabs cage rod system in conjunction with two XY translation mounts (Thorlabs SCP05) to allow for easy adjustments to be made to the distance between the lenses and photodiodes, as well as their relative transverse positions. This enables fine-tuning of focusing the laser beam onto the photodiodes to achieve optimal performance. Shown in Figure 7.3 is the cage rod system and the assembled circuit board contained within the housing.

It is worth noting that the results presented in Figure 7.2 are based on simulations and may not accurately reflect the actual frequency response of the detector once it has been constructed due to things such as parasitic capacitances that are inevitable on circuit boards. To properly evaluate the impact of the high-pass filter, the cut-off frequency should be determined through experimental measurement. We achieved this by directing a 1064 nm laser beam from our Mephisto laser, modulated by an AOM, to one of the ports of the

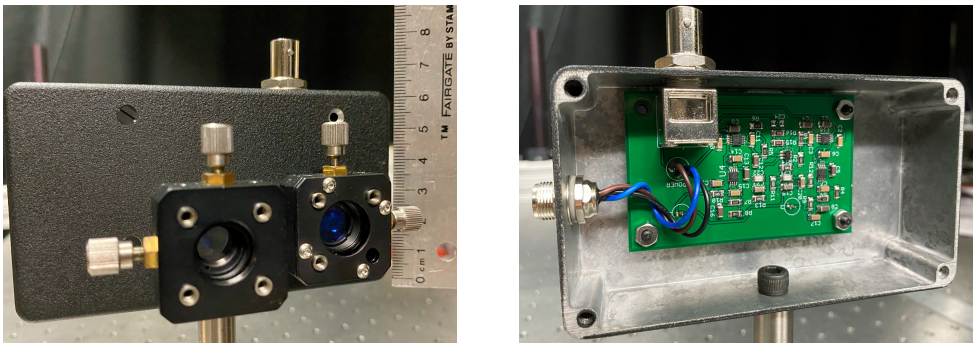

Figure 7.3: Photos of the high-power balanced photodetector. Left is the front of the detector with the adjustable lenses. Right is the circuit.

high-power balanced photodetector and measured the amplitude of the signal as the modulation frequency was varied. The cut-off frequency (-3 dB) was found to be around 975 Hz. To further characterize the bandwidth of the detector, especially the frequency response for high-frequency signals, a 1064 nm pulsed laser (Continuum Minilite) with a pulse duration of 5-7 ns was filtered and directed to one of the ports in the balanced detector. An averaged rise time τ_r between points 10% and 90% up the rising edge of the output signal is measured to be around 9 ns, which corresponds to a -3 dB cut-off frequency around 38 MHz, according to $f_{3\text{dB}} = 0.35/\tau_r$.

7.2 Brownian motion of graphene diaphragms in ambient air

Suspended graphene over a through hole is an excellent candidate for use as a diaphragm in an acoustic detector with an optical readout. Acoustic waves can be detected as they pass through one side of the device, while

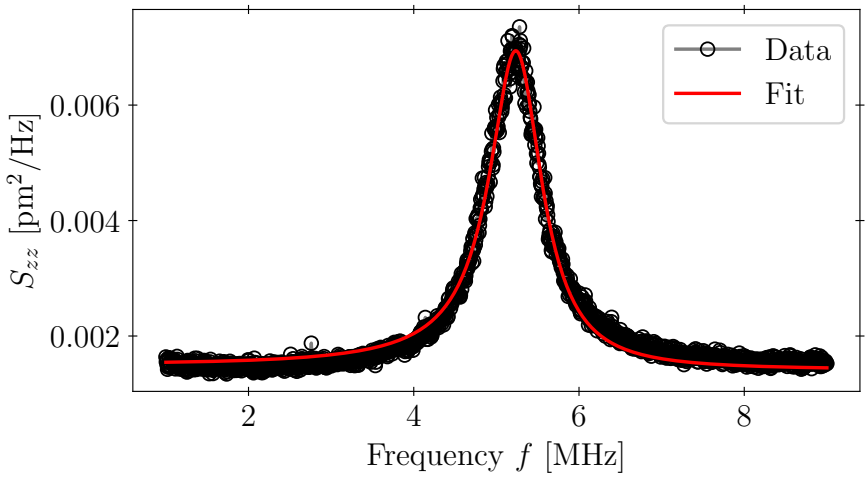

Figure 7.4: The position PSD for the first resonant mode of the 6-8 layer graphene diaphragm measured in ambient air.

a detection laser beam can access the graphene diaphragm from the other exposed side. As the graphene will be immersed in ambient air during the detection process, it is essential to conduct experiments to study its properties in this environment. In this section we report the results of the experiment conducted with the diaphragm in ambient air.

The experimental setup is very similar to that described in Chapter 6. The only difference is that the sample is now exposed to the ambient air. The position PSD of the first resonant mode is shown in Figure 7.4 and the position PSD of the first two resonant modes including the fitted resonant frequencies is shown in Figure 7.5. Based on the technique described in Chapter 6, the effective mass of the first resonant mode is found to be 558.0 fg with a relative uncertainty of 1.12 %. The first and second resonant frequencies are measured to be 5.26 MHz and 10.65 MHz, respectively, so the total mass is calculated to

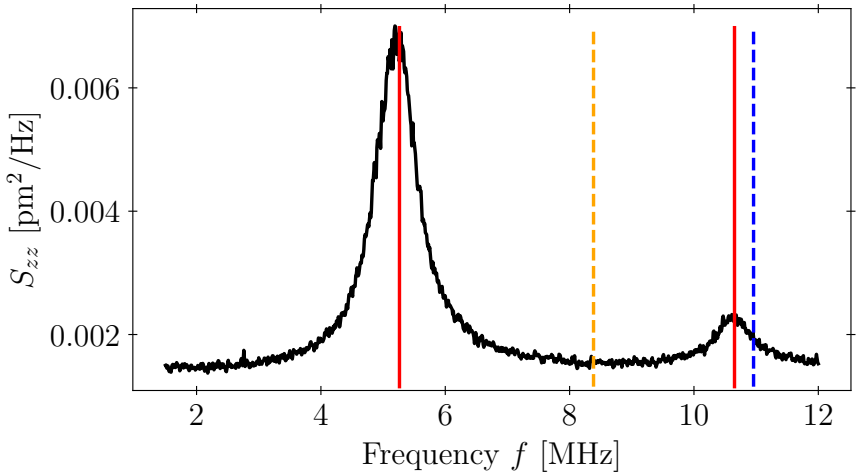

Figure 7.5: The position PSD for a 6-8 layer suspended graphene diaphragm in ambient air. The first two resonant peaks are shown. The color code is the same as Figure 6.10.

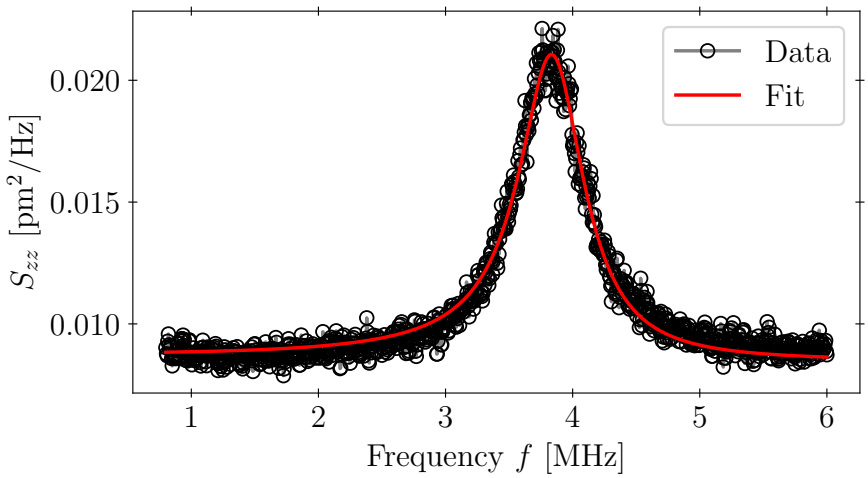

Figure 7.6: The position PSD for the first resonant mode of the bilayer graphene diaphragm measured in ambient air.

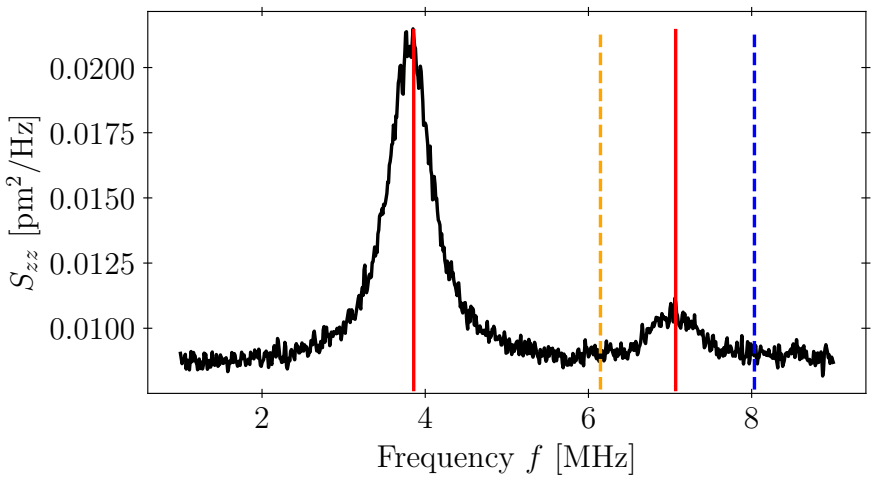

Figure 7.7: The position PSD for a bilayer suspended graphene diaphragm in ambient air. The first two resonant peaks are shown. The color code is the same as Figure 6.10.

be 3019.5 fg. A similar experiment was also performed with a bilayer graphene sample (Ted Pella 21920-5) with an identical radius. The results are displayed in Figures 7.6 and 7.7. The effective mass of the first resonant mode is found to be 566.7 fg with a relative uncertainty of 1.92 %. The first and second resonant frequencies are measured to be 3.86 MHz and 7.07 MHz, respectively. As a result, the total mass is calculated to be 2891.3 fg. It is worth noting that the mass of pure suspended graphene is 52.7 fg for bilayer graphene and 158.0-210.6 fg for 6-8 layer graphene. The large mass discrepancy between pure graphene and the total mass of the sample shows that contamination dominants the mass of the graphene sample in an ambient environment. Furthermore, when compared to the mass of the graphene diaphragm (1453.1 fg) that was put into a low-pressure chamber after being heated up, we can see that the cleaning

process can remove the half of the total contamination.

7.3 Summary and Future

7.3.1 Summary of work

The work presented in this dissertation includes two experiments that measure the mass of optically trapped microspheres and suspended diaphragms, respectively at thermal equilibrium using their Brownian motion.

Two methods have been explored to measure the mass of the optically trapped microspheres: the spectral method and the equipartition method. In the spectral method, the trap strength, density of the microsphere and the calibration factor can be accurately extracted. It serves as a calibration step and at the same time yields a mass measurement with 3.0% relative uncertainty with 3 seconds of data. After completing the calibration step, the equipartition method can be used to take rapid measurements of the mass and achieve a relative uncertainty of 4.1% with 0.3 seconds of data.

Based on the technique of laser Doppler vibrometry (LDV), the out-of-plane displacement of the suspended graphene diaphragm due to Brownian motion can be directly measured. The spectral method can be used to extract the effective mass of the fundamental resonant mode of the diaphragm. In order to extract the total mass of the suspended diaphragm, knowledge of the mode shape is required. A new method was developed to use the first two resonant frequencies to numerically solve for the resonant mode shape. This method has the benefit that it does not require knowledge of the phys-

ical and mechanical properties of the diaphragm except for the dimensions of the suspended diaphragm in the plane which can be measured very accurately. Furthermore, the method is robust and less affected by contaminants on the diaphragm thus allowing suspended diaphragms to be used in ambient environments.

7.3.2 Future directions

Ultimately, our goal is to develop a quantum-limited acoustic detector with potential applications for proton therapy [11–13] and dark matter detection [14–16]. By integrating the higher power balanced photodetector in a future setup of the optically trapped microsphere experiment, the shot-noise limited bandwidth in the high frequency range can be extended. This will make the optically trapped microsphere system a more powerful tool to detect high-energy, high-frequency acoustic signals.

One future application for the suspended graphene diaphragm we envision is to create a *portable* version of our experiment setup. Figure 7.8 shows the design of a heterodyne fiber interferometer with a suspended graphene diaphragm. The incoming laser beam is split into two branches with a 2x2 fiber coupler. The coupling ratio is chosen to be 90:10 so that the majority of the laser power is directed to the graphene diaphragm and the reflected powers from the two branches are comparable to each other. The frequency of the laser beam in the other branch is shifted by a fiber AOM and reflected back by a fiber retroreflector. Finally, the reflected beams from the graphene di-

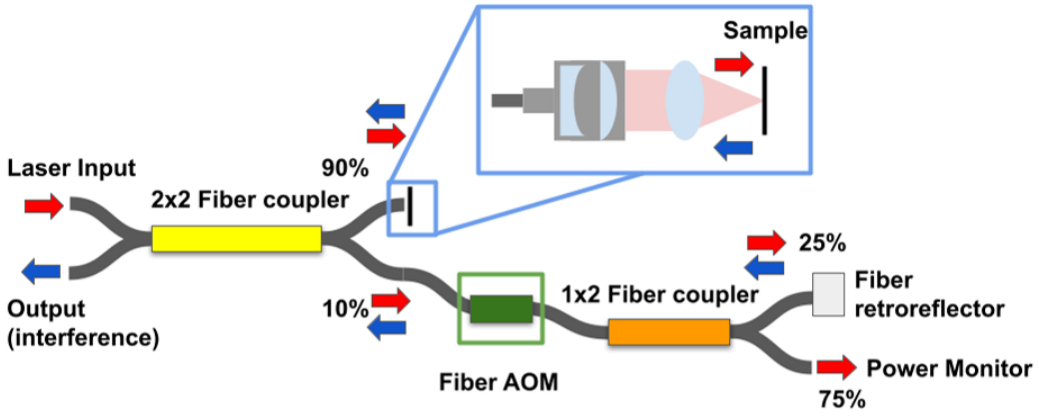

Figure 7.8: The design of a heterodyne fiber interferometer with suspended graphene. The red arrows represent the incoming laser beam and the blue arrows represent the reflected beam.

aphragm and the fiber retroreflector are combined to form a beat note signal encoding the displacement of the graphene diaphragm. The main benefit of using a heterodyne, rather than homodyne, design for a fiber interferometer is that the distance between the two arms doesn't need to be carefully chosen or locked in order to achieve the maximum sensitivity. Moreover, it can circumvent the saturation of the detection signal from low frequency noise by applying a high-pass filter prior to extracting the phase information from the beat note signal. This makes it suitable for detecting the high-frequency acoustic signals expected in detecting the Bragg peak in proton therapy and the acoustic waves in bubble chambers used for dark matter searches.

Bibliography

[1] R. Brown, "A brief account of microscopical observations made in the months of june, july and august 1827, on the particles contained in the pollen of plants; and on the general existence of active molecules in organic and inorganic bodies," *The Philosophical Magazine*, vol. 4, pp. 161–173, 1828.

[2] A. Einstein, "On the motion of small particles suspended in liquids at rest required by the molecular-kinetic theory of heat," *Annalen der physik*, vol. 17, pp. 549–560, 1905.

[3] M. von Smoluchowski, "Zur kinetischen theorie der brownschen molekularbewegung und der suspensionen," *Annalen der Physik*, vol. 326, pp. 756–780, 1906.

[4] P. Langevin, "On the theory of brownian motion," *C. R. Acad. Sci. (Paris)*, vol. 146, pp. 530–533, 1908.

[5] J. Perrin, "Brownian movement and molecular reality," *Taylor and Francis*, 1910.

[6] E. Nelson, "Derivation of the schrödinger equation from newtonian mechanics," *Phys. Rev.*, vol. 150, pp. 1079–1085, 1966.

[7] A. Einstein, "Theoretische bemerkungen Über die brownsche bewegung," *Zeitschrift für Elektrochemie und angewandte physikalische Chemie*, vol. 13, pp. 41–42, 1907.

[8] T. Li, S. Kheifets, D. Medellin, and M. G. Raizen, "Measurement of the instantaneous velocity of a brownian particle," *Science*, vol. 328, pp. 1673–1675, 2010.

[9] S. Kheifets, A. Simha, K. Melin, T. Li, and M. G. Raizen, "Observation of brownian motion in liquids at short times: Instantaneous velocity and memory loss," *Science*, vol. 343, no. 6178, pp. 1493–1496, 2014.

[10] L. E. Hillberry, *Optically trapped microspheres as sensors of mass and sound: Brownian motion as both signal and noise.* PhD thesis, The University of Texas at Austin, 2022.

[11] M. De Matteis, A. Baschirotto, and E. Vallicelli, "Acoustic analog signal processing for 20–200 mev proton sound detectors," *IEEE Transactions on Radiation and Plasma Medical Sciences*, vol. 6, pp. 325–335, 2022.

[12] W. Assmann, S. Kellnberger, S. Reinhardt, S. Lehrack, A. Edlich, P. G. Thirolf, M. Moser, G. Dollinger, M. Omar, V. Ntziachristos, and K. Parodi, "Ionoacoustic characterization of the proton bragg peak with submillimeter accuracy," *Medical Physics*, vol. 42, no. 2, pp. 567–574, 2015.

[13] F. R. Deurvorst, G. Collado Lara, A. Matalliotakis, H. J. Vos, N. de Jong, V. Daeichin, and M. D. Verweij, "A spatial and temporal characterisation

of single proton acoustic waves in proton beam cancer therapy," *The Journal of the Acoustical Society of America*, vol. 151, pp. 1200–1210, 2022.

[14] E. Behnke, J. Behnke, S. J. Brice, D. Broemmelsiek, J. I. Collar, P. S. Cooper, M. Crisler, C. E. Dahl, D. Fustin, J. Hall, J. H. Hinnefeld, M. Hu, I. Levine, E. Ramberg, T. Shepherd, A. Sonnenschein, and M. Szydagis, "Improved limits on spin-dependent wimp-proton interactions from a two liter CF_3I bubble chamber," *Phys. Rev. Lett.*, vol. 106, p. 021303, 2011.

[15] T. Kozynets, S. Fallows, and C. B. Krauss, "Modeling emission of acoustic energy during bubble expansion in pico bubble chambers," *Phys. Rev. D*, vol. 100, p. 052001, 2019.

[16] I. Felis, J. A. Martínez-Mora, and M. Ardid, "Acoustic sensor design for dark matter bubble chamber detectors," *Sensors*, vol. 16, no. 6, 2016.

[17] J. S. Bunch, A. M. van der Zande, S. S. Verbridge, I. W. Frank, D. M. Tanenbaum, J. M. Parpia, H. G. Craighead, and P. L. McEuen, "Electromechanical resonators from graphene sheets," *Science*, vol. 315, pp. 490–493, 2007.

[18] B. D. Hauer, C. Doolin, K. S. D. Beach, and J. P. Davis, "A general procedure for thermomechanical calibration of nano/micro-mechanical resonators," *Annals of Physics*, vol. 339, pp. 181–207, 2013.

[19] D. Davidovikj, J. J. Slim, S. J. Cartamil-Bueno, H. S. J. van der Zant, P. G. Steeneken, and W. J. Venstra, "Visualizing the motion of graphene nanodrums," *Nano Letters*, vol. 16, pp. 2768–2773, 2016.

[20] A. Kozbial, F. Zhou, Z. Li, H. Liu, and L. Li, "Are graphitic surfaces hydrophobic?," *Accounts of Chemical Research*, vol. 49, pp. 2765–2773, 2016.

[21] Z. Li, Y. Wang, A. Kozbial, G. Shenoy, F. Zhou, R. McGinley, P. Ireland, B. Morganstein, A. Kunkel, S. P. Surwade, *et al.*, "Effect of airborne contaminants on the wettability of supported graphene and graphite," *Nature materials*, vol. 12, pp. 925–931, 2013.

[22] S. S. Rao, *Vibration of Continuous Systems*. Wiley, 2007.

[23] A. Castellanos-Gomez, R. van Leeuwen, M. Buscema, H. S. J. van der Zant, G. A. Steele, and W. J. Venstra, "Single-layer mos2 mechanical resonators," *Advanced Materials*, vol. 25, pp. 6719–6723, 2013.

[24] R. J. Dolleman, "Graphene based pressure sensors: Resonant pressure transduction using atomically thin materials," Master's thesis, Delft University of Technology, 2014.

[25] T. Wah, "Vibration of circular plates," *The Journal of the Acoustical Society of America*, vol. 34, pp. 275–281, 1962.

[26] D. S. Lemons and A. Gythiel, "Paul langevin's 1908 paper "on the theory of brownian motion"," *American Journal of Physics*, vol. 65, no. 11, pp. 1079–1081, 1997.

[27] G. E. Uhlenbeck and L. S. Ornstein, "On the theory of the brownian motion," *Phys. Rev.*, vol. 36, pp. 823–841, Sep 1930.

[28] R. Kubo, "The fluctuation-dissipation theorem," *Reports on Progress in Physics*, vol. 29, p. 255, 1966.

[29] R. Kubo, "Brownian motion and nonequilibrium statistical mechanics," *Science*, vol. 233, pp. 330–334, 1986.

[30] R. J. Henery, "The generalized langevin equation and the fluctuation- dissipation theorems," *Journal of Physics A: General Physics*, vol. 4, p. 685, 1971.

[31] V. Balakrishnan, *Elements of Nonequilibrium Statistical Mechanics*. Springer Cham, 2008.

[32] J. C. Maxwell, *A Treatise on Electricity and Magnetism*. Clarendon Press, Oxford, 1st ed., 1873.

[33] P. Lebedew, "Untersuchungen über die druckkräfte des lichtes," *Annalen der Physik*, vol. 311, pp. 433–458, 1901.

[34] E. F. Nichols and G. F. Hull, "A preliminary communication on the pressure of heat and light radiation," *Phys. Rev. (Series I)*, vol. 13, pp. 307–320, 1901.

[35] J. Hecht, "A short history of laser development," *Appl. Opt.*, vol. 49, pp. F99–F122, 2010.

[36] A. Ashkin, "Acceleration and trapping of particles by radiation pressure," *Phys. Rev. Lett.*, vol. 24, pp. 156–159, 1970.

[37] A. Ashkin, J. M. Dziedzic, J. E. Bjorkholm, and S. Chu, "Observation of a single-beam gradient force optical trap for dielectric particles," *Opt. Lett.*, vol. 11, pp. 288–290, 1986.

[38] A. Ashkin, "Forces of a single-beam gradient laser trap on a dielectric sphere in the ray optics regime," *Biophysical Journal*, vol. 61, pp. 569–582, 1992.

[39] Y. Harada and T. Asakura, "Radiation forces on a dielectric sphere in the rayleigh scattering regime," *Optics Communications*, vol. 124, pp. 529–541, 1996.

[40] T. A. Nieminen, V. L. Y. Loke, A. B. Stilgoe, G. Knöner, A. M. Brańczyk, N. R. Heckenberg, and H. Rubinsztein-Dunlop, "Optical tweezers computational toolbox," *Journal of Optics A: Pure and Applied Optics*, vol. 9, p. S196, 2007.

[41] W. H. Wright, G. J. Sonek, and M. W. Berns, "Parametric study of the forces on microspheres held by optical tweezers," *Appl. Opt.*, vol. 33, pp. 1735–1748, 1994.

[42] Ryota, T. Omori, A. Kobayashi, and Suzuki, "Observation of a single-beam gradient-force optical trap for dielectric particles in air," *Opt. Lett.*, vol. 22, pp. 816–818, 1997.

[43] Y. Roichman, B. Sun, A. Stolarski, and D. G. Grier, "Influence of nonconservative optical forces on the dynamics of optically trapped colloidal spheres: the fountain of probability.," *Phys. Rev. Lett.*, vol. 101, p. 128301, 2008.

[44] P. Wu, R. Huang, C. Tischer, A. Jonas, and E.-L. Florin, "Direct measurement of the nonconservative force field generated by optical tweezers," *Phys. Rev. Lett.*, vol. 103, p. 108101, 2009.

[45] W. Stöber, A. Fink, and E. Bohn, "Controlled growth of monodisperse silica spheres in the micron size range," *Journal of Colloid and Interface Science*, vol. 26, pp. 62–69, 1968.

[46] B. Derjaguin, V. Muller, and Y. Toporov, "Effect of contact deformations on the adhesion of particles," *Journal of Colloid and Interface Science*, vol. 53, pp. 314–316, 1975.

[47] L.-O. Heim, J. Blum, M. Preuss, and H.-J. Butt, "Adhesion and friction forces between spherical micrometer-sized particles," *Phys. Rev. Lett.*, vol. 83, pp. 3328–3331, 1999.

[48] T. Li, *Fundamental tests of physics with optically trapped microspheres*. PhD thesis, The University of Texas at Austin, 2011.

[49] L. Hillberry, Y. Xu, S. Miki-Silva, G. Alvarez, J. Orenstein, L. Ha, D. Ether, and M. Raizen, "Weighing an optically trapped microsphere in thermal equilibrium with air," *Phys. Rev. Appl.*, vol. 14, p. 044027, 2020.

[50] A. V. Oppenheim, R. W. Schafer, and J. R. Buck, *Discrete-Time Signal Processing*. Prentice Hall Upper Saddle River NJ, 2001.

[51] S. R. Cole, H. Chu, and S. Greenland, "Maximum likelihood, profile likelihood, and penalized likelihood: A primer," *American Journal of Epidemiology*, vol. 179, pp. 252–260, 2013.

[52] S. F. Nørrelykke and H. Flyvbjerg, "Power spectrum analysis with least-squares fitting: Amplitude bias and its elimination, with application to optical tweezers and atomic force microscope cantilevers," *Review of Scientific Instruments*, vol. 81, p. 075103, 2010.

[53] C. Dawson and J. Bateman, "Spectral analysis and parameter estimation in levitated optomechanics," *J. Opt. Soc. Am. B*, vol. 36, pp. 1565–1573, 2019.

[54] S. Chapman, T. G. Cowling, and D. Burnett, *The Mathematical Theory of Non-Uniform Gases: An Account of the Kinetic Theory of Viscosity, Thermal Conduction and Diffusion in Gases*. Cambridge University Press, Cambridge, United Kingdom, 1990.

[55] H. Brenner, "The stokes resistance of a slightly deformed sphere," *Chemical Engineering Science*, vol. 19, pp. 519–539, 1964.

[56] J. Tellinghuisen, "Statistical error propagation," *The Journal of Physical Chemistry A*, vol. 105, pp. 3917–3921, 2001.

[57] J. Millen, T. Deesuwan, P. Barker, and J. Anders, "Nanoscale temperature measurements using non-equilibrium brownian dynamics of a levitated nanosphere," *Nature nanotechnology*, vol. 9, no. 6, p. 425—429, 2014.

[58] E. Hebestreit, M. Frimmer, R. Reimann, C. Dellago, F. Ricci, and L. Novotny, "Calibration and energy measurement of optically levitated nanoparticle sensors," *Review of Scientific Instruments*, vol. 89, p. 033111, 2018.

[59] G. Schnoering, Y. Rosales-Cabara, H. Wendehenne, A. Canaguier-Durand, and C. Genet, "Thermally limited force microscopy on optically trapped single metallic nanoparticles," *Phys. Rev. Appl.*, vol. 11, p. 034023, 2019.

[60] D. Allan, "Statistics of atomic frequency standards," *Proceedings of the IEEE*, vol. 54, pp. 221–230, 1966.

[61] F. Czerwinski, A. C. Richardson, and L. B. Oddershede, "Quantifying noise in optical tweezers by allan variance," *Opt. Express*, vol. 17, pp. 13255–13269, 2009.

[62] J. W. S. Rayleigh, *The Theory of Sound*, vol. 1. New York: Dover, 1945.

[63] D. J. Wilson, *Cavity Optomechanics with High-Stress Silicon Nitride Films*. PhD thesis, California Institute of Technology, 2012.

[64] I. Elishakoff, *Probabilistic Methods in the Theory of Structures*. WSPC, 3rd ed., 2017.

[65] S. Afyouni Akbari, V. Ghafarinia, T. Larsen, M. M. Parmar, and L. G. Villanueva, "Large suspended monolayer and bilayer graphene membranes with diameter up to 750μm," *Scientific Reports*, vol. 10, p. 6426, 2020.

[66] W. Osten, *Optical Inspection of Microsystems*. CRC Press, 2nd ed., 2019.

[67] R. A. Barton, I. R. Storch, V. P. Adiga, R. Sakakibara, B. R. Cipriany, B. Ilic, S. P. Wang, P. Ong, P. L. McEuen, J. M. Parpia, and H. G. Craighead, "Photothermal self-oscillation and laser cooling of graphene optomechanical systems," *Nano Letters*, vol. 12, pp. 4681–4686, 2012.

[68] R. Singh, R. J. Nicholl, K. I. Bolotin, and S. Ghosh, "Motion transduction with thermo-mechanically squeezed graphene resonator modes," *Nano Letters*, vol. 18, pp. 6719–6724, 2018.

[69] R. De Alba, F. Massel, I. R. Storch, T. Abhilash, A. Hui, P. L. McEuen, H. G. Craighead, and J. M. Parpia, "Tunable phonon-cavity coupling in graphene membranes," *Nature nanotechnology*, vol. 11, pp. 741–746, 2016.

[70] S. Kheifets, *High-sensitivity tracking of optically trapped particles in gases and liquids: observation of Brownian motion in velocity space.* PhD thesis, The University of Texas at Austin, 2014.

[71] O. Jennrich, G. Newton, K. Skeldon, and J. Hough, "A high power photodetection system for use with laser interferometric gravitational wave detectors," *Optics Communications*, vol. 205, pp. 405–413, 2002.

[72] P. Kwee, B. Willke, and K. Danzmann, "Shot-noise-limited laser power stabilization with a high-power photodiode array," *Opt. Lett.*, vol. 34, no. 19, pp. 2912–2914, 2009.

[73] P. Kwee, B. Willke, and K. Danzmann, "Laser power noise detection at the quantum-noise limit of 32 a photocurrent," *Opt. Lett.*, vol. 36, pp. 3563–3565, 2011.

Vita

Yi Xu was born in Dexing Tongkuang, Jiangxi Province, China in 1994. She completed her high school education from Dexing Tongkuang High School in 2012. She received the Bachelor of Science degree in Physics from Huazhong University of Science and Technology in 2016. She enrolled in the physics graduate program at the University of Texas at Austin and immediately joined Professor Mark Raizen's research group.

Address: yixu@utexas.edu

This dissertation was typeset with LaTeX[†] by the author.

[†]LaTeX is a document preparation system developed by Leslie Lamport as a special version of Donald Knuth's TeX Program.